Doctoral Dissertation
Doctoral Program in Mechanical Enginering (37th cycle)

# Pneumatic Soft Robotic System for Actuation and Sensing

## Novel sustainable solutions for Service Robotics

**Giovanni Colucci**

* * * * *

**Supervisor**
Prof. Giuseppe Quaglia, Supervisor

**Doctoral examination committee**
Prof. Luca Bruzzone, Referee, Università degli Studi di Genova
Prof. Giulio Reina, Referee, Politecnico di Bari

Politecnico di Torino
May 2025

I hereby declare that, the contents and organisation of this dissertation constitute my own original work and does not compromise in any way the rights of third parties, including those relating to the security of personal data.

. . . . . . . . . . . . . . . . . . . . . . . . . . . . . . . . . . . . . .

Giovanni Colucci
Turin, May 2025

# Summary

Service Robotics is the branch dedicated to the development of robotic technologies aimed directly at serving humans. Today, service robots must be efficient and safe in order to interact in unstructured environments where humans or other living creatures are present.

This thesis presents two pneumatic technologies, namely an actuator and a sensor, for Service Robotics applications. To this aim, the research context is first provided, outlining the evolution of pneumatic robotic systems over the past two decades. The main application areas of Service Robotics will then be described, including their challenges, design requirements, and how the scientific community has responded to these needs with pneumatic-based solutions. Additionally, the rise of Soft Robotics will be discussed, with a particular focus on the materials and methodologies currently employed for the fabrication of soft pneumatic robots.

The thesis will then explore the development of a linear soft pneumatic actuator that exploits the principle of antagonistic chambers to achieve bidirectional behavior. Design methodologies, prototyping techniques, and static performance in terms of stroke, exerted force, and energy consumption will be described. Particular attention will be paid to the evaluation of control methods for energy savings. The experimental phase will include not only the characterization of the actuator but also its implementation in the development of a lightweight compliant soft gripper.

The final chapter will address the development of a sensing unit based on a soft pneumatic chamber connected to an auxiliary electro-pneumatic circuit. The approach will follow the same process as the actuator, from the theoretical formulation of the geometry and system outputs to its prototyping and experimental characterization. Particular attention will be devoted to the reliability quantification of the system. The anticipated applications of this concept include the development of a tactile sensing system to enhance the exteroceptive capabilities of robotic grippers, as well as the creation of a lightweight, untethered haptic device for active finger tele-rehabilitation, which has led to a patent application.

# Acknowledgements

The idea, concepts and results presented in this thesis are the result of research work shared with members of the Automation and Robotics group at Politecnico di Torino. Specifically, I would like to acknowledge Prof. Giuseppe Quaglia, who contributed and provided input for the creative and conceptual activity, as well as supervised the work in its entirety. I would also like to extend my thanks to Simone Duretto, my colleague, with whom we shared creative aspects and most of the prototype and experimental activities. Finally, I would like to express my gratitude to the entire research group of which I am a part, which provided important technical support at various stages of the research work.

A short but significant part of my PhD experience was carried out at the TU Delft Faculty of Mechanical Engineering. The research work conducted has not been reported in this thesis, but was also important for my formation. For this reason, I would like to thank Dr. Aimée Sakes for having hosted me in the BITE research group, and all colleagues who provided me with support in carrying out my research activities.

# Contents

# List of Tables

# List of Figures

# Chapter 1

# Introduction

Robotics was initially developed to replace human beings in industrial tasks and to meet the flexibility demands of modern production plants. Since then, the results achieved and the technological solutions developed in this multidisciplinary field have influenced the scientific community in creating technologies more directly focused on human needs.

This trend in robotics is known as Service Robotics, for it prioritizes societal needs and requires strong interaction between humans and robots [1]. By its very nature, Service Robotics provides multiple areas of study for researchers. A service robot must be capable of operating in an environment that is not predetermined (unstructured or semi-structured environment), while also understanding human behavior, cooperating with people, and, above all, ensuring that it does not harm or injure them.

It is clear that these fundamental requirements generate multiple research topics, which aim to address, either individually or collectively, the related challenges. Among these topics, there is certainly the development of compliant systems for grasping and manipulating fragile objects, whose geometry and properties are not known in advance, as well as the development of safe and lightweight systems for human collaboration. On both topics, this thesis seeks to provide a modest but cutting-edge contribution.

Although Service Robotics attracts researchers with diverse technical expertise, primarily focused on developing and prototyping new ideas in this field, great attention must be paid to the social and environmental implications that arise. If, in the past, the development of a new engineering solution was primarily driven by improving performance compared to what was already on the market, today there is a need to pay attention to the sustainability of the solution itself. A clear reference for evaluating whether a technology can be classified as sustainable has been provided by the United Nations with the Sustainable Development Goals [2]. These goals form a list of 17 objectives for the 2030 Agenda for Sustainable Development, adopted by all United Nations Member States in 2015, aiming to promote sustainable development for both humans and the environment.

The SDGs address highly complex and diverse issues. By their very nature, technological solutions often align closely with specific SDGs. The haptic device for telerehabilitation presented in subsection 3.4.2, for instance, is related to SDG 3.4, which focuses on the promotion of mental health and well-being. The soft bi-directional actuator in chapter 2 and the pneumatic tactile sensing unit in subsection 3.4.1, on the other hand, are closely aligned with SDG 9.5, which focuses on enhancing research and upgrading technologies. However, a key design goal when developing new service robots should be to address multiple SDGs in order to truly consider a solution as sustainable.

Another aspect to evaluate is whether the developed technology, beyond being sustainable, is also appropriate. The development of appropriate technologies, i.e. technologies that are sustainable but also human-centered and respond to a necessary human need, is a complex and still open issue. In fact, it is difficult to provide a clear and widely accepted definition of what can truly be considered appropriate for humans [3]. A highly technological solution with the potential to create new jobs may still prove unsustainable or may not be socially accepted. For example, the study by Nomura et al. [4] discusses how the same technology (humanoid robots) is perceived by students from different cultural backgrounds and how its usefulness and impact on human life can be perceived in completely different ways.

This thesis does not aim to provide an exhaustive answer to these issues. However, the development of pneumatic and soft systems, which is the central theme of the following sections and chapters, represents a concrete solution for human-robot interaction, that is, putting robotics at the service of human needs. Additional attention has also been given to the topic of energy efficiency. This has been addressed both through systems that are inherently low-energy-consuming and through the analysis of additional methods to reduce the system's energy demand.

With this premise, the rest of the chapter will describe the role of pneumatic systems within Service Robotics, starting from traditional pneumatic systems and then exploring the emergence of Soft Robotics and its implications. To this end, robots will be classified into three main categories: exoskeletons and wearables, manipulators, and mobile robots. The application sectors, on the other hand, will follow the professional applications (including medical applications) identified by the International Federation of Robotics (IFR) [5].

The concluding section will thus outline the structure of the following chapters of this thesis.

## 1.1 Pneumatics for Service Robotics

Pneumatic systems have traditionally been one of the possible solutions for controlling automatic systems. They consist of actuators, sensors, switches, logic elements, interface components, directional valves, proportional valves, storage systems, and air treatment units. At an industrial level, these elements are managed through programmable logic controllers (PLCs) and work together to regulate production processes.

In the field of Service Robotics, i.e., robotics designed for direct human interaction, there has essentially been a transposition of pneumatic technologies previously developed for the industrial sector. Figure 1.1 illustrates the application of traditional pneumatic systems across various sectors identified by the IFR. Robots are classified into three main categories: exoskeletons and wearables, manipulators, and mobile robots.

The study by Morales et al. [6] discusses the use of pneumatic technology for the

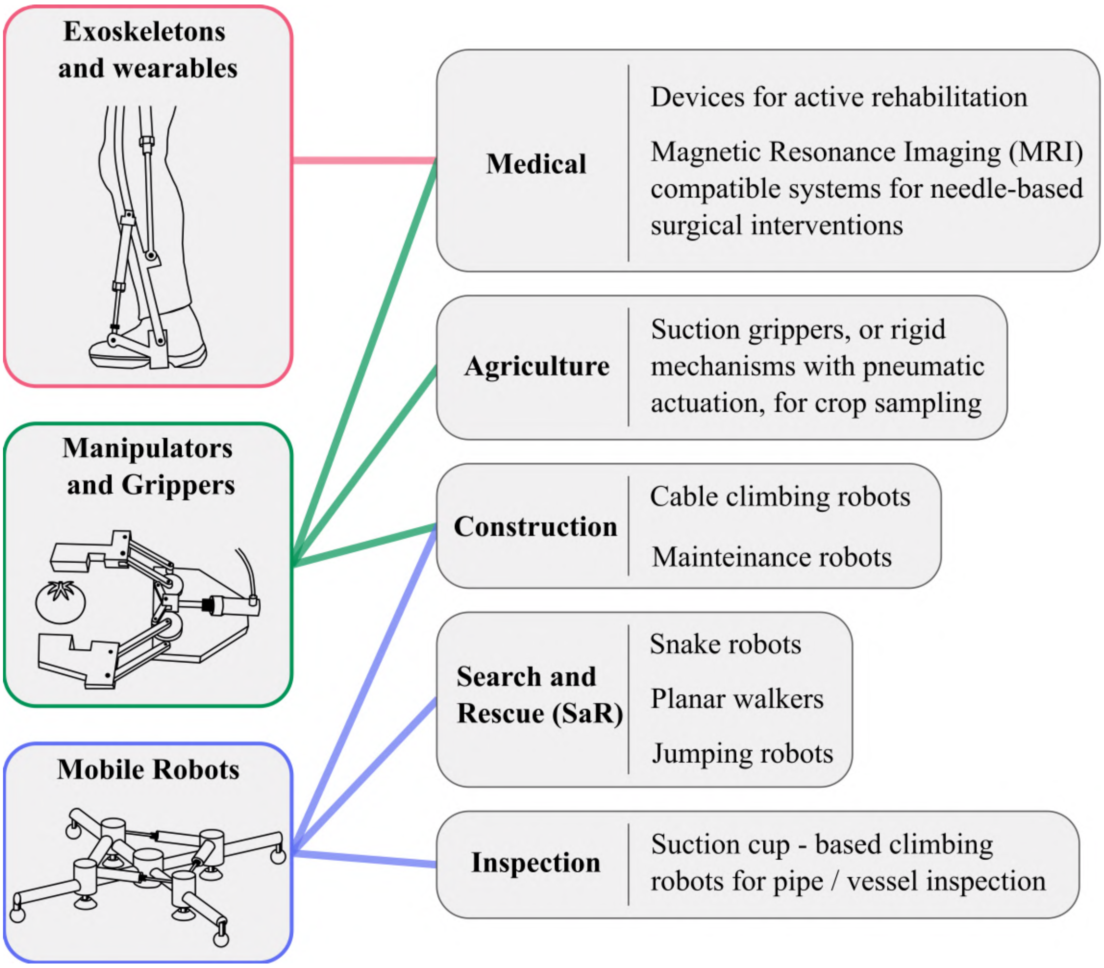

Figure 1.1: Traditional pneumatic systems in the application macro-areas of Service Robotics according to IFR (professional application and medical) [5].

development of robotic rehabilitation systems. The reason behind the development of rehabilitation robots directly originates from well-established findings in medical science, which clearly demonstrate how physical exercises based on voluntary movements can produce significant clinical results in motor recovery. Physical exercise based on voluntary movements enables both functional recovery following damage to the central nervous system [7] and neurogenesis, i.e., the formation of new neural connections [8]. A robotic system can thus help structure a rehabilitation procedure that is repetitive, monitored, and reduces the workload on therapists [9, 10, 11].

The primary need was to create systems that were safe for humans. Pneumatic systems are defined as intrinsically compliant since the compressibility of air ensures the absorption of unwanted forces, and they are also characterized by a high force-to-weight ratio. An additional advantage is their high reliability, as they are based on physical principles previously tested and developed for industrial applications. The main disadvantages, however, were the control and energy consumption of the systems [6].

The review by Su et al. [12] and that of Elhawary et al. [13] highlight a second type of application in the medical field, which concerns the development of medical robots compatible with magnetic resonance imaging (MRI). There are indeed some procedures, such as needle insertion, biopsy interventions, and catheter placement, that require imaging modalities to provide multi-parameter imaging to the medical staff. The use of robotic systems in this field reduces the time required for the procedure and improves needle placement accuracy. However, it is clear that the use of electric motors is not possible, as they would compromise the MRI outcomes and vice versa. Pneumatic actuation, then, becomes one of the feasible technological solutions. In this case, the use of dielectric materials for the pneumatic components ensures the complete absence of electromagnetic interference, but the compressibility of air represents a disadvantage, as it introduces time delays and back-drivability [14].

In the case of inspection activities, the use of pneumatic service robots is generally exploited because they are safe and allow navigation in particularly hostile environments. The Nuclear Electric Robot Operator (NERO) [15], for example, is a climbing robot for the inspection of nuclear reactor pressure vessels. Pneumatic technology is used to create the motor structure, with vacuum grippers as feet and pneumatic cylinders as legs. The robot is intrinsically safe since, in the event of an electrical failure in the control system, the valve system automatically brings the robot to a safe condition. Given the low cost, simple control, and high adhesion forces, suction cups have, in fact, been among the most used solutions for the creation of inspection climbing robots [16, 17]. The pipe inspection robot by Yoon and Park [18] is another example where pneumatic technology is chosen for navigation in high-temperature and high-pressure environments.

Regarding mobile robotics for search and rescue, pneumatics has been used for the development of snake robots, articulated robots, or for the actuation of active joints. For example, an architecture similar to that of Yoon and Park [18] was used by Chen and Yeo [19] to build a search and rescue robot that exploits the inchworm motion concept. The planar walker combines a series of pneumatic actuators and suction grippers to create a reconfigurable quadrilateral structure that allows for the generation of a two-dimensional gait. The suction grippers represent the potential anchor points to the ground, and the pneumatic cylinders form the links of the quadrilateral, and their actuation causes the reconfiguration of the structure. In the same application theme of search and rescue robotics, pneumatic actuators have been used for the actuation of active joints between modules of the OmniTread snake robot [20]. The work of Ohno and Hirose [21] shows, instead, a remarkable example of a system where the basic unit, called the SR unit, is an active pneumatic unit with three degrees of freedom and integrated control (valves, sensors, controller). The SR unit is provided with three pneumatic actuators arranged in parallel configuration, and it has a cylindrical encumbrance with a diameter of 120 mm, and a longitudinal stroke of 63 mm (from 114 to 177 mm). A series of SR units are eventually implemented to create a snake robot with a winding gait. A final application context of pneumatics in Service Robotics involves providing the mechanical power needed to perform a jump. Tsukagoshi et al. [22] developed a search and rescue robot weighing 2.3 kg, equipped with differential steering wheels, and an additional jumping mechanism realized using a pneumatic actuator. The switching of a 3-way 2-position spool valve connects to a pressurized air reservoir (0.7 MPa), which enables the robot to jump to heights of 80 cm, or 3.5 times the height of the robot.

Although the construction robotics sector is niche, examples of pneumatic solutions in this field include the development of cable-climbing robots for cable-stayed bridge maintenance [23, 24] and robotic manipulators for window glass mounting [25].

Agricultural robotics represents another sector in which pneumatic technology exploits its inherent compliance for crop sampling or harvesting. The main design requirement, therefore, consists of handling delicate objects with complex and variable shapes, whose rough or highly curved surfaces require an adaptable and compliant system. The work of Foglia and Reina [26], for example, presents a double four-bar manipulator and a two-finger rigid gripper, whose actuation is achieved solely through pneumatic actuators (cylinders for the manipulator, pneumatic muscle for the gripper). In this case, the requirement for adaptability to different shapes is not met, as the solution is specifically developed for harvesting a particular variety of radicchio. There are also similar works on grippers or rigid manipulators actuated by pneumatic actuators [27, 28, 29]. The geometric variability, as well as the fragility of objects such as strawberries, eggplants, peppers, etc., has also led to the development of suction grippers, such as the gripper for eggplant firmness evaluation by Blanes et al. [30], the cherry peduncle detacher by Tanigaki et al. [31], or the sucker-cutter gripper for sweet pepper harvesting by Lehnert et al. [32].

## 1.2 The advent of Soft Robotics

In articles concerning Soft Systems for Service Robotics, the most commonly cited example is that of the Mc-Kibben muscle, a unidirectional pneumatic actuator whose invention is attributed to Richard H. Gaylord (1958), but was later taken up a few years later by the American atomic physicist Joseph L. McKibben in order to create an exoskeleton to assist the weak musculature of the upper limb of people affected by poliomyelitis [33, 34]. The Mc-Kibben muscle represents the precursor, and still remains one of the remarkable examples of Soft Robotics. Over the past two decades, it has been the subject of various studies aimed at its modeling [35, 36, 37], its realization using innovative techniques [38, 39, 40], and its use in Service Robotic Systems [41, 42, 43, 44]; but in essence, it is a pneumatic actuator made using soft materials, namely an inner tube (bladder) and an outer sleeve to constrain and impose the muscle deformation. Unlike a traditional single-acting pneumatic cylinder, the Mc-Kibben muscle generally behaves like a linear actuator, but a force perpendicular to its axis can cause it to bend. For this reason, and due to its rubber (or similar) walls, the Mc-Kibben muscle is considered a soft actuator and can therefore interact with humans and natural environments with greater safety.

As mentioned, the Mc-Kibben muscle represents only the first example of a series of scientific activities that, since the early 2000s, have given rise to the new technological field of Soft Robotics. A 2024 study conducted by Aracri et al. [45] highlights how, in the early years of the millennium, Soft Robotics experienced steady but modest growth, with 500 articles published in 2015. From 2016 onwards, however, the development was of an entirely different nature, with 2500 articles published in 2021 alone. The fundamental principle behind all the work is essentially the same: the development of robotic systems based on deformable materials, mainly made of soft and compliant materials [46].

The scientific literature includes several reviews that analyze the world of Soft Robotics. The 2013 review by Kim et al. [47] presents various types of bio-inspired soft robots. The most recent work by Alici and Tawk [46] analyzes soft actuators and sensors made using additive manufacturing, while the 2018 work by Shintake et al. [48] focuses on soft robotic grippers. Finally, the 2017 work by Polygerinos et al. [49] specifically addresses pneumatic soft robotic technologies. The following sub-sections build on these concepts, integrate them with more recent studies, and provide a categorization based on construction methodologies and application fields, with a final comparison with the solutions from the previous section.

### 1.2.1 The role of materials and manufacturing methods

Soft Robotics is, evidently, an extraordinarily vast and multidisciplinary field, where the design limits are imposed by the materials used as well as the related manufacturing techniques. Figure 1.2 summarizes, in tabular form, the main production processes and the related materials employed in the creation of a soft pneumatic robot.

The first technique that is worth mentioning is the moulding of highly elastic materials. While, in the past, the production of moulds was a critical aspect of this technique, this is nowadays largely solved by creating the moulds in rigid plastic material using additive manufacturing machines (typically Fused Deposition Modeling, FDM). Moulding is, in fact, one of the most accessible and cost-effective methods for producing pneumatic soft robots. Ilievski et al. [50], for example, realized a pneumatic bi-directional and multi-material soft bending gripper by using polydimethylsiloxane (PDMS) for the central layer, which bends but does not undergo large deformations, and a siloxane, with a higher maximum strain rate, for the chambers of the various pneumatic actuators that make up the gripper. Similarly, Morin et al. [51] used the same basic unit, i.e., a PneuNet actuator, to create a fluidic planar walker with additional camouflage capabilities.

Han et al. [52] instead created a pneumatic soft bending actuator through a circular soft chamber made of silicone rubber and a constraining frame made of polyurethane. The actuator was then used to create the gripper, and the physical principle of granular jamming was employed to stiffen the actuators once they are in contact with the object to be grasped. López-Díaz et al. [53] developed a similar solution, but made from hydrogel, which also shows self-healing capabilities.

Another remarkable example is the work of Bell et al. [54], in which a double-acting PneuNet actuator is integrated with a peristaltic pump to obtain a compact and untethered actuation unit. In this case as well, the actuator is fabricated through injection molding of a silicone elastomer, but the constraining material consists of a thin metal mesh.

Jones et al. [55] created a class of soft pneumatic actuators using bubble casting. This method is based on the complete filling of a mold through the injection of Vinyl Polysiloxane (VPS). The internal channel is then formed by injecting air, which, due to gravity, tends to float in the VPS, creating an internal channel whose axis of symmetry does not coincide with that of the VPS structure. Once cured, the final result consists of an element with anisotropic behavior when pressurized.

Finally, there are examples where the internal chambers of a molded soft pneumatic actuator are filled with a porous rubber, which is obtained using a silicone elastomer as a matrix and salt as a fugitive porogen [56, 57]. The presence of foam in the internal chambers of the structure helps reinforce the actuator and prevents uncontrolled volumetric deformation when pressurized.

Further examples of pneumatic soft actuators fabricated through molding are provided in the 2022 review paper by Xavier et al. [58].

Additive manufacturing represents the other predominant methodology for fabricating soft robots. The review by Sachyani Keneth et al. [59], published in 2021, offers a broad overview, which is expanded here with more recent examples.

The Fused Deposition Modeling (FDM) method is undoubtedly the most widely used technique due to its low cost. It allows the printing of polyurethane (PU) material with

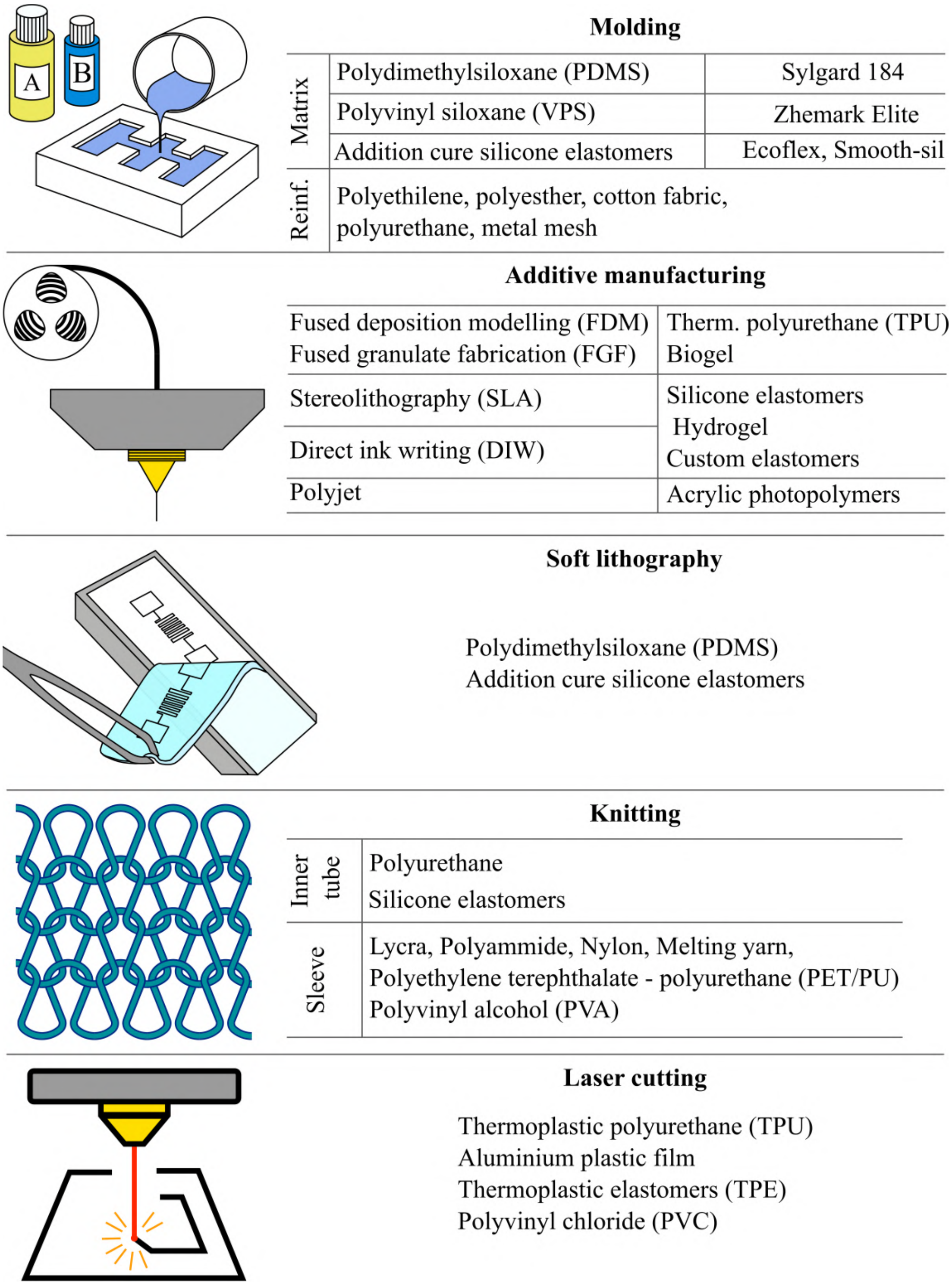

**Molding**

| | | |
|---|---|---|
| Matrix | Polydimethylsiloxane (PDMS) | Sylgard 184 |
| | Polyvinyl siloxane (VPS) | Zhemark Elite |
| | Addition cure silicone elastomers | Ecoflex, Smooth-sil |
| Reinf. | Polyethilene, polyesther, cotton fabric, polyurethane, metal mesh | |

**Additive manufacturing**

| | |
|---|---|
| Fused deposition modelling (FDM)<br>Fused granulate fabrication (FGF) | Therm. polyurethane (TPU)<br>Biogel |
| Stereolithography (SLA) | Silicone elastomers<br>Hydrogel<br>Custom elastomers |
| Direct ink writing (DIW) | |
| Polyjet | Acrylic photopolymers |

**Soft lithography**

Polydimethylsiloxane (PDMS)
Addition cure silicone elastomers

**Knitting**

| | |
|---|---|
| Inner tube | Polyurethane<br>Silicone elastomers |
| Sleeve | Lycra, Polyammide, Nylon, Melting yarn,<br>Polyethylene terephthalate - polyurethane (PET/PU)<br>Polyvinyl alcohol (PVA) |

**Laser cutting**

Thermoplastic polyurethane (TPU)
Aluminium plastic film
Thermoplastic elastomers (TPE)
Polyvinyl chloride (PVC)

Figure 1.2: Materials and methods used in the manufacture of soft pneumatic robots.

different hardness levels (typically 60-95A), though with lower accuracy compared to other methods. Nevertheless, there are several noteworthy examples, including the PneuNet actuator with internal lattice structures by Lalengani Dezaki et al. [60] or the pneumatic auxetic structure by Eguchi et al. [61], manufactured using Fused Granulate Fabrication (FGF), which extrudes granules of material instead of a filament.

Although FDM is typically cited for the fabrication of soft robots in PU, Heiden et al. [62] proposed, in 2022, the fabrication of actuators using a fully biodegradable gelatin-based hydrogel (biogel).

On the other hand, stereolithography (SLA), which consists of the selective polymerization of a liquid resin using a laser beam, generally achieves more accurate results than FDM, both in terms of nominal layer resolution and the actual printed object. It can be used for the fabrication of objects in hydrogel [63], silicone [64], photopolymers [65], or custom elastomers [66, 67, 68].

SLA shares with Direct Ink Writing (DIW) a high adaptability for printing materials of different nature, but it also offers the additional capability of multimaterial printing. Schaffner et al. [69] developed custom silicone-based printable inks with different elastic properties and used them to fabricate soft multimaterial actuators. Cheng et al. [70] instead created a biomimetic pneumatic tentacle using hydrogel ink. Finally, Wang et al. [71] used silicone-based inks for multimaterial printing in a support matrix, which eliminates the problem of overhang angles and thus allows for the creation of even more complex geometries.

The polyjet technique represents another option for multimaterial printing.
Sheng et al. [72] developed a soft crawling robot inspired by caterpillars. The soft material used is an acrylic photopolymer with a maximum strain of 140%. To enable forward motion, the robot's contact elements with the ground consist of anisotropic feet, combining rigid and soft materials. Kappel et al. [73] used similar methodologies to build a bending actuator and then compared it with the same actuator manufactured via FDM. The result showed that the polyjet-made specimen exhibited lower elasticity and reduced fatigue resistance compared to the FDM version, a finding also confirmed in [71].

Additionally, polyjet printing imposes constraints on the viscosity, surface tension, and evaporation rate of the material, limiting its application to the few commercially available materials [59].

In the case of millimeter-scale soft systems, additive manufacturing techniques are unsuitable, and soft lithography is employed instead. The outcome of such processes typically consists of pneumatic small-scale soft structures made of silicone elastomers, generally PDMS.

In a recent 2023 study, Milana et al. [74] developed an array of soft and flexible microactuators acting as artificial cilia, which could be used for micropumping or micromixing tasks. The authors designed a micromold that enables the molding of 36 microactuators in a single casting, each with an outer diameter of 150 $\mu$m and a length of 450 $\mu$m. Another remarkable work was presented by Russo et al. [75], where the soft lithography process was used to fabricate soft fluidic microactuators in biocompatible silicone elastomers with proprioceptive sensing capabilities. This work was later expanded upon by the same authors for the fabrication of a 12-layer soft spider in PDMS [76], featuring multiple degrees of actuation.

Another approach involves the use of knitting techniques, adapted from the garment industry, for the fabrication of outer constraining sleeves for soft airtight chambers. The achievable geometries are evidently more limited compared to additive manufacturing techniques (restricted to rectangular or cylindrical shapes), but sewing proves to be a simple and reliable process, which is why several noteworthy studies can be found in the literature.

In the work of Elmoughni et al. [77], the airtight bladder is made of laser cut PU sheets, welded together with an impulse sealer, while the outer shell is manufactured using a garment knitting machine with materials such as Lycra or polyamide. Yang et al. [78] developed a monodirectional bending/unfolding actuator that combines, for the outer sleeve, a conductive layer for deformation self-sensing and an elastic layer that acts as a recovery spring. A similar approach, but with a different knit geometry, is used by Luo et al. [79], employing a Lycra yarn. A recent study by Wang et al. [80] from 2024 discusses the effect of different knitting techniques on the behavior and performance of bending soft pneumatic actuators. Finally, Sanchez et al. [81] utilized acrylic, elastomer, and polyvinyl alcohol (PVA) to create a family of seamless and monolithic sleeves for soft manipulators and mobile robots.

In the case of flat or origami-inspired structures, it is possible to construct soft pneumatic robots using laser cutting. In this approach, flat soft bladders are cut by a laser beam and then sealed together. For example, Amiri Moghadam et al. [82] used thermoplastic polyurethane to fabricate a thin soft gripper and a four-arm swimming robot. In this case, the TPU layers were stacked, and the laser beam performed both the membrane cutting and the sealing of the internal chambers. Shen et al. [83] developed a flat pneumatic artificial muscle (FPAM) with a similar laser cutting/welding technique, employing an al-plastic film (ALF) that withstood a maximum pressure of 200 kPa (gauge). The pneumatic bladder was constrained by an outer mesh made of polyethylene terephthalate (PET), also laser-cut, and kevlar wires.

Rogatinsky et al. [84] proposed a soft robot for constrained environments made of stacked balloon actuators (SBAs). The single balloon was fabricated by stacking two layers of thermoplastic elastomer (TPE), which were selectively sealed through selective heat pressing, while a Teflon intermediate mask was used to preserve the internal chamber. Chen et al. [85] developed an origami-inspired bending actuator using laser cutting, with TPU as the sealing layer and polyvinyl chloride (PVC) as the structural layer. The two layers were joined together using double-sided adhesive tape and subsequently heat-pressed along the edges. A similar approach was presented by Li et al. [86] for the fabrication of stacked balloon actuators.

### 1.2.2 Soft Robotics applications

While traditional pneumatics found its application by adapting developments from the industrial sector to the context of Service Robotics, Soft Robotics operates at a generally deeper level, starting from the redesign or, in many cases, the complete reinvention of the fundamental components of a pneumatic system [49]. Examples include the numerous pneumatic actuators recently invented, already mentioned in the previous sub-section, or the work by Kortman et al. [87], which presents a novel soft and foldable bio-inspired suction cup, as well as the Soft Circuits Toolkit [88, 89], developed for educational purposes, where entire components (e.g., an oscillating valve) are made using soft materials. This thesis, in fact, focuses on the development of two elementary units, i.e., an actuator and a sensing unit, which are then applied in Service Robotics contexts.

It is important to clarify that many Soft Robotics technologies presented in academic research are still at a premature stage, and there is no clear or explicit reference to a specific application context where they can be employed. Nevertheless, they are extremely fascinating and represent the cutting-edge base research that, in the coming decades, could push Soft Robotics toward horizons still unknown today.

That said, in the remainder of this subsection, studies from the scientific literature will be described where there is an explicit and strong reference to one or more application contexts and where pneumatic soft robotic systems have provided an additional contribution compared to what was discussed in subsection 1.1. A summary of this analysis is provided in Figure 1.3. The macro-application contexts remain essentially the same, with the sole disappearance of construction robots, but the specific fields of use present substantial differences.

Regarding systems for medical applications, it is evident that the field of rehabilitative devices can only benefit from the introduction of soft structures [90]. There are also additional contexts, such as systems for minimally invasive surgery and cardiac devices, where soft pneumatic systems find their utility. A comprehensive review, dated 2019, was conducted in [91] and is revisited here with more recent developments.

Concerning rehabilitative systems, the main advantages of employing soft systems consist of mechanical compliance, which is already a characteristic of traditional pneumatic systems but is further enhanced by the use of soft materials, and low weight. Typical examples include wearable devices for wrist [92, 93, 94], finger [95, 96], elbow [97, 98, 99, 100], and ankle [101, 102, 103] rehabilitation, based on linear or bending soft pneumatic actuators of various types. Figure 1.4 shows the elbow exosuit in [100] compared to the exoskeleton by sanchez et al [104].

A smaller number of studies focus on the knee [105, 106] and shoulder [107], likely due to the larger size of the actuators required, resulting from the greater range of motion and higher force demand. This eliminates any advantage over systems based on traditional pneumatics. A completely new application context concerns the development of assistive cardiac devices [108]. These consist of a sleeve composed of multiple

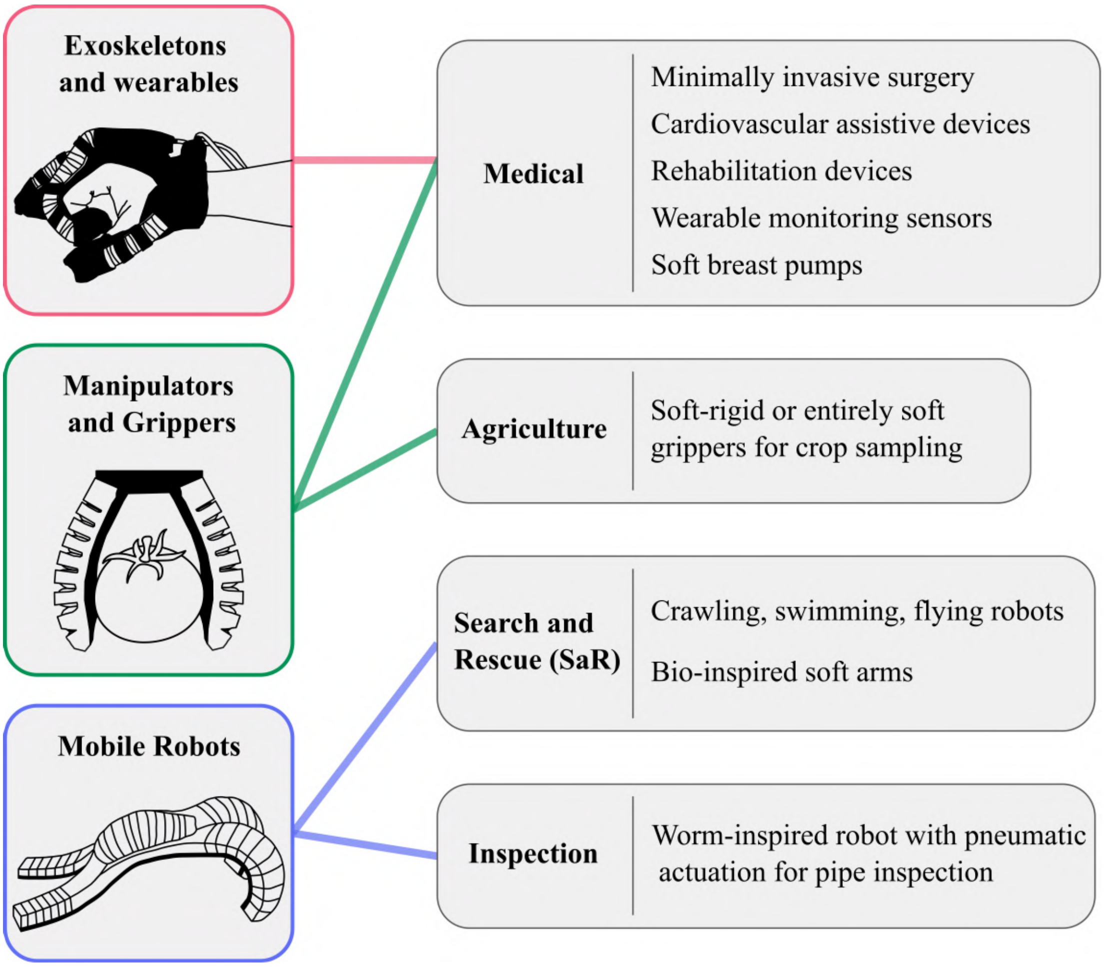

Figure 1.3: Soft pneumatic systems in the application macro-areas of Service Robotics according to IFR (professional application and medical).

actuators that cooperate to assist the heart during its contractions. A critical aspect, in the case of pneumatic actuators, is the possibility of air leaks, which would pose a serious risk to the patient's safety, as well as the difficulty of installing the air source. For this reason, although these technologies are particularly innovative, they are still far from the maturity and reliability required for medical devices.

Another innovative field compared to traditional pneumatics concerns minimally invasive surgery, which refers to surgical procedures where the surgical target is accessed through small entrances (laparoscopy, thoracoscopy) or natural orifices (endoscopy). The advantage of minimally invasive surgery lies, evidently, in the reduced impact on the patient, which has recently made it a major focus of research for the development of robotic devices. The operations generally required during surgery include grasping, divarication, dissection of the surgical target (e.g., an organ), and video recording to guide the medical staff [109]. These can be performed using a single unit, in

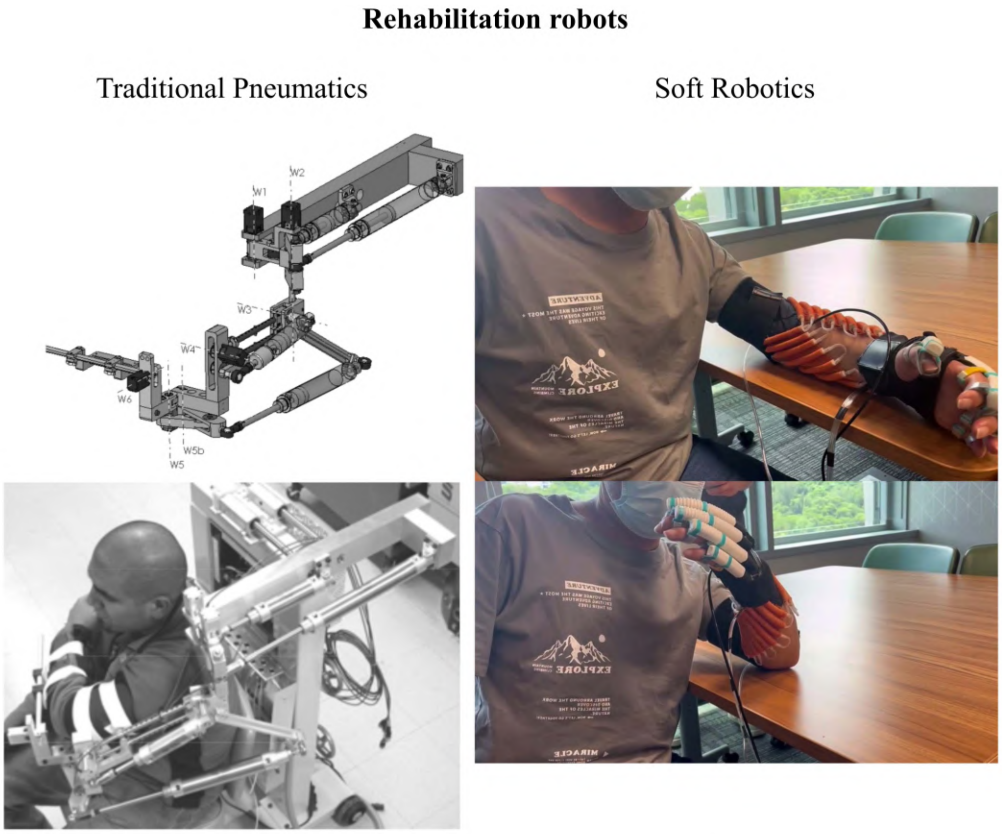

(a) (b)

Figure 1.4: **(a)** The pneumatic robot for upper limb rehabilitation by Sanchez et al. [104]. **(b)** The soft assistive exosuit for the elbow joint by Xie et al. [100].

which case it is referred to as single-port minimally invasive surgery, or using multiple instruments, each inserted through an appropriate incision in the patient’s body.

For example, Kortman et al. [87] presented a suction gripper that, being foldable, can be inserted into the patient’s body through a trocar. Further examples include the inflatable cable-driven robot by Yang et al. [110] and the bioinspired soft manipulator with variable stiffness by Ranzani et al. [109].

Additional applications concern the development of soft pneumatic monitoring sensors, such as the pouch sensor by DelPreto et al. [111], or the development of a breast pump with soft pneumatic interfaces to increase the breastfeeding mother’s comfort during device usage [112].

The ability to manipulate delicate objects, in turn, opens numerous application contexts for Precision Agriculture (PA) [113, 114]. Among the most recent works, Clark et al. [115] developed a PneuNet-based gripper inspired by a gecko’s foot, Tasneem and Oka [116] designed a soft stem holder for sweet pepper harvesting, and

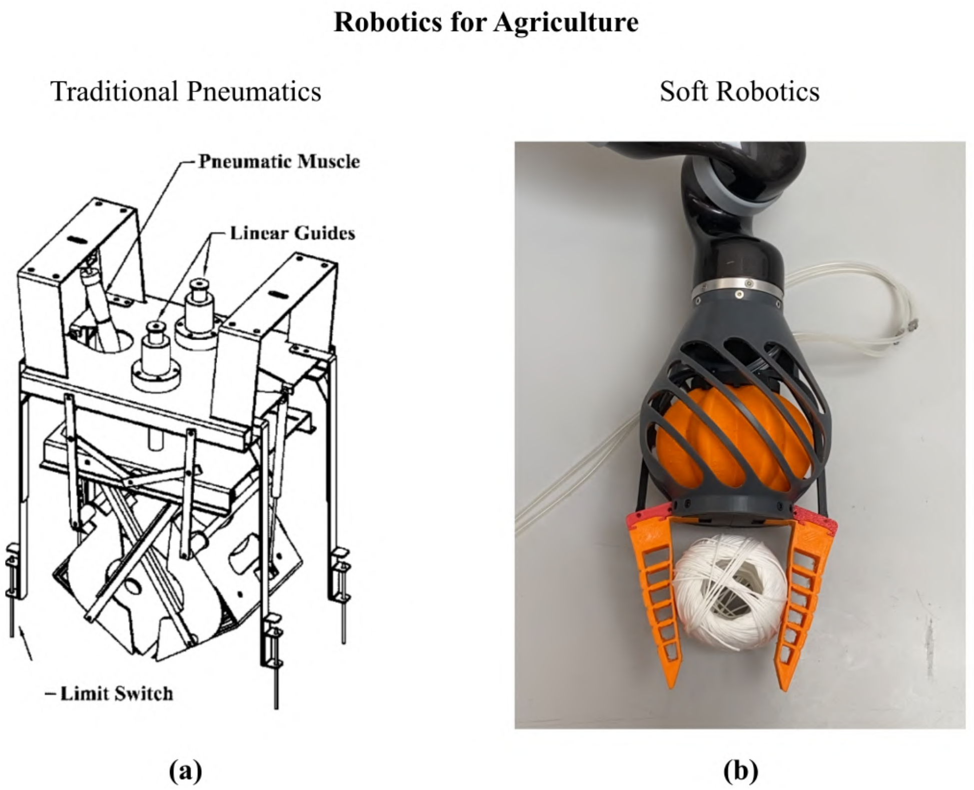

Figure 1.5: **(a)** The robotic end-effector for radicchio harvesting [26]. Reproduced under permission. Copyright John Wiley & Sons, 2006. **(b)** The BiSoft.Q gripper outlined in this thesis.

Navas et al. [117] proposed a gripper composed of diaphragm actuators for crop sampling.

The BiSoft.Q gripper, presented in the following chapter of this thesis, also falls within the technologies applicable to PA. It is therefore compared, in Figure 1.5, with the solution by Foglia and Reina [26] for radicchio harvesting.

Regarding the field of search and rescue, typical examples come from mobile robots, such as the numerous crawling, flying, and swimming soft pneumatic robots cited in the comprehensive review by Sun et al. [118]; and from soft manipulators, such as the continuum manipulator by Wen et al. [119], inspired by the giant anteater's tongue, the RoBoa soft manipulator with a maximum extension of 15 m, or the octopus-inspired soft arms [120, 121].

Finally, there are a limited number of examples of worm-inspired mobile robots for pipeline inspection, such as the work by Liu et al. [122] from 2022 or the one by Zhang et al. [123] from 2018.

Figure 1.6 compares the planar walker in [19] with the soft quadrupedal walker in [124]. The soft walker has been made using soft lithography in PDMS and it is essentially base on the PneuNet actuator. The traditional version is, on other hand, composed of a rigid structure actuated by pneumatic cylinders. Suction cups are used as *feet* to make contact with the ground.

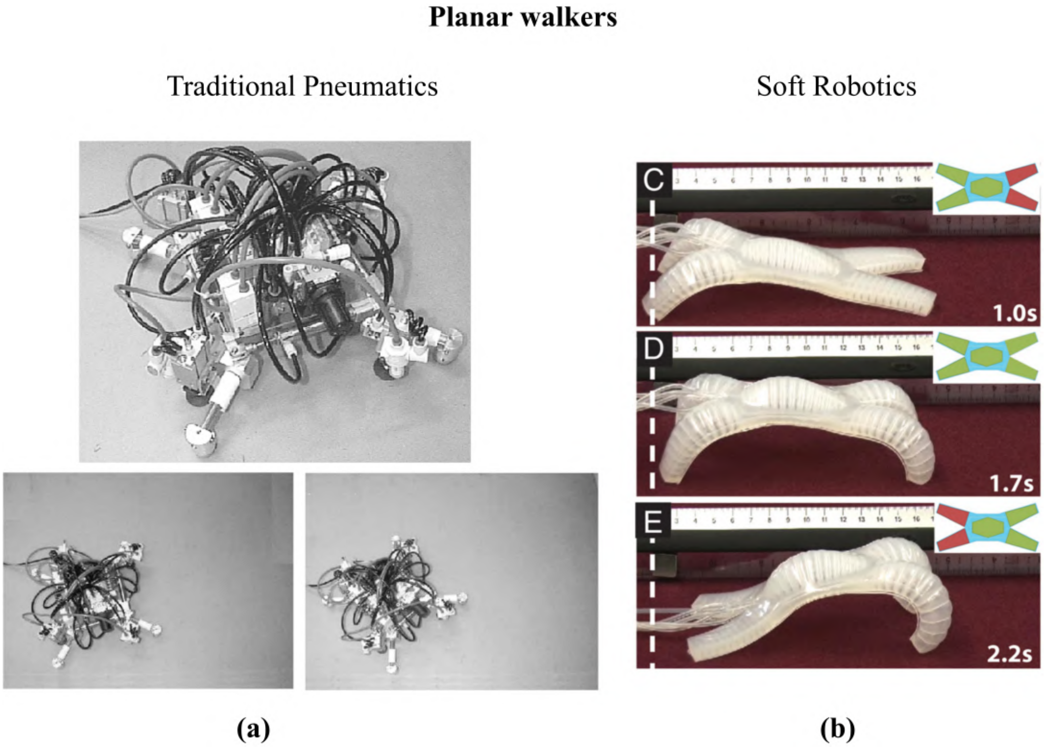

Figure 1.6: **(a)** The pneumatic planar walker by Chen and Yeo [19]. Reproduced under permission. Copyright Sage Publications, 2003. **(b)** The quadrupedal soft robot by Sheperd et al. [124].

## 1.3 Thesis outline

In the following chapter, an innovative soft pneumatic actuator will be presented. This actuator is linear and bi-directional, i.e., it can achieve both contraction and extension with positive gauge pressure. Chapter 3, on the other hand, describes the use of Soft Pneumatic Sensing Chambers (SPSCs) for robotics and haptic device applications. The structure of both chapters is as follows:

- Discussion of related research and innovative aspects of the presented work.
- Design methodology and the effect of key parameters, e.g., geometric parameters, on system performance, e.g., static characteristics or energy consumption.
- Experimental characterization.
- Application contexts.

For Chapter 2, some analytical sections are collected and described in Appendix A.

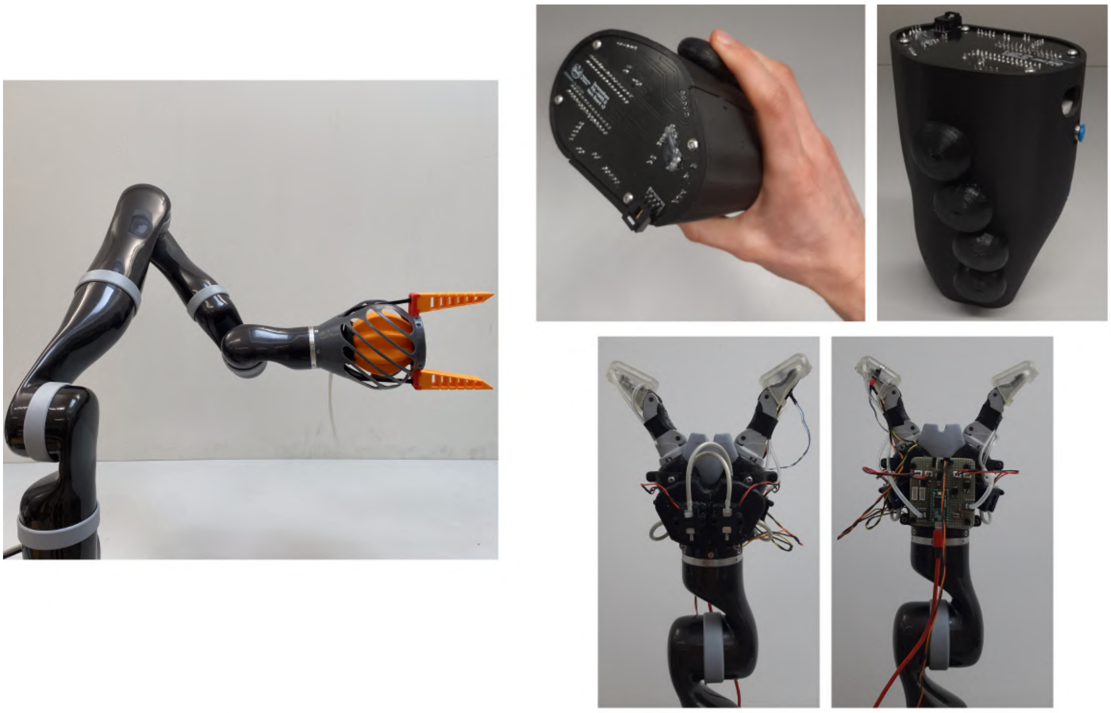

(a) (b)

Figure 1.7: **(a)** The BiSoft.Q gripper presented in subsection 2.4.2. **(b)** The PAL-HAND.Q haptic device of subsection 3.4.2 (top) and the PneuTact.Q device described in section 3.4.1 (bottom).

# Chapter 2

# A Soft Pneumatic Linear and Bi-Directional Actuator

Double-acting or bi-directional Soft Pneumatic Actuators (SPAs), capable of deforming in both directions under positive gauge pressure [125], are well-documented in the literature. These actuators operate on a principle similar to traditional double-acting pneumatic cylinders, wherein two or more internal chambers are pressurized to achieve the desired motion. The earliest reference to a double-acting soft linear actuator, featuring two internal chambers, is found in Morin's 1953 patent [126], later cited by Daerden in 1999 [127]. Designed to control measuring systems or valves, the actuator diaphragms were constructed by embedding reinforcing fibers into a rubber matrix. In 2014, Ferraresi et al. [128] built upon this concept with the BiFAc3 actuator, which could generate both push and pull forces using three internal chambers. This design evolved from the BiFAc2, which had two internal chambers, by incorporating a third chamber to neutralize the intermediate diaphragm during pulling behavior. The operational principle remained based on the elastic deformation of a fiber-reinforced rubber diaphragm, with a maximum working pressure of 75 kPa.

Other variations of double-acting or bidirectional SPAs are inspired by the McKibben muscle. In these designs, an external braiding sleeve constrains the deformable bladder, preventing uncontrolled membrane deformation. The actuator's behavior is determined by the braiding angle, which can be tailored to produce either contraction or extension of the Pneumatic Artificial Muscle (PAM) [129]. Al-Fahaam et al. combined contraction and extension PAMs to create a bi-directional linear muscle achieving a contraction ratio of approximately 30 % at a working pressure of 500 kPa [130]. In comparison, the multifunctional McKibben muscle developed by Hassan et al. utilized a single McKibben actuator with an adjustable braiding angle to enable bidirectional functionality. Their study also investigated how the actuator's geometric parameters influenced its performance, achieving a contraction ratio of approximately 40 % and maximum forces of around 40 N at relatively low pressures (100-200 kPa) for increased safety [35].

Despite advancements in linear and bi-directional SPAs, several limitations remain. For instance, actuators using reinforced diaphragms, where deformation is converted into elongation or contraction, suffer from energy losses during actuation cycles due to the material's hysteretic behavior. Similarly, McKibben muscles face challenges related to frictional effects from the relative motion between the braided sleeve and bladder, along with a threshold pressure below which no actuation occurs [131]. Furthermore, the antagonist chamber approach in [130] is prone to buckling phenomena during pneumatic bladder compression, complicating the realization of purely linear actuator motion.

This chapter details the development of a SPA, named BiSoft.Q, that exhibits bi-directional linear motion when pressurized. The actuator is based on antagonistic chambers, and it is based on the principles of BiFAc3, previously developed and patented by Quaglia, Ferraresi and Franco [128]. The novel SPA modifies the BiFAc3 geometry by introducing pleated geometries to improve performance both in terms of force and stroke output and in terms of energy consumption. The BiSoft.Q has been designed in such a manner that it is compatible with additive manufacturing techniques, and it allows for monolithic structures to be manufactured.

The BiSoft.Q conceptualization and development has been discussed by Duretto in 2023 [132] and later published by Colucci, Duretto and Quaglia in 2023 [133].

In the following, a simplified analytical model is introduced to predict the actuator's performance, including stroke, force output, and energy consumption. The results of this model are analysed to derive key design guidelines.

The chapter also covers an initial experimental phase focused on prototyping the actuator using easily reproducible additive manufacturing techniques. Experimental results are included to assess actuator performance. Additionally, there is a mention in the theoretical framework of the implementation of strategies aimed at reducing the actuator energy consumption.

Finally, a comparison with similar solutions in the literature is provided, alongside a case study that explores potential applications in service robotics, specifically in the development of an adaptive gripper for a commercial robotic manipulator.

## 2.1 BiSoft.Q concept

To make a SPA bi-directional, either it is a linear [128, 35], bending [134, 135, 136, 54] or twisting actuator, two or more internal chambers have to be realized and properly pressurized in order to deform the actuator in both directions of motion. In the case of BiSoft.Q, bi-directionality is provided by the combination of a pleated membrane that unfolds and thus contracts when pressurised [137, 138], and a bellows that expands linearly when inflated, as shown in Figure 2.1 (a). Those membranes are co-axial and linked by two end plates, thus resulting into two different and sealed internal chambers which can be independently pressurized.

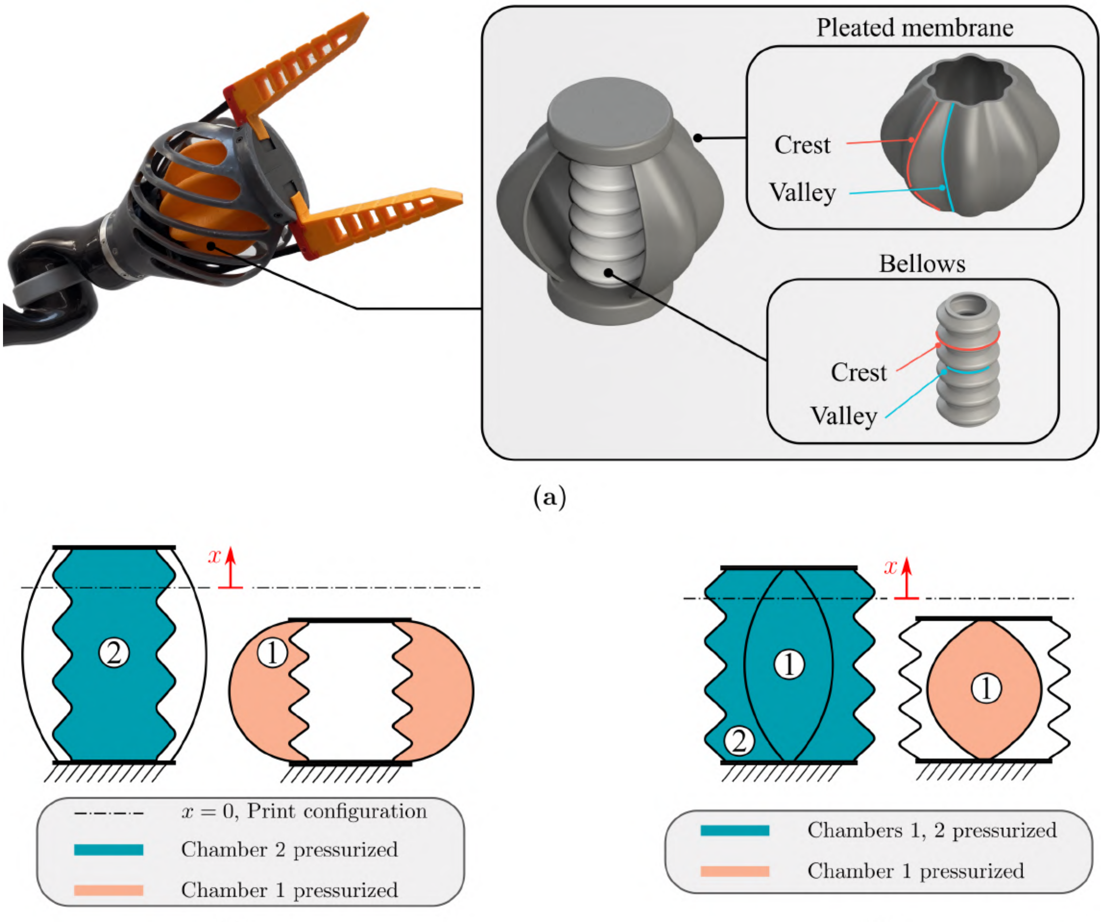

(a)

(b)

(c)

Figure 2.1: **(a)** A two-finger compliant gripper driven by the BiSoft.Q type A actuator. **(b)** Schematic of BiSoft.Q Type A functioning under free-load condition in the longitudinal plane. The lower plate is fixed, the upper plate is free to move. **(c)** Type B functioning.

Both membranes take advantage of the sequential alternation of crest and valley fibres to create a corrugated geometry which can fold (or unfold) when elongated (or squeezed), but with a clear difference on how these fibres are aligned. In other words, the pleated membrane can be considered as the imitation of a bellows where the crest and valley fibres are now aligned longitudinally. It is critical that both the longitudinal and radial fibres of the pleated membrane and bellows remain as inextensible as possible. This is necessary to prevent a volumetric and uncontrolled expansion, which would result in no actuator elongation.

This principle of antagonist chambers can thus be used to design two different typologies of BiSoft.Q actuator, depending on how the membranes are distributed. For BiSoft.Q type A in Figure 2.1 (b), the outer chamber, here chamber 1, is in between the pleated membrane and the bellows, while chamber 2 is the bellows inner chamber. For BiSoft.Q type B in Figure 2.1 (c), instead, the pleated membrane is located inside the bellows, and the chambers numbering is flipped. As a main distinction among the operating principle of the two actuators, the elongation in type B is achieved by pressurizing both chambers 1 and 2, thus making the inner pleated membrane neutral and devoid of any pressure load [128]. Besides, the same principle can't be applied to type A while contracting, for it would result into a lower free load contraction caused by the pressure force acting on both the end caps, as it will be further explained.

### 2.1.1 Actuator geometry

Figure 2.2 shows the primitive curves for the BiSoft.Q type A along both the longitudinal $<\hat{r}, \hat{k}>$ and cross $<\hat{i}, \hat{j}>$ planes. Those curves represent the middle axis of both the bellows and the pleated bladder.

Starting from the B-B cross-sectional plane, the geometry of the unit pleat is composed of two arcs, labelled as I and III in the figure, connected by an intermediate and tangent segment II. The resulting profile is mirrored with respect to $\hat{r}$ to define the unit pleat, thus repeated $N_p$ times in a circular pattern centred in $O'$. The cross-sectional geometry is eventually extruded along $\hat{k}$ axis, guided by a first primitive valley arc of length $l_{v,p}$ and a second $l_{c,p}$ crest arc. The latter lies in the $<\hat{j}, \hat{k}>$ plane, therefore it is not represented in Figure 2.2.

The resulting geometrical parameters that entirely describe the BiSoft.Q geometry are provided in Table 2.1 along with a short description of them. It is worth noting that De Pascali et al. [139] proposed a similar approach to analytically define a 3D printed monolithic and single-direction PPAM, although the unit pleat is composed of two elliptical arcs without any tangency constraints. Furthermore, the authors assert that the definition of the cross-sectional geometry described in this study, which namely depends on the set $[N_p, R_{ie,p}, R_{oe,p}, R_{ce,p}, R_{ve,p}]$, is more explicit than the set of ellipse centres and semi-axes defined in [139]. Additional information regarding the analytical definition of the BiSoft.Q undeformed geometry are provided by the authors in Appendix A.

## 2.2 Design methods

The Bisoft.Q design is done by assessing the effect of the actuator geometrical parameters on the static apply curve, i.e. the force versus stroke graph under static conditions, its air-mass consumption and efficiency. To this aim, the actuator geometry is analytically defined and the actuator static performance curve is obtained by assuming the actuator deformed configuration can be estimated *a priori* as a function of its stroke and geometrical parameters. The proposed approach mainly addresses the pleated membrane, whose geometry definition is not a trivial concern, while the bellows membrane is adapted afterwards once the BiSoft.Q dimension and type are defined.

In developing the original PPAM, F. Daerden used Timoshenko's theory to calculate the geometry, stress state and tensile forces of the actuator. The latter was a function of the supply pressure, the undeformed length of the PPAM and a dimensionless function, depending only on the contraction rate, geometry and material behaviour [127]. However, this approach is not applicable to the BiSoft.Q due to differences in the geometry of the two actuators. Consequently, a simplified model was employed to describe the Bisoft.Q geometry as a function of its linear stroke $x$.

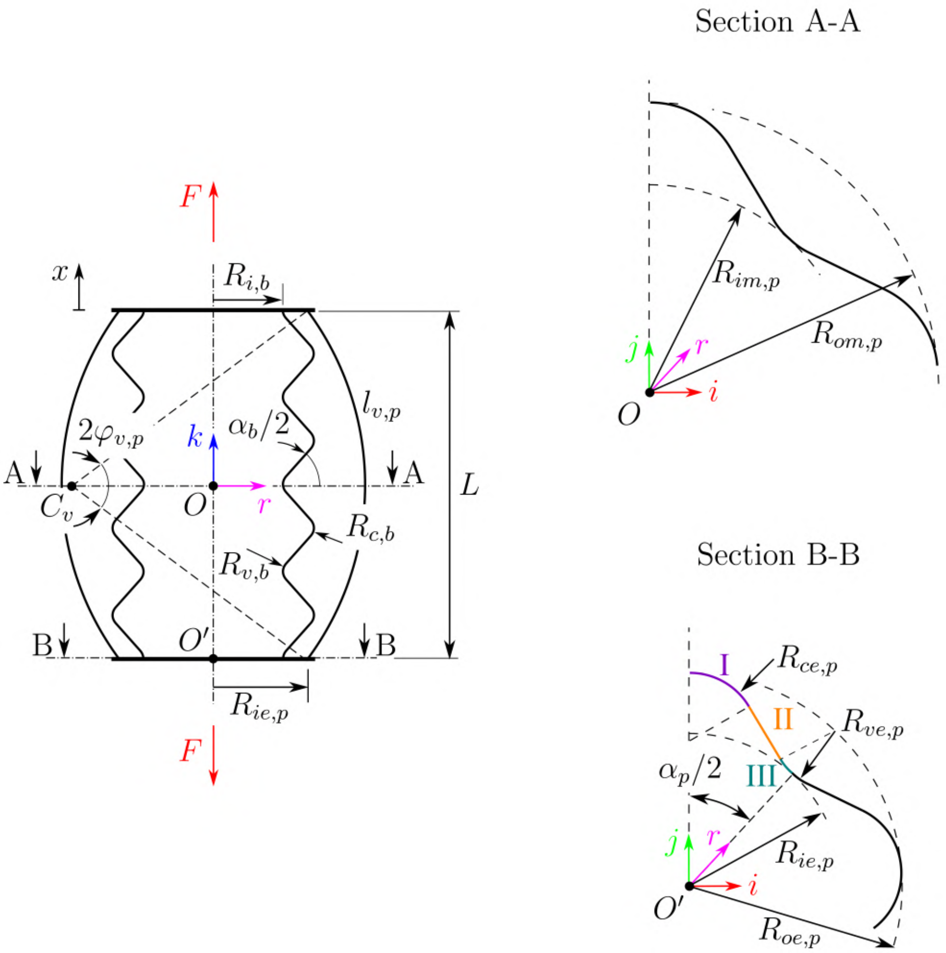

Figure 2.2: BiSoft.Q type A nominal geometry shown in the longitudinal, median and end section planes. The stroke $x$ is positive when the BiSoft.Q elongates. $F$ is the force that keeps the BiSoft.Q in static equilibrium, i.e. it is positive when the actuator shows contractile behavior (pulling forces).

### 2.2.1 Simplifying assumptions

Let introduce the following simplifying model assumptions to analytically compute the BiSoft.Q deformed configuration:

- The elastic properties of the pleated membrane are considered negligible.
- Both the terminal caps can only translate along $\hat{k}$ axis, i.e. the BiSoft.Q behaves as a pure linear actuator, as shown in Figure 2.3 (a) for the pleated membrane and in (c) for the bellows.
- Due to the pleats circular pattern and the bellows axial-symmetry, the problem can be reduced to the evaluation of the single pleat deformed configuration, here considered as the portion of actuator in between two subsequent longitudinal crest fibres, as depicted in Figure 2.3 (b).
- The three angles $\alpha_p$ in Figure 2.2 and $\delta$, $\gamma$ in Figure 2.3 (b), remain constant. Thus, the crest, valley and the two tangency points can only move along a straight line along the radial direction when the pleated membrane is pressurized.

Table 2.1: BiSoft.Q geometrical parameters describing both the pleated membrane and the bellows.

| | **Name** | **Description** |
|---|---|---|
| **Pleated membrane** | $L$ | Longitudinal length of the actuator when printed ($x$ =0) |
| | $l_{v,p}$ | The valley longitudinal arc length |
| | $l_{c,p}$ | The crest longitudinal arc length |
| | $R_{ie,p}$ | The radius of the arc defined in $B-B$ plane, centred in $O'$ and intersecting the longitudinal valley fibres |
| | $R_{ve,p}$<br>$R_{ce,p}$ | The radii of arcs I and II |
| | $R_{im,p}/R_{om,p}$ | The ratio of the inner valley and outer crest arcs defined in $B-B$ plane |
| | $N_p$ | The number of pleats |
| **Bellows** | $R_{i,b}$ | The bellows radius defined on the B-B plane |
| | $\alpha_b$ | The angle between two subsequent bellows folds |
| | $R_{v,b}$<br>$R_{c,b}$ | The valley and crest fillet radii of the bellows |
| | $N_b$ | The number of bellows folds |

- The longitudinal fibres of the pleated membrane, along with the valley circular fibres of the bellows are considered as inextensible, i.e. the actuator elongation (or contraction) solely relies on the membranes folding/unfolding process.

It is worth noting that the first assumption was not extended to the bellows, since the method proposed by Wang et al. [140] was used to estimate its axial elastic properties.

This deformed geometry evaluation method differs to what done in [139], where an optimisation method was employed to derive the PPAM deformed configuration, and the constraint of longitudinal fibres inextensibility was relaxed with inequality constraints. Further details on the deformed geometry estimation can be found in Appendix A.1.

### 2.2.2 Static apply curve computation

As shown in Figure 2.2, let $x$ be the BiSoft.Q stroke along $\hat{k}$ axis and $F = F(x)$ the external force acting on the actuator to guarantee the static equilibrium at a specific value of $x$. The following convention is thus assumed:

$$x \begin{cases} < 0 & \text{contraction} \\ = 0 & \text{print configuration} \\ > 0 & \text{elongation} \end{cases} \qquad F(x) \begin{cases} < 0 & \text{pushing} \\ > 0 & \text{pulling} \end{cases} \tag{2.1}$$

Under the assumption of inextensibility of the longitudinal fibres of the pleated membrane, the maximum stroke $s = x_{\max} - x_{\min}$ of the BiSoft.Q is dependent on the length of the valley fibres, since $l_{v,p} < l_{c,p}$ by geometrical construction. As depicted in Figure 2.3 (a), it is possible to provide an initial estimate of $s$ by considering the configuration of the maximum displacement, $x_{\max}$, as that in which the valley fibres are fully stretched and that of the minimum displacement, $x_{\min}$, as that in which the valley fibres assume a half-circle configuration.

$$s = x_{\max} - x_{\min} \leq (l_{v,p} - L) - \left(\frac{2\, l_{v,p}}{\pi} - L\right) = l_{v,p}\left(1 - \frac{2}{\pi}\right) \approx 0.36\, l_{v,p} \tag{2.2}$$

For both BiSoft.Q types, let now consider chamber 1 pressurized at the gauge pressure level $p_{s,1} = P_{s,1} - P_{\text{amb}}$. As shown in Figure 2.4 (a), let $\boldsymbol{\Sigma}(\vartheta_1, \vartheta_2, x)$ be the analytical definition of the $N$-th pleat, that is function of the two polar coordinates $(\vartheta_1, \vartheta_2)$ and the stroke $x$:

$$\boldsymbol{\Sigma}(\vartheta_1, \vartheta_2, x) = \boldsymbol{OW}(\vartheta_1, \vartheta_2, x) = X\,\hat{\imath} + Y\hat{\jmath} + Z\,\hat{k} \tag{2.3}$$

This formulations allows to calculate the surface integral of the pressure distribution acting on the $N$-th pleat to obtain the pressure force $\mathbf{F_p}(x)$ :

$$\mathbf{F_p}(x) = \int_{\Sigma} p_{s,1}\, \hat{n}_1\, d\Sigma = \int_{-\alpha_p/2}^{\alpha_p/2} \int_{-\vartheta_{2,\max}}^{\vartheta_{2,\max}} p_{s,1} \hat{n}_1 \left\| \frac{\partial \boldsymbol{\Sigma}}{\partial \vartheta_1} \times \frac{\partial \boldsymbol{\Sigma}}{\partial \vartheta_2} \right\| d\vartheta_1 d\vartheta_2 \tag{2.4}$$

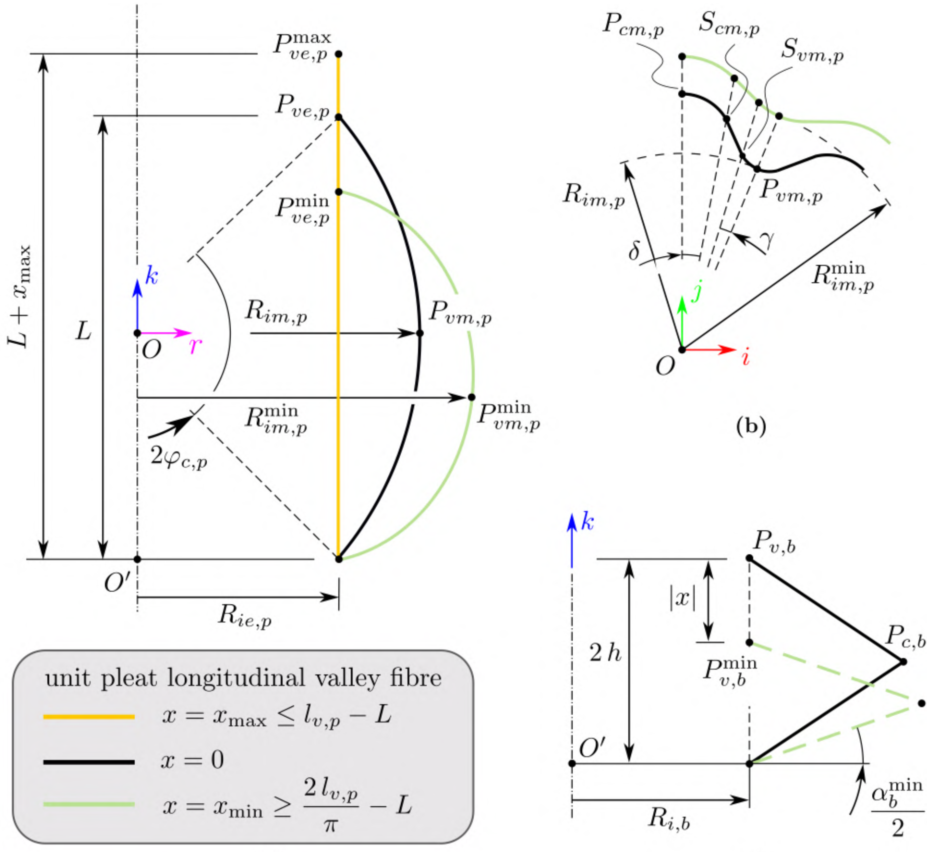

(a) (b) (c)

Figure 2.3: **(a)** Longitudinal crest fibre under deformation. $x = 0$ is the nominal (print) configuration. **(b)** Unit pleat deformation in the median cross-sectional plane. Pink line represents the $x = x_{\min}$ configuration. **(c)** Unit bellows fold under deformation in the longitudinal plane.

where $\hat{n}_1$ is the unit vector that is normal to the surface:

$$\hat{n}_1(\vartheta_1, \vartheta_2, x) = -\frac{\dfrac{\partial \boldsymbol{\Sigma}}{\partial \vartheta_1} \times \dfrac{\partial \boldsymbol{\Sigma}}{\partial \vartheta_2}}{\left\| \dfrac{\partial \boldsymbol{\Sigma}}{\partial \vartheta_1} \times \dfrac{\partial \boldsymbol{\Sigma}}{\partial \vartheta_2} \right\|} \tag{2.5}$$

As depicted in Figure 2.4 (b), thanks to the model symmetry, two components of $\mathbf{F_p}$ are null:

$$\mathbf{F_p} \cdot \hat{k} = \mathbf{F_p} \cdot \hat{\imath} = 0 \tag{2.6}$$

and the force is purely directed along $\hat{\jmath}$:

$$\mathbf{F_p}(x) = F_p(x)\,\hat{\jmath} \tag{2.7}$$

Let assume the crest fibres as the main responsible of the load transmission. The free-body diagram depicted in Figure 2.5 (a) allows the computation of the tension $T$ acting on the fibre as:

$$T(x) = \frac{F_p(x)}{2\,\sin(\varphi_{c,p}(x))} \tag{2.8}$$

and, eventually, the free-body diagram of the actuator terminal cap leads to the estimation of the pulling force $F(x) > 0$:

$$F(x) = \frac{N_p\,F_p}{2\,\tan(\varphi_{c,p}(x))} - F_a - F_{\text{elastic, b}}(x) \tag{2.9}$$

where the first term projects $T$ along $\hat{k}$, and also takes into account the combined effect of the $N$ pleats. On other hand, the second term represents the antagonistic pressure force acting on the end cap, that is equal to:

$$F_a = A_a\,p_{\text{s},1} \tag{2.10}$$

The antagonistic area for BiSoft.Q type A is represented in Figure 2.5 (b), while Figure 2.5 (c) shows the same entity but for type B. Due to the counter-acting effect of $F_a$, the inner chamber 2 of type A is not pressurized during the BiSoft.Q pulling behaviour, for it would increase $A_a$ with the minor benefit of making the bellow membrane neutral [126, 128]. The analytical computation of $A_a$ for both BiSoft.Q types can be retrieved in Appendix A.2. Lastly, as cited above regarding the model simplifying assumptions, the latter term $F_{\text{elastic, b}}$ represents the bellows intrinsic elasticity [140].

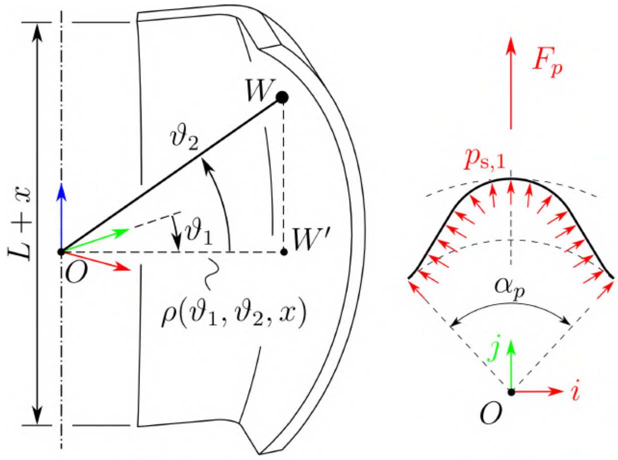

(a) (b)

Figure 2.4: **(a)** Analytical description of the unit pleat in polar coordinates. **(b)** Pressure force acting on the unit pleat represented in the median cross-sectional plane. Thanks to the model symmetry, the resulting components along $\hat{\imath}$ and $\hat{k}$ are null.

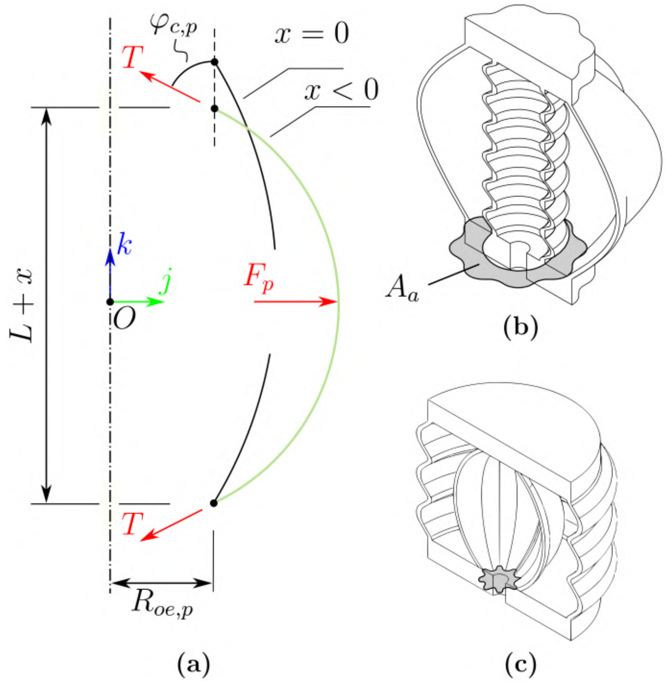

Figure 2.5: **(a)** Free-body diagram of the forces acting on the unit longitudinal crest fibre. **(b)** Antagonistic area for BiSOft.Q type A, **(c)** type B.

Let now consider the BiSoft.Q pushing mode, i.e. $F(x) < 0$. For BiSoft.Q type A, $F(x)$ arises from the pressurization of the sole chamber 2 while, for type B, both the internal chambers can be pressurized to make the inner pleated membrane neutral. By denoting $p_{s,2}$ as the supply chamber for the push mode and by employing the simplifying assumptions cited above, the calculation of the push force $F(x) < 0$ is straightforward:

$$F(x) = -\pi\, R_{i,b}^2\, p_{\text{s,2}} + F_{\text{elastic,b}}(x) \tag{2.11}$$

The two resulting equations, namely Equation (2.9) and Equation (2.11), describe the static-apply behaviour of the BiSoft.Q for a specific set of geometrical parameters in Table 2.1. The initial estimation of the maximum stroke, as given in Equation (2.2), can be rescaled within the range of the pulling (or pushing) force, provided that it is non-null and consistent with the adopted sign convention.

### 2.2.3 Energy analysis

Apart from the aforementioned static apply curve, the analytical definition of both the BiSoft.Q membranes as a function of the linear stroke $x$ also allows the calculation of the actuator internal volumes, as described in Appendix A.2. Once the internal volumes $V_{ch.[1,2]}(x)$ are known, the BiSoft.Q energy performance can be estimated in terms of air mass consumption and actuator efficiency. It is worth uderlining that these terms depend on the actuator geometry as well as on the supply line lay-out. In this sense, methodologies such as the filling of the chambers with either granular media or incompressible fluid, or the internal (or external) exhaust air recirculation, would result into higher energy performances [141, 142, 143, 144]. However, these strategies will not be assessed in this paper and a simplified actuator control using a 5-way 2-position spool valve will be considered in the remainder of this work.

Let consider the BiSoft.Q type A in its elongated configuration $x_{\text{max}}$ with chamber 1 connected to the exhaust and chamber 2 pressurized at $P_s$ from the supply. Let now switch the directional valve. The amount of air mass that is injected in chamber 1 to reach the contracted configuration $x_{\text{min}}$ is:

$$\Delta M_{\text{ch. 1}} = \frac{P_s\, V_{\text{ch. 1}}(x_{\text{min}}) - P_{\text{amb}}\, V_{\text{ch. 1}}(x_{\text{max}})}{R\, T_{\text{amb}}} \tag{2.12}$$

where $P_{\text{amb}}$ is the ambient pressure, $R$ (J kg$^{-1}$ K$^{-1}$) the air specific constant and $T_{\text{amb}}$ (K) the air absolute temperature imposed from the supply. Please notice the temperature of the air from the supply $T_s$ is assumed to be equal to $T_{\text{amb}}$. A similar formulation can be derived for chamber 2 during the backward motion, and the total amount of air mass that is spent on a full cycle is equal to:

$$\Delta M = \Delta M_{\text{ch. 1}} + \Delta M_{\text{ch. 2}} = \frac{(P_{\text{s}} - P_{\text{amb}})(V_{\text{ch. 1, d}} + V_{\text{ch. 2, d}})}{R\, T_{\text{amb}}} + \frac{P_{\text{s}}(\Delta V_{\text{ch. 1}} + \Delta V_{\text{ch. 2}})}{R\, T_{\text{amb}}} \tag{2.13}$$

where the following substitutions:

$$V_{\text{ch. 1}}(x_{\text{min}}) = V_{\text{ch. 1}}(x_{\text{max}}) + \Delta V_{\text{ch. 1}} = V_{\text{ch. 1, d}} + \Delta V_{\text{ch. 1}} \tag{2.14}$$

$$V_{\text{ch. 2}}(x_{\text{max}}) = V_{\text{ch. 2}}(x_{\text{min}}) + \Delta V_{\text{ch. 2}} = V_{\text{ch. 2, d}} + \Delta V_{\text{ch. 2}} \tag{2.15}$$

have been made to highlight the dead volumes of the actuator.

The BiSoft.Q efficiency over a cycle can be eventually estimated by considering the ratio between the output $\mathscr{W}_{\text{out}}$ and input work $\mathscr{W}_{\text{in}}$ as follows:

$$\eta = \frac{\mathscr{W}_{\text{out,ch.1}} + \mathscr{W}_{\text{out,ch.2}}}{\mathscr{W}_{\text{in}}} \tag{2.16}$$

with $\mathscr{W}_{\text{out,ch.1}}$ and $\mathscr{W}_{\text{out,ch.2}}$ indicating the exerted work respectively during the pulling phase and pushing phase:

$$\mathscr{W}_{\text{out,[ch.1,ch.2]}} = \int_{x_{\text{min}}}^{x_{\text{max}}} |F(x)|\, dx \tag{2.17}$$

and $\mathscr{W}_{\text{in}}$ denoting the ideal work of compression, here evaluated as the isoentropic head, i.e. by assuming the air is compressed and cooled back to the ambient temperature before being sent to the BiSoft.Q actuator:

$$\mathscr{W}_{\text{in}} = \Delta M\, R\, T_{\text{amb}} \frac{n}{n-1} \left( \left( \frac{P_{\text{s}}}{P_{\text{amb}}} \right)^{\frac{n-1}{n}} - 1 \right) \tag{2.18}$$

where $n$ is the adiabatic coefficient for air and $\Delta M$ deriving from Equation 2.13.

A similar method applies to BiSoft.Q type B, with the distinction that chamber 1 is also pressurized during the pushing phase.

### 2.2.4 Model results and design guidelines

The BiSoft.Q analytical model can be employed during the actuator design process to obtain an estimation of its static performance. However, the actuator's complex shape and the considerable number of parameters outlined in Table 2.1 may present a challenge in this process. This subsection outlines the impact of the significant geometrical parameters on the BiSoft.Q shape and behaviour, thereby providing a few useful design guidelines.

What has been the subject of discussion in this section and in Appendix A-A.2 was implemented in Matlab environment and distributed as open-source code[1]. The software can compute the BiSoft.Q nominal and deformed geometry and all discussed physical quantities with a execution time of 0.9 seconds[2].

Regardless of the BiSoft.Q type, it can be stated that the actuator size can be imposed by its outer radius on the terminal section B-B, i.e $R_{ie,p}$ for type A and $R_{i,b}$ for type B, and its nominal length $L$. With reference to the working modes of Figure 2.1 (b), for instance, if $R_{ie,p}$ is imposed, $R_{i,b}$ corresponds to the higher permissible value without any interference with the pleated membrane. The ratio $L/(2\,R_{ie,p})$, or $L/(2\,R_{i,b})$ for type B, defines the slenderness of the actuator, where $L/(2\,R_{ie,p}) > 1$ corresponds to slim shape with high strokes and low forces, whilst the other case means high force actuator with a relatively low stroke. In the case of the original PPAM actuator [138], the antagonistic force and the dead volumes inevitably result in PPAMs with a slenderness ratio much greater than 1, as also resulting in other works [139, 145]. This design limit does not apply for the BiSoft.Q type A, as the internal bellows membrane reduces the antagonistic area and dead volumes while contracting, thereby preventing the aforementioned limitation.

Once $L$ is fixed, the length of both longitudinal crest and valley fibres of the pleated membrane can be expressed by the two dimensionless ratios:

$$\frac{l_{v,p}}{l_{c,p}} \leq 1 \tag{2.19}$$

$$\frac{2}{\pi} \leq \frac{L}{l_{c,p}} \leq \frac{l_{v,p}}{l_{c,p}} \tag{2.20}$$

---

[1] https://github.com/seromedises-PoliTo/BiSoft.Q-main

[2] Tested on a Dell XPS with Intel i7-10510U@1.80 GHz processor. The computation time increases to 30 seconds when the air mass consumption is also estimated.

where the upper limit for the first ratio is derived from the intrinsic definition of crest and valley fibres, while the lower limit $2/\pi$ for the latter is obtained through the simplified Equation 2.2.

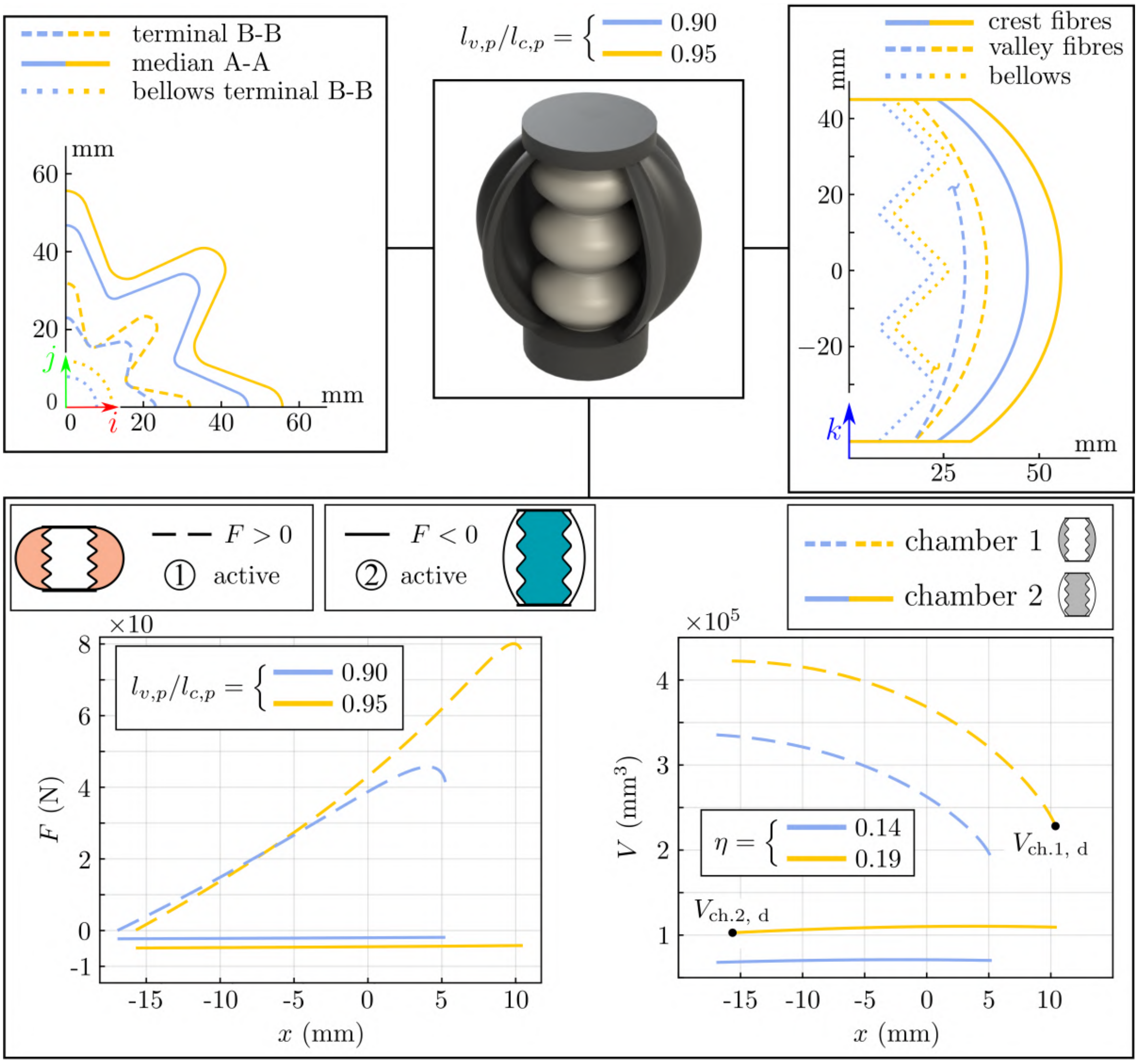

Figure 2.6: Results of the design methodology for two BiSoft.Q type A actuators with two different values of $l_{v,p}$. $L$ =90 mm, $l_{c,p}$ =106 mm, $R_{ie,p}$ =17 mm, $R_{im,p}/R_{om,p}$ =0.65, $N_p$ =8, $\alpha_b$ =45 deg, $R_{v,b}$ =0.5 mm, $R_{c,b}$ =2 mm. For the first case where $l_{v,p}/l_{c,p}$ =0.9, $l_{v,p}$ =95 mm, $R_{i,b}$ =12 mm. For the latter case $l_{v,p}/l_{c,p}$ =0.95, $l_{v,p}$ =100 mm, $R_{i,b}$ =8 mm. The dead volumes $V_{\text{[ch. 1, ch. 2], d}}$ are highlighted only for $l_{v,p}/l_{c,p} = 0.95$. The selected material to compute the bellows stiffness is TPU 82A. The cross-sectional planes A-A and B-B are defined in Figure 2.2.

Figure 2.6 shows an example of the effect of $l_{v,p}$ on both the geometry and static performance of a BiSoft.Q type A. It is notable that this type of actuator exhibits a pronounced imbalance between the pulling and pushing forces, a phenomenon that will be also discussed in section 2.4. Other than that, an higher value of $l_{v,p}$ leads to longitudinal valley fibres that are more bended in the nominal configuration $x = 0$, and thus to higher values of $R_{im,p}$. Since the $R_{im,p}/R_{om,p}$ ratio is kept fixed, the longitudinal crest fibres are translated along $\hat{j}$ without modifying their geometry, but with an higher radial encumbrance. Higher values of $l_{v,p}$ also lead to higher $x_{\max}$ while keeping $x_{\min}$ almost constant. Finally, there is an overall improvement in the efficiency of the actuator, because although the air consumption is higher, the output work $W_{\text{out}}$ is much greater. It is worth citing the longitudinal fibres bending, that is quantified by angles $\varphi_{[c,v],p}$, is strongly limited by the manufacturing process, as it will further explained in the next section.

Opposite results can be obtained by considering the effect of $l_{c,p}$, i.e. higher levels of force and efficiency correspond to lower values of $l_{c,p}$, as showed in Figure 2.7 for a geometry which is similar to the one in the previous figure.

The ratio $R_{im,p}/R_{om,p}$ is the last geometrical parameter with significant influence on the static performance of the actuator. A lower value of this ratio would mean an higher difference between the inner and outer radius of the pleated membrane in the intermediate cross section. In turn, this would lead to more pronounced pleats, higher dead volumes for chamber 1, but much grater pulling forces, with the general improvement in the actuator efficiency. This effect is depicted in Figure 2.8 for a BiSoft.Q type B geometry.

Lastly, the fillet radii $R_{[v,c]e,p}$ do not have any significant influence on what discussed above, thus they can be chosen to correctly complete the pleated geometry. The same statement also apply for $R_{[v,c],b}$ and the bellows overhang $\alpha_b$, which depend more on technological considerations than on their effect on the stiffness of the bellows.

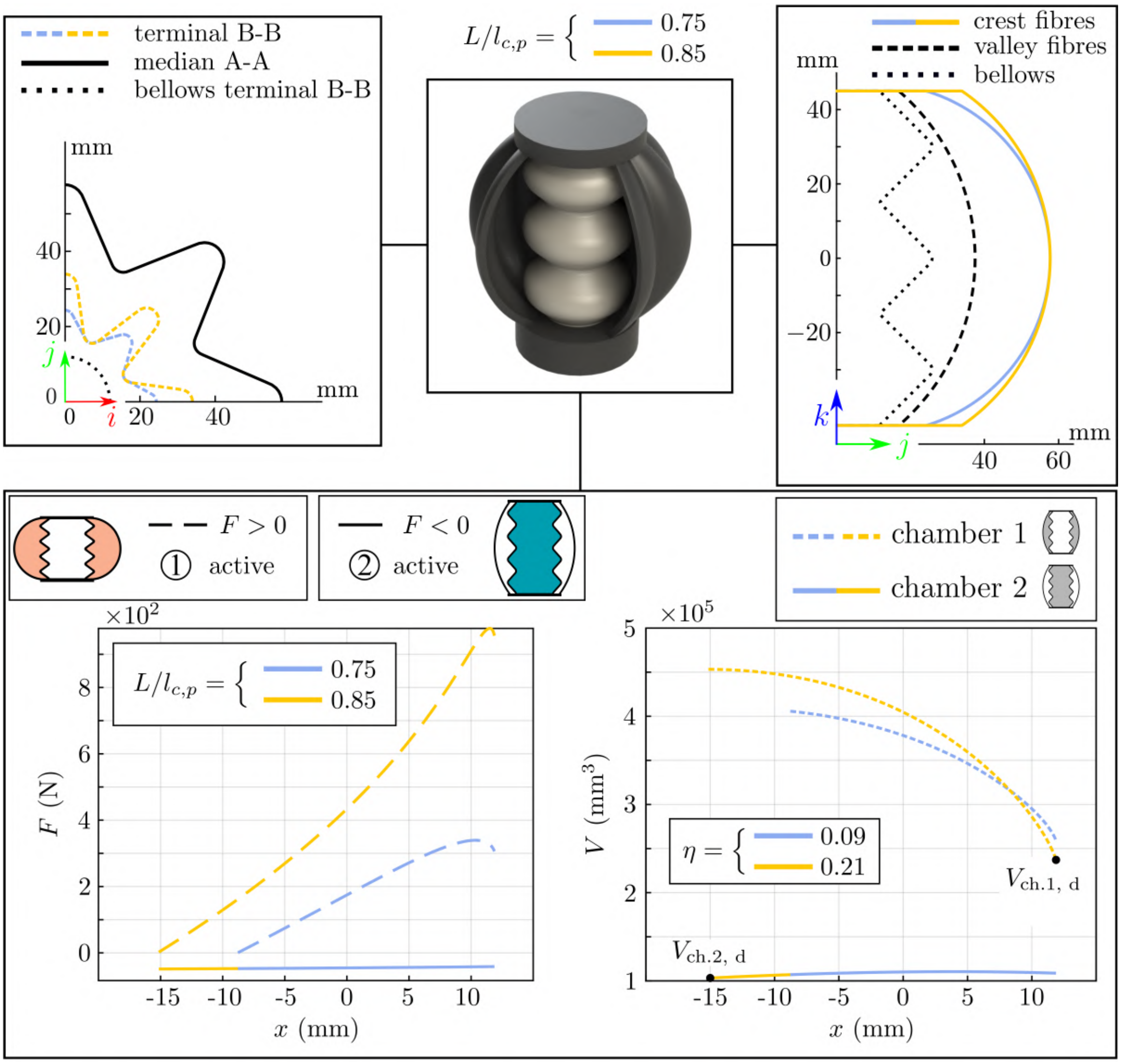

Figure 2.7: Influence of $l_{c,p}$ on the actuator static performance. $L$ =90 mm, $l_{v,p}$ =102 mm, $R_{ie,p}$ =17 mm, $R_{ve,p}$ =1.6 mm, $R_{im,p}/R_{om,p}$ =0.65, $N_p$ =8, $R_{i,b}$ =12 mm, $\alpha_b$ =45 deg, $R_{v,b}$ =0.5 mm, $R_{c,b}$ =2 mm, $N_b$ =3. For the first case $R_{ce,p}$ = 2.3 mm, for the latter $R_{ce,p}$ = 3.3 mm.

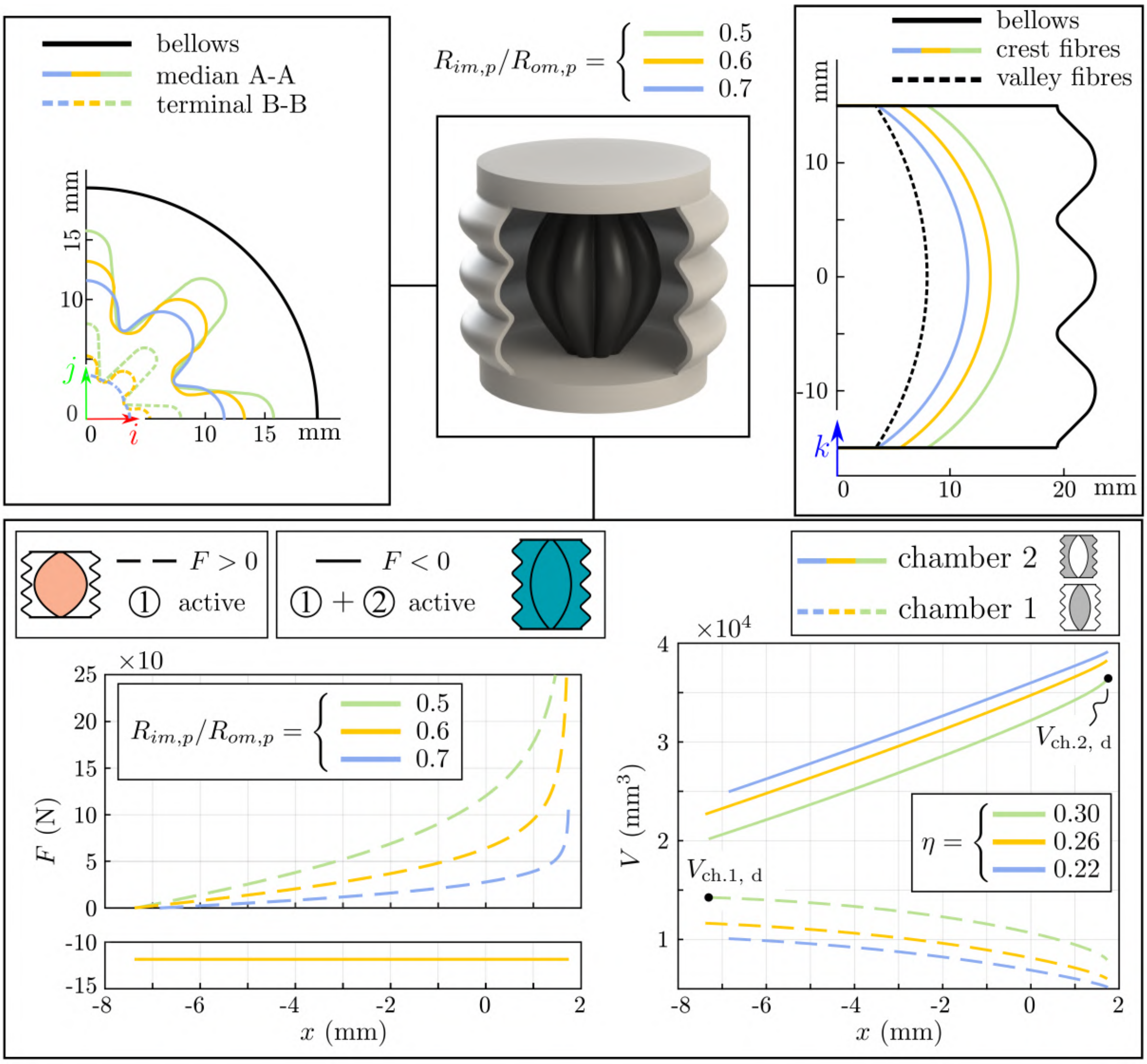

Figure 2.8: Influence of $R_{im,p}/R_{om,p}$ on the actuator static performance for a type B geometry. $L$ =30 mm, $l_{c,p}$ =35.3 mm, $l_{v,p}/l_{c,p}$ =0.9, $R_{ie,p}$ =3.5 mm, $N_p$ =8, $R_{i,b}$ =19 mm, $\alpha_b$ =45 deg, $R_{v,b}$ =1 mm, $R_{c,b}$ =3 mm, $N_b$ =3. For the first two cases $R_{ve,p}$ =0.7 mm and $R_{ce,p}$ =1 mm, for the latter $R_{ve,p}$ =1.4 mm and $R_{ce,p}$ =1.4 mm.

## 2.3 Prototyping and testing

The fundamental elements of the BiSoft.Q actuator are the two membranes and the two rigid end fittings. Both membranes must be airtight and they must withstand the pressure forces acting on them. Furthermore, the pleated membrane must also be able to transmit the pulling force to the end fittings. On other hand, the two end fittings are responsible for three key functions: facilitating airflow into the chambers via designated internal channels, providing a rigid connection between the actuator and the remaining mechanical system, and, in certain instances, closing off the internal volumes at both ends.

A decade ago, the production of PPAMs membranes was typically conducted through injection moulding or the use of coated fabrics. In such cases, the closure of internal volumes by end fittings represented the prevailing approach [128, 138, 146]. When the PPAM was first presented in 1999 [127], it was essentially made of a inextensible fabric, e.g. kevlar or similar, with a thin liner attached on the outside to make the membrane airtight. This membrane was eventually inserted into two end fittings to close the actuator and provide tubing for the actuation. This design was subsequently improved by the same research group to minimize leakages and decrease the PPAM inherent stiffness, by using a more flexible fabric and by transmitting the pulling force by means of inextensible fibres positioned on the valley of each pleat. When presenting the third-generation of PPAMs in 2012, the authors introduced the fused deposition modelling (FDM) technique for the end fitting manufacturing, which allowed the realization of toothed fittings to simplify and make more reliable the pleating operation [138]. The deformable membrane was similar, but the new mounting process ensured a more symmetrical bulging and a better distribution of the pulling force over the single pleat.

However, with the advent of modern additive manufacturing methodologies, it is now possible to fabricate monolithic actuators with sealed internal volumes. For instance, in [139] a monolithic design of a PPAM by using additive manufacturing techniques is presented. The GRACE PPAM designed by the authors has been realized with a variety of materials with a shore hardness ranging from 80A to 98A. The maximum operating gauge pressure for 80A was 30 kPa, while 220 kPa for 98A TPUs. Similar methods have been used in other research papers to manufacture pneumatic actuators such as bellows [140] or actuators with more complex geometry [147, 148, 149].

Although FDM techniques permit the creation of intricate and enclosed geometries, the authors assert that the high power-to-weight ratio of PPAMs necessitates the utilisation of rigid end fittings, as the enhanced rigidity of plastic or metallic materials offers a more robust and reliable mechanical connection.

Figure 2.9 (a) and (b) illustrate two design solutions that reflect the aforementioned considerations. With respect to the option in which rigid plugs are used to close the internal volumes, the connection is achieved through the use of a geometric coupling and clamping ring, while the seal is provided by a silicone sealant. The method of manufacturing the parts individually and subsequently assembling them has two distinct

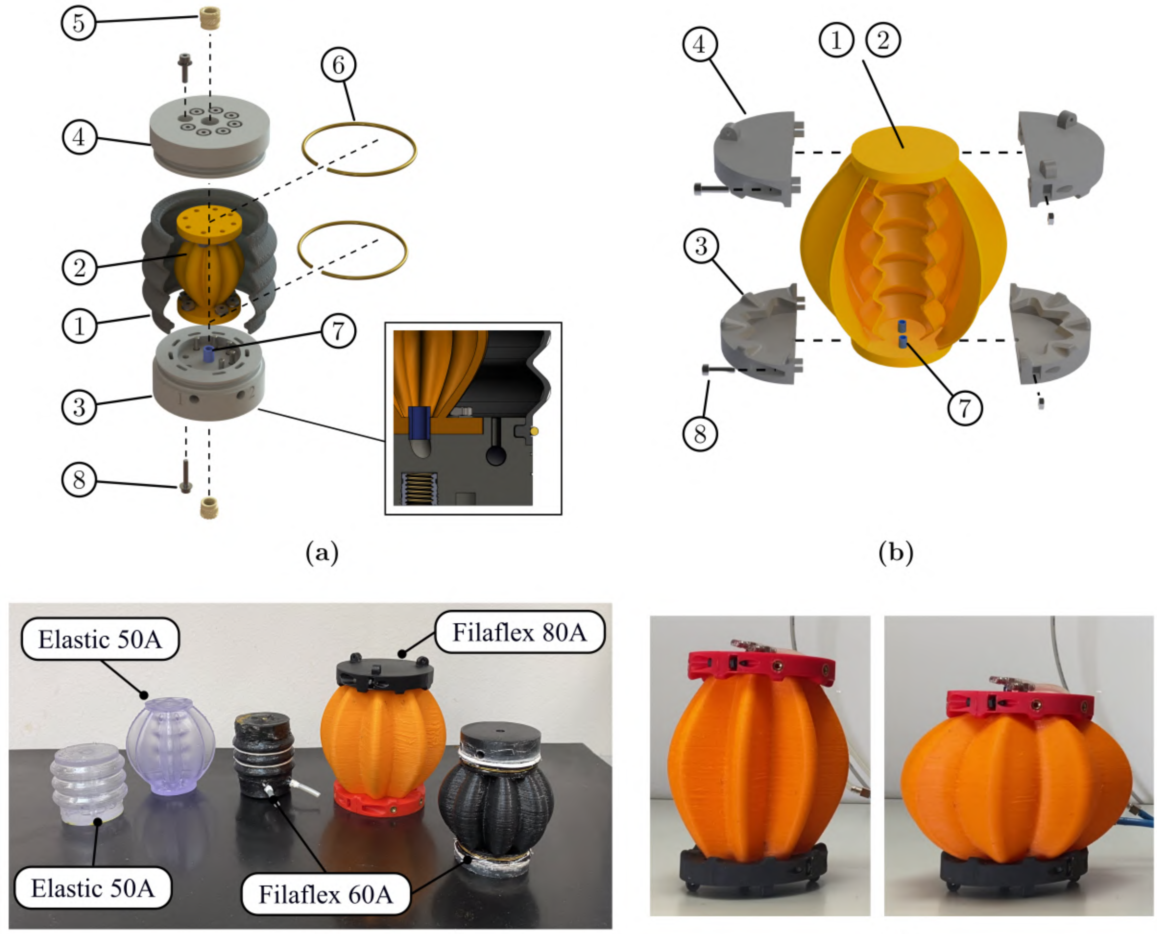

(a) (b) (c) (d)

Figure 2.9: BiSoft.Q executive design. **(a)** Assembly design with end caps to close the membrane internal volumes. The connection to the rest of the mechanical system is achieved through metallic inserts integrated into the plastic end fittings. **(b)** Monolithic design. The mechanical connection is here established through the use of hinge joint. (1) bellows, (2) pleated membrane, (3) lower cap with internal channels, (4) upper cap, (5) metallic insert, (6) clamping ring, (7) polyurethane tubing, (8) socket head cap screw. **(c)** BiSoft.Q prototypes. **(d)** BiSoft.Q type A realized with the assembly design in its maximum and minimum configurations.

advantages. Firstly, it allows for the replacement of parts in case of failure. Secondly, in the case of the BiSoft.Q, it permits the verification of the actual tightness of the inner chamber before assembly. The picture also shows a detail of the assembly, with the fluid inlets made in the lower cap and the bolted connection to secure the inner membrane to the caps. It is worth noting that the design of the internal channels for type A is made more challenging than for type B due to the minimisation of the antagonistic area problem discussed in the previous section. On other hand, the monolithic design in Figure2.9 (b) is a time-saving solution that circumvents the non-trivial issue of fixing between membranes and end fittings, and also reduces the number of components.

Figure 2.9 (c) shows a series of BiSoft.Q prototypes, produced through the utilisation of FDM and SLA (stereolithography) technologies. These prototypes have been constructed through the application of both the assembly and monolithic approach. The deformable membranes were tested with elastic materials having a shore hardness ranging from 60A to 95A, with a bladder thickness ranging from 0.8 mm to 1.4 mm. Polylactic acid (PLA) was used for the rigid caps. The maximum supply pressure was found to be higher than that reported in [139], namely 60 kPa for 60A TPUs and 150 kPa for 80A, despite undergoing a limited number of one hundred testing cycles. The manufacturing method is also a significant factor in the design process. As illustrated in Figure 2.6, an elevated value of $l_{v,p}$ may enhance the actuator's static performance. However, this would also result in elevated values of the $\varphi_{[c,v],p}$ angles, defined in Figures 2.2 and 2.3. In the case of FDM or SLA, the maximum printable overhang angle imposes an upper limit on the value of $\varphi_{c,p}$, which is always the higher of the two, with maximum values of approximately 55 degrees [150], which leads to:

$$\frac{L}{l_{c,p}}_{\min} \approx 0.85 \tag{2.21}$$

Similar limitation are applied on the bellows structure, here constraining the $\alpha_b$ maximum value.

### 2.3.1 Static apply experimental curve

To validate the accuracy of the analytical model employed within the design process, the isometric experimental characterization [83] of a BiSoft.Q type B with a nominal height $L$ =30 mm and an external diameter of $R_{i,b}$ =19 mm has been conducted. The BiSoft.Q specimen has been realized by using the assembly design, and both membranes have been made of TPU 60A extruded by a FDM machine. During the course of the tests, the elongation of the actuator was regulated by means of a manually operated linear slide, while the supply pressure was maintained at a constant level by means of a pressure regulator. To complete the experimental setup, the force exerted by the actuator was measured by a load cell[3]. The discretization step for the linear guide has been equal to 0.2 mm, and the resulting isobar curves have been fitted with a second order polynomial curve (linear least squares method). The results of the experimental tests are shown in Figure 2.10 (b) for a supply pressure from 20 kPa to 60 kPa (gauge). The maximum theoretical stroke of the actuator is equal to 3.3 mm, that means a contraction ratio of 11 % with respect to its nominal height $L$.

---

[3] LCM DCE, full scale 1 kN, linearity ± 5%

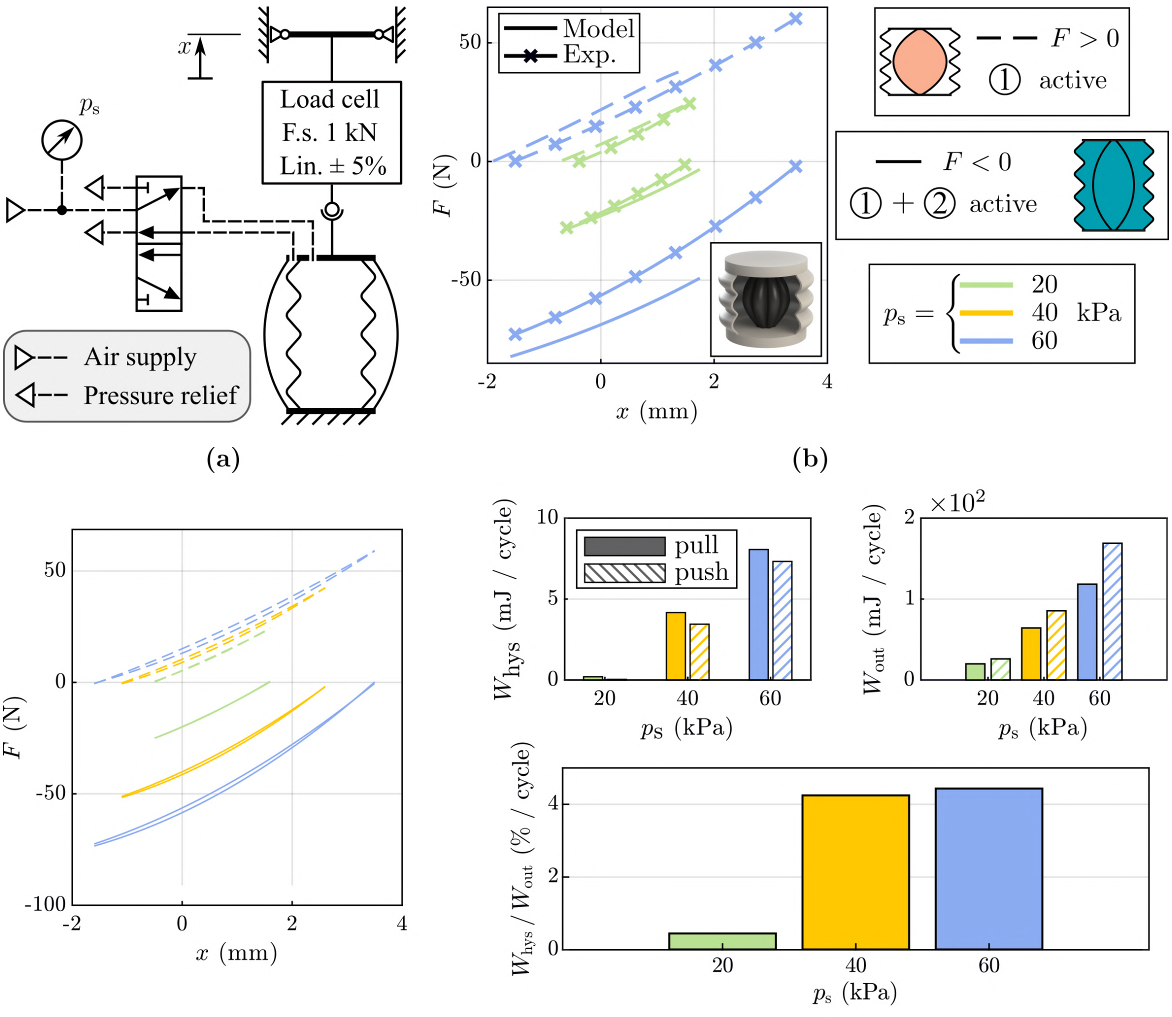

(a)

(b)

(c)

(d)

Figure 2.10: Experimental results for a BiSoft.Q type B actuator. $L = 30$ mm, $l_{c,p} = 35.3$ mm, $l_{v,p}/l_{c,p} = 0.9$, $R_{ie,p} = 3.5$ mm, $R_{ve,p} = 0.7$ mm, $R_{ce,p} = 1$ mm, $R_{im,p}/R_{om,p} = 0.66$, $N_p = 8$, $R_{i,b} = 19$ mm, $\alpha_b = 45$ deg, $R_{v,b} = 1$ mm, $R_{c,b} = 3$ mm, $N_b = 3$. The material used for the membranes is a TPU 60A from Recreus. **(a)** Layout of the experimental setup for the isometric tests. **(b)** Experimental static apply curves and comparison with the analytical model implemented during the design process. **(c)** Hysteresis curve over the single pulling or pushing cycle at different levels of supply pressure. **(d)** Comparison between the output work $\mathscr{W}_{\text{out}}$ done by the actuator and the work $\mathscr{W}_{\text{hys}}$ lost due to dissipative hysteretic phenomena.

Higher levels of supply pressure $p_s$ within chamber 1 of the actuator correspond to higher levels of $|x_{\min}|$, whose aspect is predicted by the model with an error of 0.3 mm on the 60 kPa curve, that is a relative error of 9 % with respect to the maximum theoretical stroke $s$. On other hand, the model looses its accuracy in predicting the value of $x_{\text{max}}$ for pressure levels above 40 kPa. In this case, the pressure force acting on the end plates is such that the longitudinal fibres of the bladder are no longer inextensible, resulting in an additional stroke of the actuator and elastic deformation of the pleated membrane. This behaviour is undesired, and further thickening of the longitudinal fibres of the actuator can only provide a minimal improvement.

In terms of exerted force, the model is more accurate for the pulling force than for the pushing force, with an average error of 4 N in case of pulling behaviour. The authors assumes this is due to having neglected the stiffness of the pleated membrane, that becomes relevant when the actuator approaches the extended configuration.

While not achieving the same degree of precision as FEA techniques, the developed analytical model offers valuable support during the actuator design phase, with a moderate computational cost and accurate estimation of stroke and pull force under nominal behaviour. With regard to pushing forces, the results indicate the need for a method of calculating membrane stiffnesses in the model, particularly that of the pleated geometry.

Figure 2.10 (c) also shows the experimental hysteretic behaviour of the actuator. Once again, the tests were isometric, commencing from the $x_{\text{min}}$ configuration. The $\mathscr{W}_{\text{hys}}$ term represents the work lost due to dissipative phenomena, while the $\mathscr{W}_{\text{out}}$ term represents the work exerted by the actuator, i.e. it is the subtended area of the experimental static apply curves. As shown in Figure 2.10 (d), the hysteretic term measured on the single cycle is completely irrelevant when compared to $\mathscr{W}_{\text{out}}$ in the case of $p_s$ =20 kPa, while it slightly increases to values of 4.5 % in the case of pressures above 40 kPa.

The findings confirm the benefit of PPAM actuators over traditional PAMs, where the elongation of the actuator is achieved through the elastic deformation of the diaphragms under pressure, resulting in a more pronounced hysteretic behaviour [131].

### 2.3.2 Air consumption

In addition to the experimental characteristic of static apply measured through isometric tests, the experimental characterization of the actuator's air consumption during a single actuation cycle is also of interest. In the case of actuator control via a directional valve, as shown in Figure 2.10 (a), the theoretical estimate of this consumption is given by Equation 2.13. This estimate depends on $V_{\text{ch. }[1,2]}(x)$, the calculation of which is described in Appendix A.2 and is carried out using the simplified model described previously.

Figure 2.11 (a) shows the experimental setup used for these tests, which were conducted on a BiSoft.Q type A[4]. The testing procedure involved connecting the reservoir, with a capacity of $V_r = 3.8$ liters, to the pressure source through a check valve. Once the

---

[4] The geometry of the BiSoft.Q is provided in the figure caption.

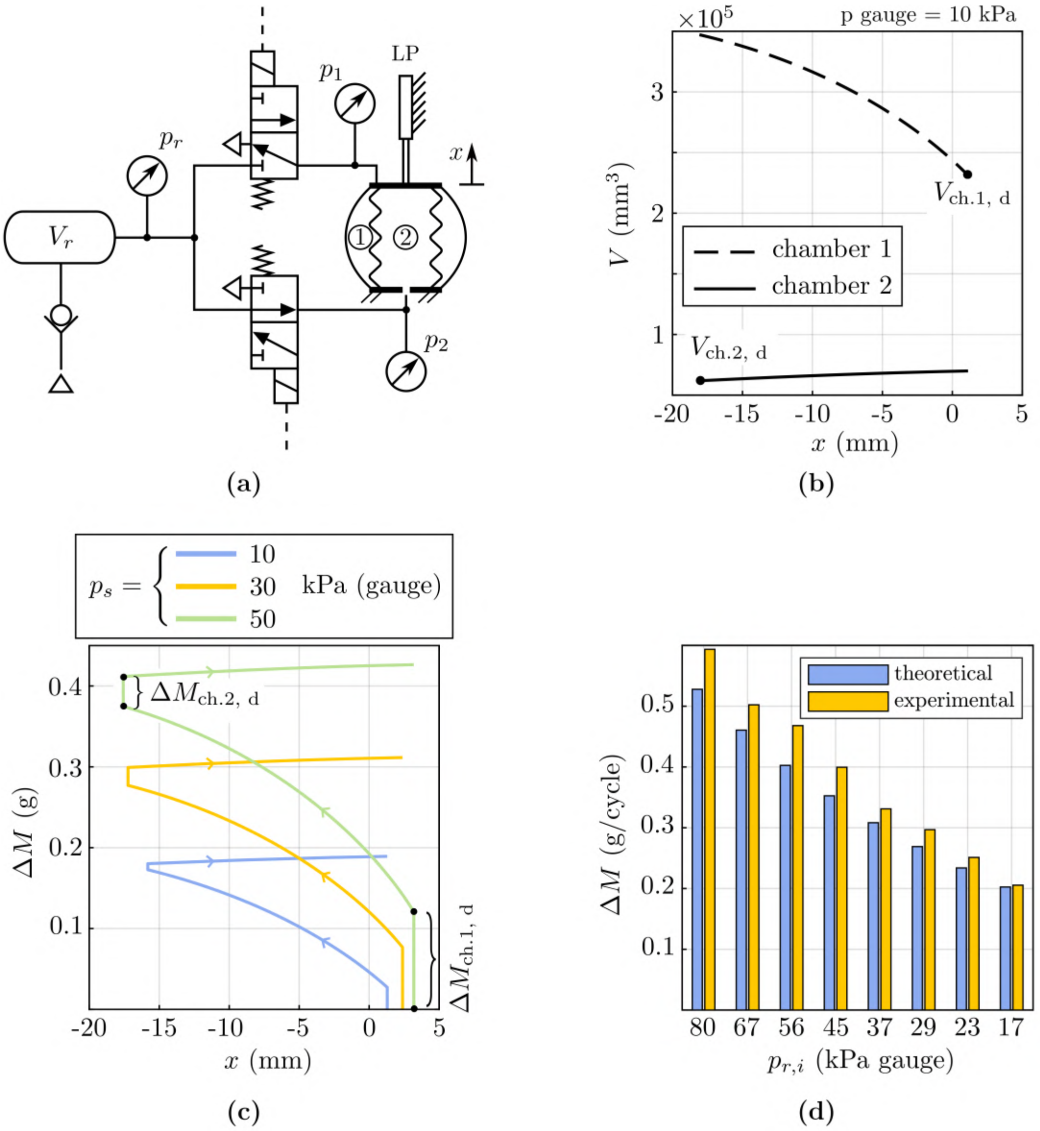

Figure 2.11: Prove sperimentali di consumo di aria di un BiSoft.Q type A. $L$ =90 mm, $l_{c,p}$ =106 mm, $l_{v,p}/l_{c,p}$ =0.9, $R_{ie,p}$ =17 mm, $R_{ve,p}$ =1.6 mm, $R_{ce,p}$ =2.3 mm, $R_{im,p}/R_{om,p}$ =0.65, $N_p$ =8, $R_{i,b}$ =8 mm, $\alpha_b$ =45 deg, $R_{v,b}$ =0.5 mm, $R_{c,b}$ =2 mm, $N_b$ =3. **(a)** Experimental setup. **(b)** Theoretical estimate of the internal volumes within the actuator. **(c)** Estimated air consumption during a single actuation cycle. **(d)** Results expressed as the theoretical versus experimental comparison of the actuator's air consumption.

supply was disconnected, the BiSoft.Q was then controlled using two 3-way 2-position solenoid valves, as described in Figure 2.11 (a). A single actuation cycle begins from the configuration of $x_{\text{max}}$. The bottom end-fitting of the actuator is fixed, while the upper one is free to move.

The elongation of the BiSoft.Q is measured using a linear potentiometer[5], while the pressure in the reservoir and the two chambers of the actuator is measured using pressure transducers[6].

The theoretical estimate of the internal volumes within the actuator is shown in Figure 2.11 (b), for a supply pressure of 10kPa (gauge). Figure 2.11 (c) instead shows the estimated air consumption during a single actuation cycle at different supply pressures $p_s$. For this geometry, the pressurization of chamber 1 is the main contributor to energy consumption, both due to the greater volumetric variation and the larger dead volume.

Figure 2.11 (d) shows the theoretical versus experimental comparison of the actuator's air consumption. Since the pressure source is disconnected from the system during the tests, each switch of the actuator corresponds to a decrease in the pressure of the reservoir $p_r$, which is therefore not constant. The graphs in Figures 2.11 (b) and (c) are recalculated for each cycle.

The theoretical model consistently underestimates the actual consumption, though it maintains good accuracy, with an average difference of approximately 8%. Additionally, the estimation error decreases as the pressure in the reservoir $p_r$ drops.

### 2.3.3 Energy saving strategies

Although not thoroughly investigated through experimental tests, there is an indication of energy-saving methods during the functioning of the SPA. As the experimental findings demonstrate, the actuator's air consumption is significantly influenced by the dead volumes in the two chambers. These volumes augment the amount of air mass spent in each actuation cycle to drive the actuator, without altering its output performance. Consequently, the objective should be to minimise these volumes or, if technically feasible, to eliminate them entirely.

In addition, when the BiSoft.Q is controlled by means of a 5-way 2-position spool valve, the pressurised air sent into the active chamber is ejected through the exhaust when the valve is switched. To address these issues, the literature proposes several energy-saving strategies based on two principles:

- Recovery of pressurised air by recirculation between the two chambers (internal recirculation) or by means of an auxiliary reservoir (external recirculation) [143];
- Partial filling of the chambers with liquid or granular material to reduce dead volumes [52].

Figure 2.12 shows, for instance, the IEAR (Internal Exhaust Air Recirculation) strategy, which in fact adds the 2-way 2-position valve $D_2$ to allow, when switching from $x_{\max}$

---

[5] Opkon SLPT 75 D 5K 1M, full scale 75mm, linearity ±0.05%.

[6] Honeywell ABP2DANT030PGAA3XX, full scale 207kPa, accuracy ±0.25%.

to $x_{\min}$, the recirculation of air between the two chambers. Equation 2.12 and Equation 2.13 for calculating the air consumption over a single operating cycle are therefore slightly modified with the introduction of the intermediate configuration $x^*$ and its analogue $x^{**}$. The latter one, which is not shown for the sake of simplicity, is obtained with internal air recirculation when the SPA is to be switched from $x_{\min}$ to $x_{\max}$. The

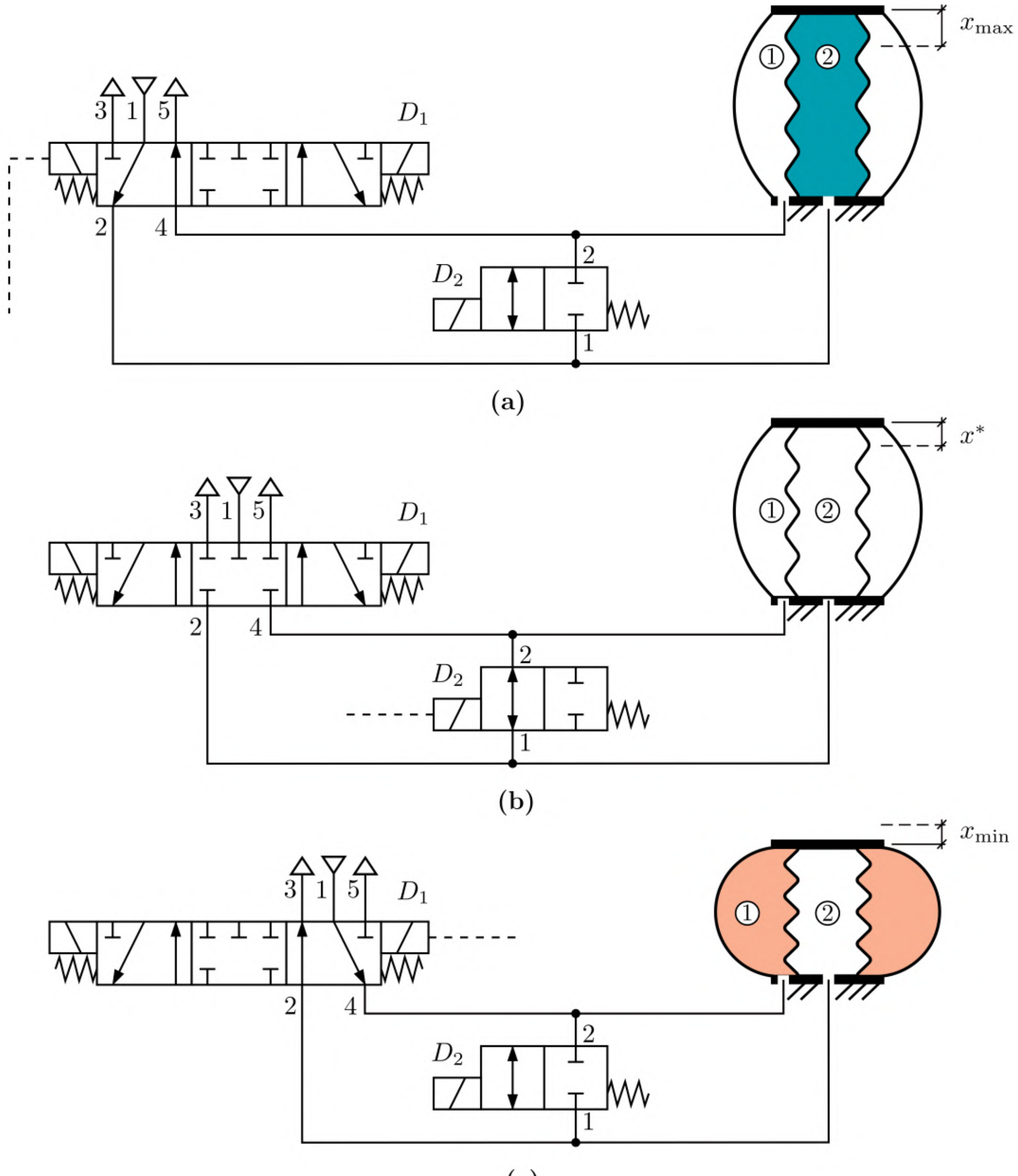

(a)

(b)

(c)

Figure 2.12: Schematic of the IEAR (Internal Exhaust Air Recirculation) system for recovering pressurized air from the active chamber. **(a)** $x = x_{\max}$, $D_2$ closed. **(b)** $x = x^*$, $D_2$ open. **(c)** $x = x_{\min}$, $D_2$ closed. The coloured chamber denotes the active one.

configuration $x^*$, and similarly $x^{**}$, can be straightforwardly obtained by imposing the following conditions:

$$F(x) = \left( \frac{N_p\, p^*}{2\, \tan(\varphi_{c,p}(x^*))} \int_\Sigma \hat{n}_1\, d\Sigma \right) - p^* \left( A_a + \pi\, R_{i,b}^2 \right) - F_{\text{elastic, b}}(x^*) = 0 \tag{2.22}$$

$$\frac{P_s V_{\text{ch. 2}}(x_{\text{max}}) + P_{\text{amb}} V_{\text{ch. 1}}(x_{\text{max}})}{R T_{\text{amb}}} = \frac{P^*(V_{\text{ch. 1}}(x^*) + V_{\text{ch. 2}}(x^*))}{R T^*} \tag{2.23}$$

where the former imposes that $x^*$ is the static equilibrium configuration under free-load condition, and the latter imposes the conservation of the mass of air present in the two chambers. $P^*$ and $T^*$ result to be the internal pressure and temperature of the air in this intermediate configuration (let assume, for simplicity $T^* = T_{textrmamb}$). Note also how it is necessary to add, to the antagonist area, the internal area of the bellows. From configuration $x^*$, the BiSoft.Q finally reaches configuration $x_{\text{min}}$. The air consumption $\Delta M_{\text{ch. 1}}$ is therefore equal to:

$$\Delta M_{\text{ch. 1}}^{\text{IEAR}} = \frac{P_s\, V_{\text{ch. 1}}(x_{\text{min}}) - P^*\, V_{\text{ch. 1}}(x^*)}{R\, T_{\text{amb}}} \tag{2.24}$$

and in a similar manner:

$$\Delta M_{\text{ch. 2}}^{\text{IEAR}} = \frac{P_s\, V_{\text{ch. 2}}(x_{\text{max}}) - P^{**}\, V_{\text{ch. 2}}(x^{**})}{R\, T_{\text{amb}}} \tag{2.25}$$

The IEAR strategy proves to be a simple solution (requiring only one additional valve) but effective in saving energy. Since recirculation occurs until the pressure in the two chambers balances, however, it is evident that there is a physical limit to the energy recovery possible by following this technique. A further improvement can be achieved by means of EEAR (External Exhaust Air Recirculation) [143, 142, 141], which is not further explored in this thesis.

Regarding the aforementioned strategy of partial filling of the actuator with fluid or granular media, it may be performed in order to decrease the dead volumes of the actuator. Figure 2.13 shows a schematic where two liquid-air interface volumes ensure that only the air actually required to drive the BiSoft.Q Type A is sent. In that instance, Equation 2.13 is adjusted by removing the terms $V_{\text{ch. 1, d}}$ and $V_{\text{ch. 2, d}}$:

$$\Delta M^{\text{Fill}} = \frac{P_s(\Delta V_{\text{ch. 1}} + \Delta V_{\text{ch. 2}})}{R\, T_{\text{amb}}} \tag{2.26}$$

The graph in Figure 2.14 quantifies the energy savings achievable through the methods described. In a similar manner to what has been described in previous subsections, air consumption is calculated over a single actuation cycle starting at $x_{\text{max}}$. With a supply pressure of $p_s = 100$ kPa, dead-volume filling turns out to be the more efficient of the

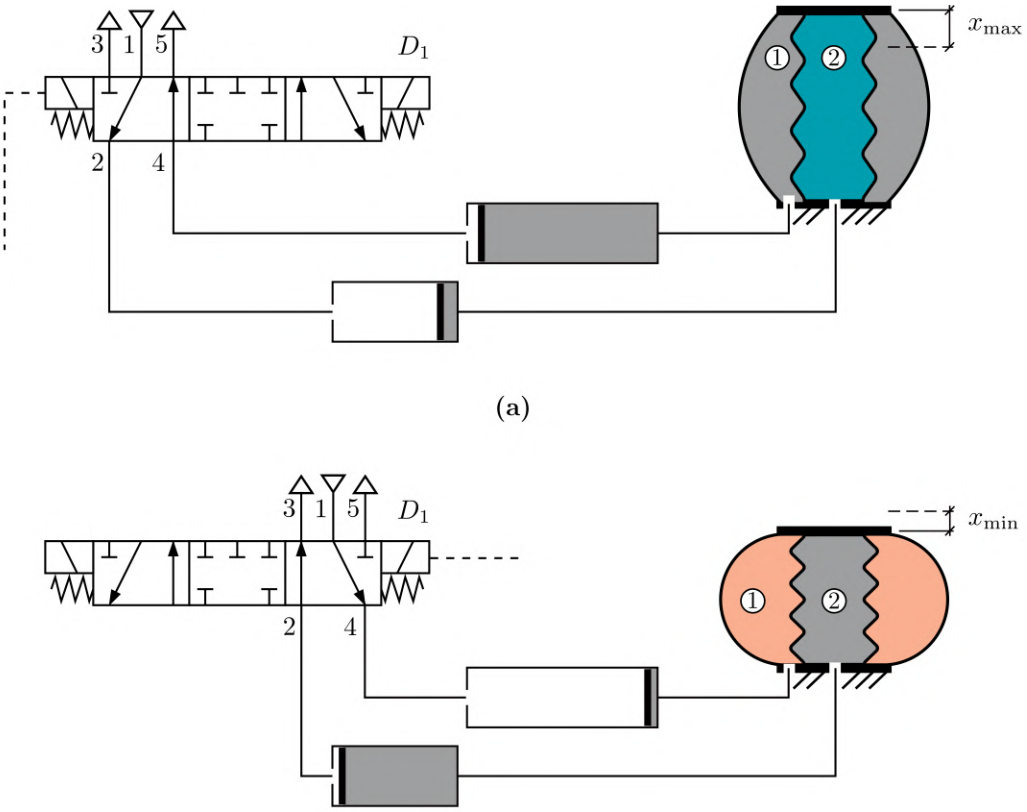

**(a)**

**(b)**

Figure 2.13: Schematic of a BiSoft.Q Type A actuator filled with incompressible fluid or granular media to minimize the actuator dead volumes. The coloured chamber is the active one. The interface chambers are schematized as rodless cylinders. **(a)** Extension, **(b)** contraction.

two methods, with a reduction in air consumption of 46%. Internal recirculation, on the other hand, allows a reduction of 22%. The figure also shows the combined effect of filling and IEAR carried out, in this case, between the two auxiliary cylinders. However, it does not have a significant effect compared to the mere filling of the chambers, with a reduction in air consumption of 48%.

## 2.4 Application of BiSoft.Q in Service Robotics

It has been proposed that PAMs, and in particular PPAMs, can be employed as a technological solution for the implementation of revolute joints, hopping mechanisms and robotic grippers due to their inherent compliance and high force to weight ratio. In the case of the latter application, for instance, the inherent compliance of these devices

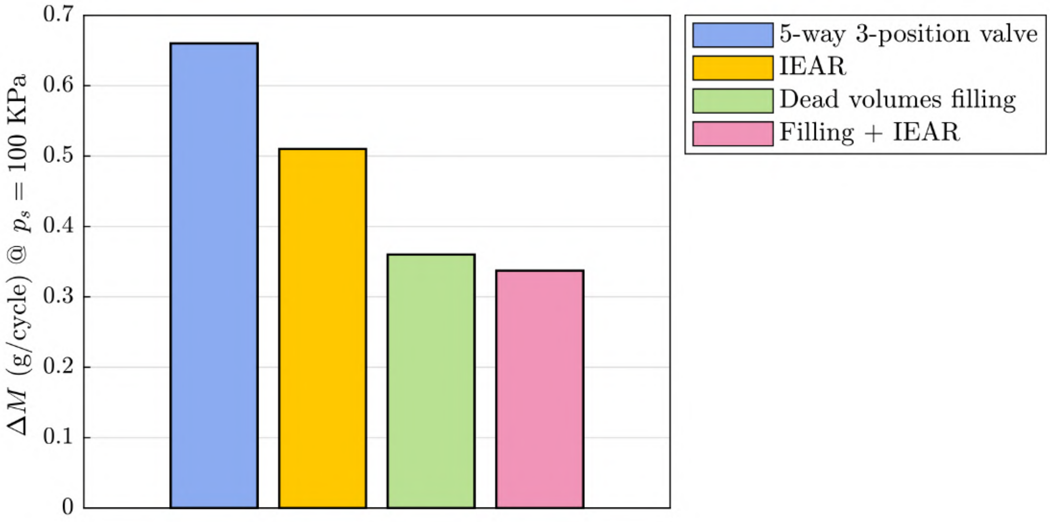

Figure 2.14: Theoretical comparison of air consumption for a BiSoft.Q Type A during an actuation cycle starting from $x_{\max}$. The geometric specifications of the BiSoft.Q are the same as those in Figure 2.11.

makes them safer, enabling them to adapt to the shape of a gripped object and preventing damage.

Nevertheless, prior to considering the potential applications of the BiSoft.Q, a fundamental question concerns the actual difference in performance between the two types, and, more generally, their advantage over the simple alternative of placing a traditional PPAM in parallel with a bellows actuator. Figure 2.15 presents a comparison of the static force versus stroke graph, derived from the design model of section 2.2, for the three cited solutions. The total encumbrance, i.e. the nominal longitudinal length and radial dimension, is kept fixed for all the three cases. The supply pressure considered is $p_s$ =100 kPa (gauge).

This analysis shows that by using a BiSoft.Q type A, higher pull forces can be achieved at the expense of lower push forces than any other solution. Type A has the highest stroke $s$, with an strain ratio of $s/L$ =24 %. Type B, on the other hand, has shorter strokes since the longitudinal fibres of the pleated membrane are smaller than those of type A, but the forces that can be achieved when pushing or pulling are much more balanced.

Finally, the graph shows the real advantage of the BiSoft.Q over the parallel solution. Although the design is simpler, the strokes are similar to those of type B and the forces obtained are always lower than in the other two cases. However, in the case of the BiSoft.Q, the pulling forces are not as much related to the size of the end plates, but rather to the surfaces of the folded bladder and the inclination angle $\varphi_{c,p}$, as reported

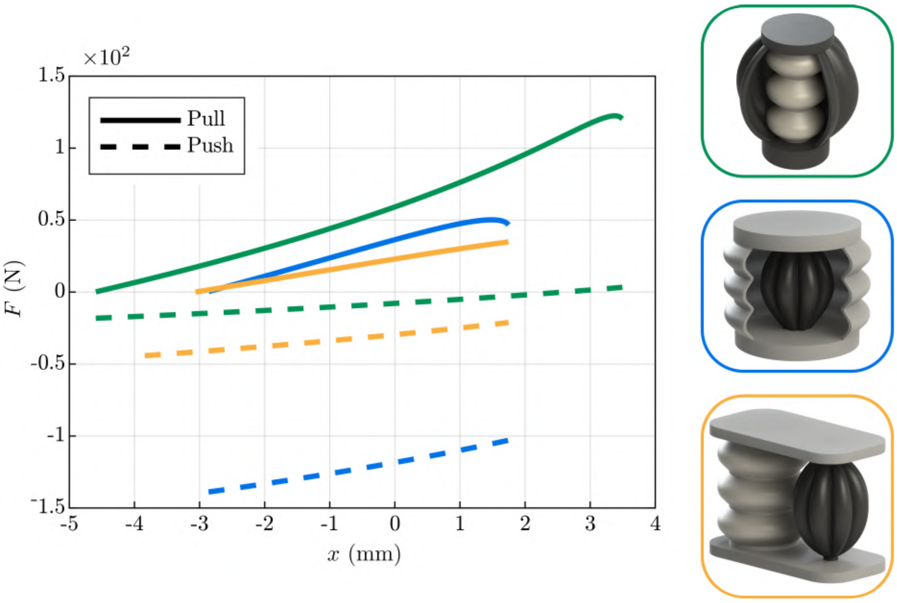

Figure 2.15: Comparison of the two types of BiSoft.Q and the trivial parallel case on the static apply graph. The comparison is made for the same longitudinal nominal length and radial encumbrance.

in Equation 2.9.

It can thus be concluded that both types of BiSoft.Q exhibit advantages in the static apply graph over the basic parallel solution. The selection between the two types, however, is dependent on the specific requirements of the intended application.

### 2.4.1 Actuator comparison

Table 2.2 compares the two types of BiSoft.Q with other one-directional linear PPAMs and bidirectional linear PAMs in the literature. The indices used in the comparison are those reported in the review paper by Mirvakili and Hunter [129] and were used by Villegas et al. to compare the third generation PPAM with the PAM produced by Festo [138]. With regard to the method of membrane reinforcement, the third generation of PPAM used highly stiff longitudinal fibres, such as Dyneema fibres, which ensured that maximum supply pressures of 400 kPa and elongations of about 38 % could be achieved. The slenderness ratio, i.e. the ratio of the length to the radius of the actuator, is approximately 10. This generation of PAMs also included the use of FDM for the end fittings, allowing a reduced total weight of 60 g, similar to that of the BiSoft.Q. Due to the higher internal pressures and maximum tensile forces of around 6000 N, the PPAM has an energy work density that is an order of magnitude higher than that of the BiSoft.Q. This is defined as the ratio between the output work on the cycle and the volume (or mass) of the actuator.

Table 2.2: Comparison of BiSoft.Q with bi-directional PAMs and mono-directional PPAMs available in the scientific literature.

| | **PPAM** [138] | **GRACE-A** [139] | **MMKM** [35] | **BiFAc3** [128] | **BiSoft.Q A**(1) | **BiSoft.Q B**(2) |
|---|---|---|---|---|---|---|
| **Membrane reinforcement** | Netting | None<br>(3D printed) | Braiding | Reinforced rubber | None (3D printed)(3) | |
| **Supply pressure $p_s$ (kPa gauge)**(4) | 400 | 220 (-83) | 100 | 75 | 100 | 100 |
| **Mass (g)** | 60 | n/a | | | 63 | 60 |
| **Strain (%)** | 38 | 31 | 49 | 19.1 | 24 | 15 |
| **Engineering stress (MPa)** | 159 (5) | 0.05 (0.06) (5) | 2.9 (1.9) (5) | n/a | 1.05 (0.4) | 0.5 (0.8) |
| **Energy work density (kJ m$^{-3}$)** | 287 | n/a | | | 23 | 16 |
| **Energy work density (J kg$^{-1}$)** | 72 - 1112(6) | n/a | | | 7 | 11 |
| **Efficiency (%)** | n/a | | | | 22.47 | 14.8 |
| **Deformation under pressure** | Contraction | | Bi-directional | | | |

(1) $L$ =30 mm, $l_{c,p}$ =35 mm, $l_{v,p}/l_{c,p}$ =0.95, $R_{ie,p}$ =7 mm, $R_{ve,p}$ =0.44 mm, $R_{ce,p}$ =2.2 mm, $R_{im,p}/R_{om,p}$ =0.80, $N_p$ =8, $R_{i,b}$ =5 mm, $\alpha_b$ =45 deg, $R_{v,b}$ =1 mm, $R_{c,b}$ =3 mm, $N_b$ =3.

(2) The actuator parameters are the same as in Figure 2.10.

(3) Some BiSoft.Q prototypes present a cotton reinforcement wire for the outer membrane

(4) For bi-directional actuators, values in brackets refer to the push mode in case they differ from the pull mode. The same applies to the subsequent lines.

(5) Extrapolated by the author of this thesis. The engineering stress is defined as the ratio between the maximum output force and the actuator cross-sectional area.

(6) Depending on the PPAM length.

In terms of engineering stress, it is instead calculated as the ratio of the maximum output force to the cross-sectional area of the actuator when not pressurized, and gives an indication of the stress state to which the diaphragm is subjected. The design differences between the different actuators can be seen in this index, with the value for the PPAM being two orders of magnitude higher than for the GRACE-A and BiSoft.Q. This is due to both the higher forces of the PPAM and its smaller cross-sectional area. The Multifunctional Mc-Kibben Muscle, referred to as MMKM in the table, by Hassan et al. [35], also exhibits a higher engineering stress than the two PAMs produced by additive manufacturing techniques, namely GRACE and BiSoft.Q. This is mainly due to the extremely low thickness of the latex membrane of about 0.25 mm, compared to a thickness of about 1 mm for the two actuators mentioned above.

In the field of bi-directional actuators, i.e. actuators capable of deforming in both directions when pressurised, the MMKM is the one with the highest strain rate, although its structure requires the braiding angle to be changed before the actuator is pressurised. As it is based on the Mc-Kibben muscle, it will also be characterised by greater hysteretic phenomena than the PPAM [131], although there is no indication of the efficiency or energy dissipation of the actuator.

### 2.4.2 The BiSoft.Q gripper

As mentioned above, one of the possible applications of PPAMs concerns the development of pneumatic gripping systems. In addition to the aforementioned advantages of a PAM, the use of the bi-directional BiSoft.Q in such contexts makes it possible to generate both closing forces, to grasp objects from their external surface, and opening forces, in order to pick up the object from holes or slots or, more generally, from internal surfaces.

Figure 2.16 shows a schematic drawing of a robotic gripper consisting of a six-bar linkage actuated by BiSoft.Q type A. The palm of the gripper, i.e. the $C'C$ link, is fixed to the wrist of the manipulator and is shown fixed in the figure. The elongation of the BiSoft.Q is converted into the translation of $EE'$ and therefore into the closing of the two fingers $CD$ and $C'D'$.

To improve the compliance of the gripper, it is then possible to use flexible fingers, such as the Fin Ray fingers [151, 152], made of the same material as the BiSoft.Q membranes. Based on the results in Figure 2.15, the choice between the two types was made in case A due to its longer stroke compared to type B. However, it is not excluded that a BiSoft.Q gripper based on type B could be developed, in order to exploit its better balance between push and pull forces. Similar layout to that showed in Figure 2.16 can be found in the literature under the name of single-motor grippers, usually driven by an electric motor, as in the case of the three-finger compliant gripper proposed by Liu et al. [153] or the universal soft gripper of Shin et al. [151]. The kinematic chain of these solutions has only one degree of freedom, i.e. the rotation of link fixed to the fingers is

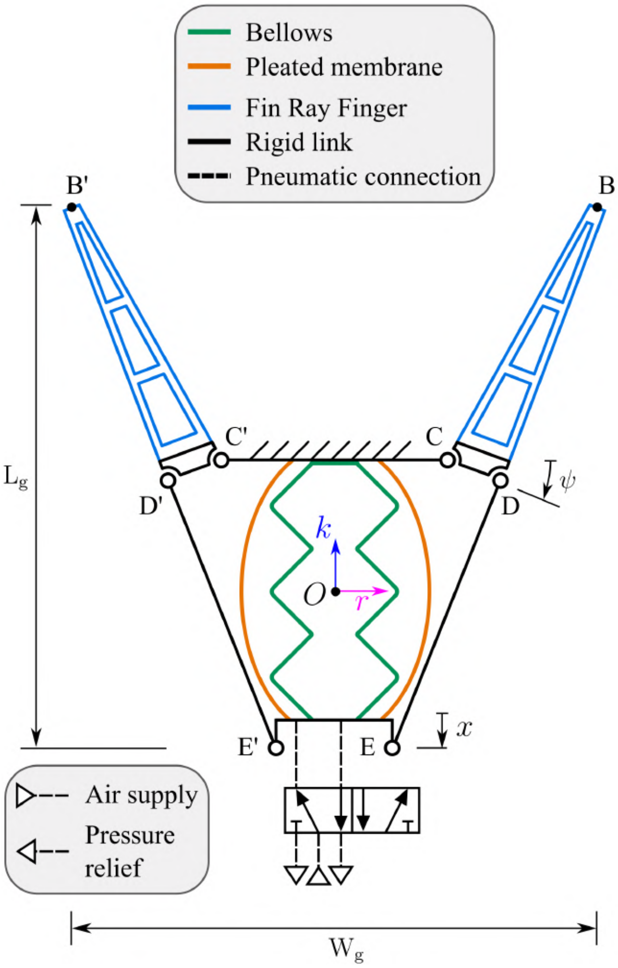

Figure 2.16: Schematic drawing of the BiSoft.Q gripper in a generic configuration. The under-actuated six bar linkage is driven by a BiSoft.Q type A. The two compliant Fin Ray fingers are fixed to the two links CD and C'D'. Link $CC'$ is fixed to the robot wrist, here represented as fixed. The actuator is controlled by a 5-way 2-position spool valve.

uniquely determined by the angle of rotation of the motor, and the mechanical compliance is left to the flexible fingers alone. In contrast, the six-bar linkage that transmits the movement to the fingers makes the BiSoft.Q gripper an under-actuated system. As shown in Figure 2.17 (a), the high stiffness of the actuator in respect of the relative rotations of the two end fittings causes the gripper to close (or open) symmetrically when the forces on the two fingers are equal. However, if the contact forces between the two fingers are unequal, the rotation of the end fitting $EE'$ causes a redistribution of the gripping forces, allowing the gripper to close without damaging the gripped object, as in Figure 2.17 (b). This type of adaptive gripping is therefore similar to that of single motor grippers that integrate differential mechanisms into the transmission, such as the underactuated modular finger by Kakogawa et al. [154] or the single-motor gripper

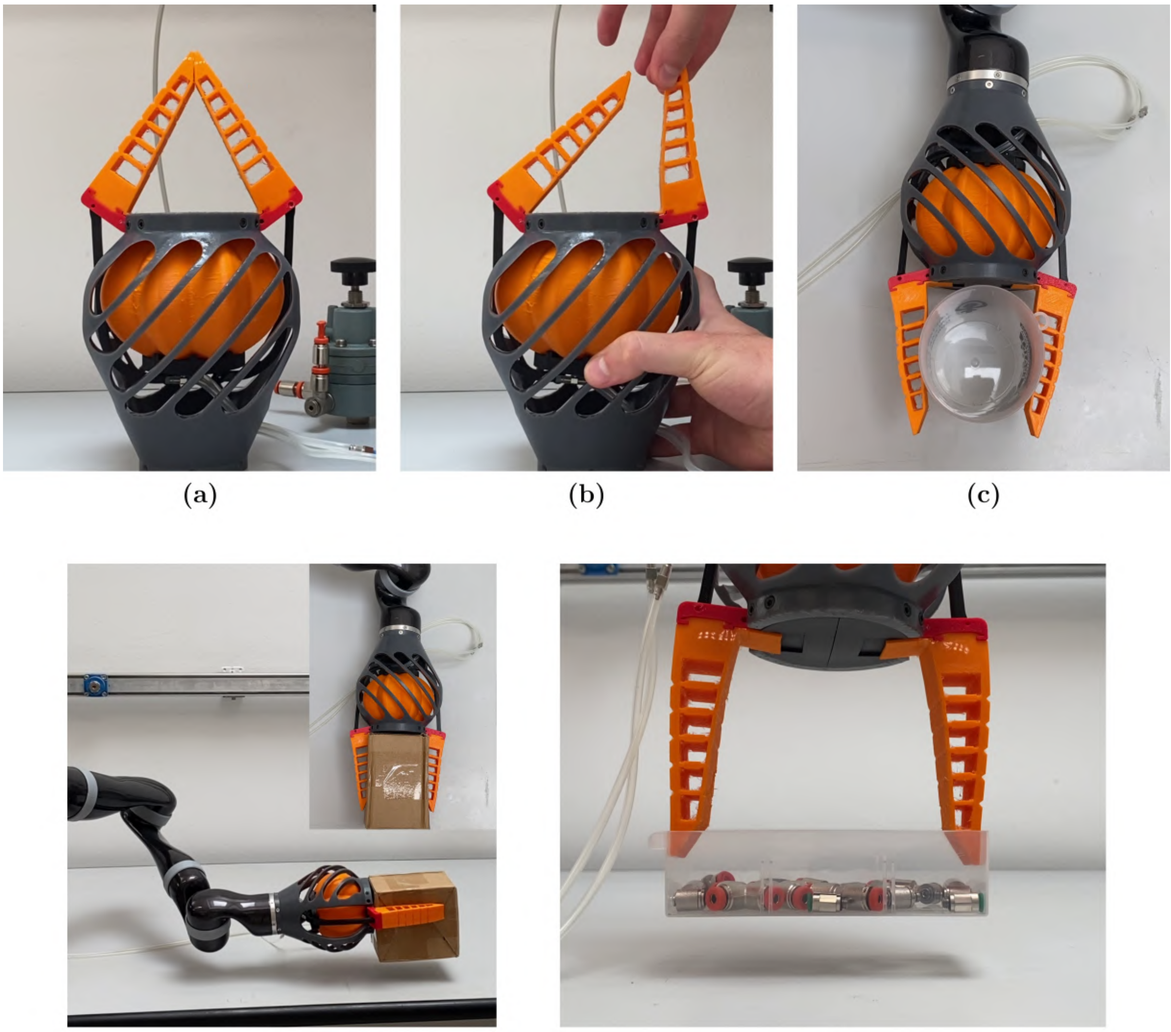

(a) (b) (c)

(d) (e)

Figure 2.17: The BiSoft.Q Gripper type A prototype. The deformable membranes, as well as the Fin Ray compliant fingers, were made in FDM with TPU 82A. The rigid parts are made of tough 2000 resin by Formlabs. The actuator geometric parameters are the same as those in Figure 2.11. **(a)** Gripper closed, **(b)** asymmetric closure due to uneven forces between the two fingers. **(c)** Grasping of a cylindrical plastic cup, diameter 80 mm. **(d)** Grasping of a cardboard box, length of the grasped side 85 mm, mass 600 g. **(e)** Grasping of a plastic box from the inner surface, length of the grasped side 130 mm, mass 200 g.

by Liu et al. [155].

Figures 2.17 (c)-(e) show the behaviour of the BiSoft.Q gripper when grasping objects of different geometries. The gripper was adapted to the Kinova Gen2 manipulator, effectively replacing the company's standard gripper. The design requirements were to

Figure 2.18: The BiSoft.Q Gripper compared to the Kinova KG2.

maintain the same radial encumbrance as the Kinova gripper, as showed in Figure 2.18.

In order to carry out the tests, the compressed air supply and control system was located at the base of the manipulator.

The absence of electric motors, the simplicity of the mechanical drive system and the low mass of the BiSoft.Q allowed a significant reduction in the overall mass of the gripper, which was approximately 250 g compared to 560 g for the Kinova KG2 gripper.

Table 2.3 reports the key data of the BiSoft.Q gripper type A, while Figure 2.19 (a) and (b) shows the estimated contact force on the single finger as a function of the actuator stroke. For this purpose, it is assumed that the grasp is symmetric on both fingers, i.e. that the link $EE'$ translates solely along $\hat{k}$. It is also assumed that the finger is rigid and that the contact force acts both perpendicular to the finger and at the midpoint between $C$ and $B$, as depicted in the figure itself.

With respect to the gripping forces explicable by the Kinova gripper system [156] and ranging from 30 to 60 N over the gripper's range of motion, the BiSoft.Q gripper exhibits similar closing forces when $\psi_{\min}$ and more than twice as high in the $\psi_{\max}$ configuration. However, the opening forces are much lower. Although increasing the supply pressure could easily improve this situation, the value shown in the table of $p_s$ =80 kPa (gauge) represents the maximum currently achievable without actuator failure or malfunction.

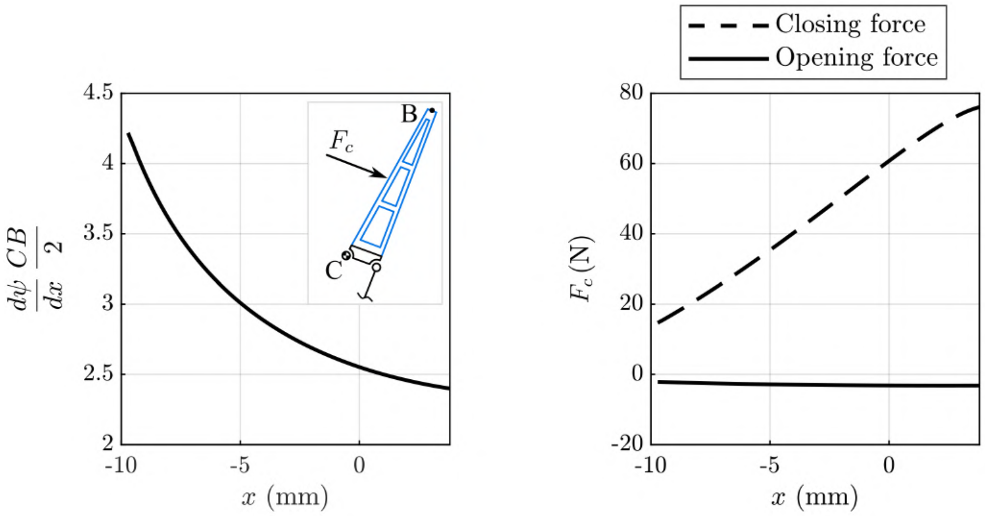

**(a)** **(b)**

Figure 2.19: BiSoft.Q gripper performance in quasi static conditions at a supply pressure $p_s = 80$ kPa (gauge). The finger is assumed as rigid, and $EE'$ can only translate along $\hat{k}$. **(a)** Transmission ratio. **(b)** Estimated contact force on the single finger.

Table 2.3: BiSoft.Q gripper technical data.

| Name | Value |
|---:|:---:|
| Mass (g) | 250 |
| $L_g$ (mm) | 250 |
| $W_g$ (mm) | 180 |
| $CC'$, $EE'$ (mm) | 80, 30 |
| $CB$, $CD$, $ED$ (mm) | 102, 20, 111 |
| $[\psi_{\min}, \psi_{\max}]$ (deg) (1) | [-15, 34] |
| Full opening time (s) (2) | 1,2 |
| Full closing time (s) (2) | 0,8 |

(1) Referring to Figure 2.16, the maximum value corresponds to the fully extended BiSoft.Q configuration and the minimum value corresponds to the maximum contracted one.

(2) These values are inherently dependent on the control circuitry in use, and thus should be regarded as mere indications.

# Chapter 3

# Soft Pneumatic Chambers for Tactile Sensing and Haptic Systems

For contexts of robotic manipulation or human-machine interface (HMI), pressurised chambers made of soft material can be employed as an interface element between the grasped object (or the human being) and the rigid gripper (or the rigid device). In the scientific literature, these kinds of membranes have been termed Soft Pneumatic Sensing Chambers (SPSCs) by Tawk et al. [157]. They are low-cost membranes, designed by the authors to be mostly realised by FDM in TPU.

The functions of SPSCs are plural. In the case, for instance, of robotic manipulation, the interposition of a compliant element between the gripper and the grasped object considerably simplifies the grasping control, which changes from a force control to a position control [158]. It is worth pointing out that, by mentioning mechanical compliance, it generally refers to a spring-damper element, whose elastic part constitutes only the static characteristics [159]. There are, indeed, examples in the literature of soft fingertips whose damping (as well as stiffness) can be actively controlled. In such works, however, the gripping dynamics are relatively fast, thus there is a need to mitigate the severity of the contact transition and to dissipate energy [160, 161]. In recent studies related to Service Robotics, though, the damping part is neglected, due to the gripping dynamics being different from those analysed in industrial robotics contexts. In such studies, therefore, the use of the term *compliant* is reduced to describing only the stiffness of the interface element.

Among the most recent examples in the field of robotic manipulation, Hughes et al. [162] have sensorized a soft gripper using latex-made SPSCs. Kuppuswamy et al. [163] employed the same material to create *soft-bubble* fingertips to be mounted on rigid manipulators, whereby the monitoring of the internal pattern of the SPSC during gripping is used for in-hand pose estimation and object classification. Another camera-based sensing unit has been proposed by Su et al. [164], who sensorised a silicon-made PneuNet gripper using a soft inflatable palm with internal markers. Lastly, Wang et al. [165] developed a rigid-soft gripper where two (or more) soft inflatable bladders are mounted on a rigid cylindrical structure.

In the field of haptic devices, on other hand, the use of SPSCs allows for a compliant interface that enables bi-directional (input/output) communication with the user. To this aim, Tawk et al. [157] have employed different types of SPSCs for rehabilitation, remote control or generic virtual reality (VR) purposes.

Despite the efforts of researchers in this field, limitations still exist. SPSCs have an essentially spherical geometry, except in cases where the membrane is flat (rectangular or circular) and is deformed as a result of pressurisation. Furthermore, there is an absence of parametric analysis regarding the effect of geometry on the stiffness and sensitivity of the sensing unit. In addition to the requirement for a variable stiffness interface, there are strict demands for lightness, compactness and ease of integration of the system. For instance, in the context of robotic grasping, such solutions are designed to be mounted on the end-effector of the manipulator. This necessitates a compact sensing system that does not compromise the payload and workspace of the manipulator, while also enhancing its sensing capabilities. These requirements are equally applicable to haptic systems, where they are essential for improving both the user experience and the transportability of the device. However, it should be noted that compactness and complete functionality for haptic devices are inherently incompatible. Active stiffness control, for instance, necessitates the incorporation of one or more power units (e.g. actuators or compressors), which in turn increases the complexity and weight of the device. Consequently, the aforementioned works are invariably tethered systems, characterised by a cable drift, i.e. an electrical and/or pneumatic cable, towards a delocalised unit.

This chapter discusses the development of a semi-active soft sensing unit, based on pneumatic technology, with variable stiffness. The *semi-active* terminology here refers to an interface whose stiffness can be discretely (but non continuously) adjusted.

The system's interface unit consists of a SPSC connected to a hydro-pneumatic or pneumatic circuit, capable of adjusting its stiffness and estimate the squeezing level of the SPSC. The reduced number of pneumatic components also results in low energy consumption during use.

The subsequent sections of the chapter are dedicated to the description of the system's functional and executive design, as well as its experimental characterisation. Particular attention is paid to the description and measurement of the resulting stiffness when the SPSC makes contact with the grasped object, and how it varies as a function of the chamber geometry, as well as the initial set-up parameters of the pneumatic spring. The chapter also includes a discussion of the various techniques and materials that can be used to manufacture the chambers, as well as an assessment of the reliability of the resulting membranes.

The concluding section delves into the applications that are derived from this sensing unit, encompassing a grasp sensing system for robotic grippers and an haptic handheld device. In both applications, the internal pressure data of the chamber is integrated

with measurements of various types to enhance the sensing capabilities without compromising the mass and encumbrance of the solution.
The conceptualization and development of the SPSC-based sensing unit has been partially published by Colucci, Visconte and Quaglia in [166]. The sensing unit application for haptic devices has been later published by Duretto, Colucci, Jabbari and Quaglia in 2024 [167] and has been subject of a national patent application by Colucci and Quaglia, n. 102024000002331 filed in february 2024.

## 3.1 System concept

The underlying concept of the solution here described consists of a deformable membrane that is kept under pressure by an annexed auxiliary system. The latter is able to adjust the stiffness of the membrane when it is squeezed. Figure 3.1 shows the general architecture of the system. To offer the reader a reference, it is shown in the case of an application on robotic grippers, which will be detailed in the sub-section 3.4 together with the second application for the development of a haptic system.

Figure 3.1 (a) shows two interface elements, i.e. two SPSCs, each of which is connected to an auxiliary hydro-pneumatic system. It allows the indirect measurement of the contact force by reading the pressure inside the chambers, as well as enabling the adjustment of the stiffness of the SPSC itself by acting on the switching state of the directional valves present. The amount of squeezing undergone by the membranes is described by the variable $y_s$. The system is generally designed to be filled with a liquid, thus it behaves like a hydrostatic transmission when the membrane is squeezed by the grasped object. This causes the compression of the air mass enclosed in the auxiliary volumes $V_{C_1}, ..., V_{C_N}$ (the number of auxiliary volumes is generally variable). The directional valves $D_1, ..., D_N$ open or close the membrane connection to the auxiliary volumes. The switching of the valves, i.e. the connection or disconnection of the volumes, is only performed during system set-up. The spill valve $SP$ allows the correct spillage of air during the filling procedure of the membrane with the liquid and is, therefore, also only used during the initial set-up phases.

The check valves $C_1, ..., C_N$ allow the pressurisation of the system by connection to a pressure source, which is then disconnected during normal operation. The connection to any compressor, or generic compressed air source, is therefore made only in the initial set-up stages; and the system must be airtight for correct functioning.

## 3.2 Design methods

If leakage-free, the system behaves, in practice, as a pneumatic spring. The contact force $F$ generated on the grasped object depends, in general, on the structural stiffness of the membrane and the stiffness of the air spring itself. It will also depend on the stiffness

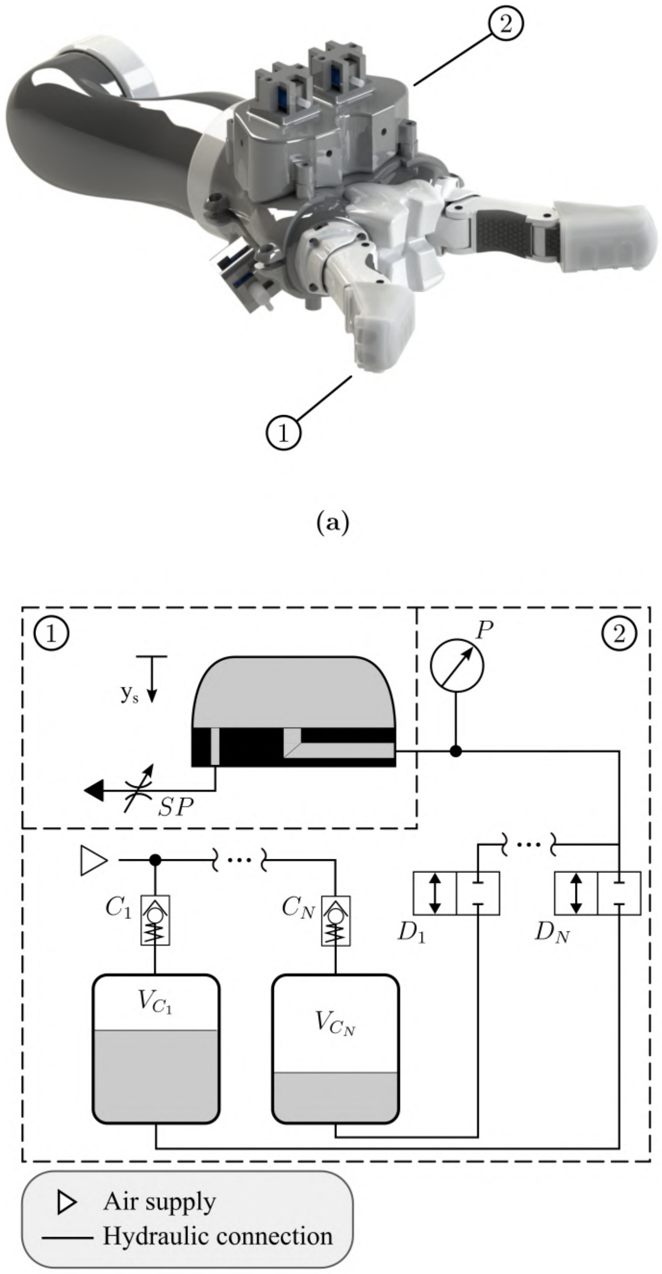

(a)

(b)

Figure 3.1: **(a)** A render of the sensing unit applied for robotic grasping and tactile sensing. **(b)** Schematic of the single sensing unit.

and geometry of the grasped object. For SPSC design purposes only, the following simplifying assumptions are made:

- The two stiffnesses mentioned above act in parallel. As will be seen in the following sub-section 3.3.1, this assumption will be reasonably valid during the experimental characterisation of the sensing unit.

- The grasped object is assumed as a plane uniformly squeezing the bladder, and it is considered as rigid.

Figure 3.2 diagrams the model resulting from the above assumptions. A single auxiliary volume is represented for simplicity. Let $F$ be the contact force between the bladder and the object:

$$F(y_s) = F_s(y_s) + p(y_s)\,A(y_s) \tag{3.1}$$

where $p(y_s)$ is the gauge pressure, and is solely a function of $y_s$. The pressure inside the chamber, on the other hand, depends on the polytropic law:

$$P(y_s) = P_i \left(\frac{V_i}{V(y_s)}\right)^n \tag{3.2}$$

where $n$ is the polytropic coefficient. $V_i$ is the volume of air in the initial rest state $y_s = 0$ of the system and depends on the switching state of the directional valves. In the case of $N$ connected auxiliary volumes, there are $2^N$ possible values that $V_i$ can take, depending on which volumes have been connected. There is also the case where no volume is connected to the SPSC. Finally, $P_i$ is the pressure of the system at rest, set by the pressure source during system setup. The volume of air in the m-th volume can

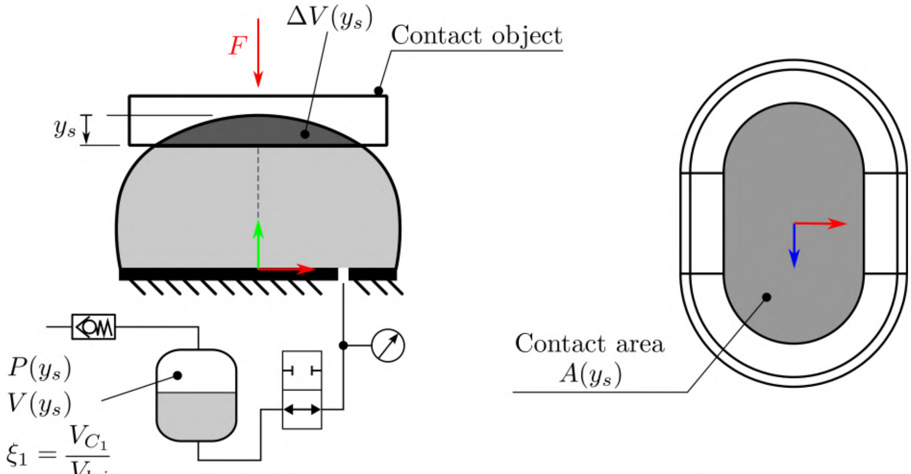

(a) (b)

Figure 3.2: **(a)** Simplification, for design purposes, of the contact between the SPSC and the grasped object by representing the latter by a rigid plane. For the purpose of simplicity, only one auxiliary volume is shown. **(b)** Contact area.

also be referred to the dimensionless parameter $\xi_m$:

$$\xi_m = \frac{V_i}{V_{b,i}} \tag{3.3}$$

where $V_{b,i}$ is the internal volume of the bladder in the undeformed configuration. It should be noted that it is generally necessary to fill the membrane with liquid in order to obtain at least one configuration where $\xi_m < 1$. If not, it is possible to remove the liquid and fill the system with air only. In this instance there is always $\xi_m > 1$, and $\xi_m = 1$ in the case where the SPSC is not connected to an auxiliary volume.

The volume $V(y_s)$ will instead be equal to:

$$V(y_s) = V_i - \Delta V(y_s) \tag{3.4}$$

i.e. it depends on the volume that is squeezed during the contact.

In addition to depending on the magnitude of the squeezing level $y_s$, $\Delta V(y_s)$ and $A(y_s)$ also depend, broadly speaking, on the geometry and stiffness of the gripped object. In the design phase, where these aspects are neglected, they depend only on the geometry of the SPSC, and can therefore be defined as geometric parameters.

It should be emphasised that the feed pressure must be the same in all auxiliary volumes to avoid unwanted flows in the event of a valve switching.

Both the geometric and the set-up parameters influence the performance of the system. In fact, it is possible to rewrite equation 3.1 and equation 3.2 as follows:

$$P(y_s) = P_i \left( \frac{\xi_m V_{b,i}}{\xi_m V_{b,i} - \Delta V(y_s)} \right)^n \tag{3.5}$$

$$F(y_s) = F_s(y_s) + \left( P(y_s) - P_{amb} \right) A(y_s) \tag{3.6}$$

Equation 3.6 shows the link between the physical quantity measured and the magnitude of the SPSC squeezing. The respective first order derivatives of $F$ and $P$ are also of interest. The former one represents, in fact, the stiffness of the sensing system:

$$\frac{dF}{dy_s} = k(y_s) = k_s(y_s) + p(y_s)\frac{dA}{dy_s} + A(y_s)\frac{dp}{d\Delta V}\frac{d\Delta V}{dy_s} \tag{3.7}$$

where $k_s$ represents the structural stiffness of the membrane. The second term shows, on the other hand, the part of the stiffness due to the increase in contact area during squeezing. On other hand, the latter term contains both the first order derivative of $p$ as defined in Equation 3.5 and the increase in volume squeezed during grasping.
The term:

$$\frac{dp}{dy_s} = \frac{dp}{d\Delta V}\frac{d\Delta V}{dy_s} \tag{3.8}$$

i.e. the first order derivative of the internal pressure with respect to the squeezing level, represents the sensitivity of the sensing unit. By adjusting the geometric parameter $\Delta V$ and the setup parameters, it is therefore possible to adapt the sensitivity of the system to the design requirements.

### 3.2.1 SPSC geometry

While the effect of $P_i$ and $\xi_m$ on the system performance is easily understood, i.e. by increasing the pressure or reducing the value of $\xi_m$ it is possible to increase stiffness and sensitivity of the system, it is also of interest to analyze the effect of the SPSC geometry. In fact, there are no studies in the literature that analyze the influence of the nominal geometry of the SPSC on its behavior, and it is generally assumed to be a spherical cap shape [157, 168, 164].

The generic description of the SPSC can be schematized as shown in Figure 3.3. In the midplane $\mathcal{S}$, the centerline of the cross-section is obtained by a sequence of three arcs, tangent to each other at points $P_{[1,2]}$. The three arcs have their centers at $O_{[1,2,3]}$ with a central angle equal to $\alpha_{[1,2,3]}$. The first arc intersects the $\hat{\jmath}$ axis at $P_0$, and its center $O_1$ lies on $\hat{\jmath}$ itself. The third arc, instead, intersects the $\hat{\imath}$ axis at $P_3$, but there are no constraints on $O_3$. This geometry is then mirrored with respect to $\hat{\jmath}$ to obtain the complete section, of which $s$ represents the thickness. It is then extruded along $\hat{k}$ for a length equal to $l$ ($< \hat{\imath}, \hat{\jmath} >$ remains the midplane of this extrusion). To close the geometry, the half-section in Figure 3.3 (b) is used for a revolute extrusion, on both sides of the SPSC, performed with respect to the $\hat{\jmath}$ axis by a value equal to $\pi$.

The independent geometric parameters of the geometry are collected in Table 3.1. The values in the first row of the table generally depend on the dimensions of the link of the gripper on which the sensing system is to be mounted. Note that the following relationship holds:

$$L = l + 2\,i \tag{3.9}$$

The values in the second row affect, respectively, the desired squeezing stroke on the

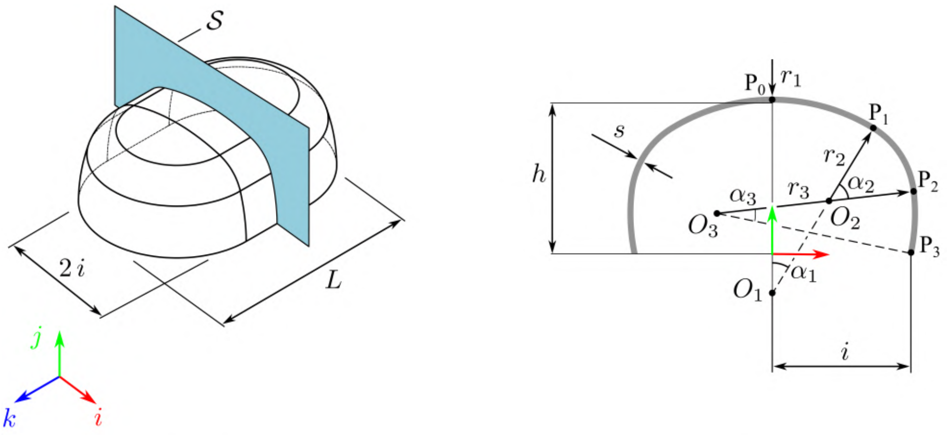

(a) (b)

Figure 3.3: **(a)** Representation of the bladder in an axonometric view. $\mathcal{S}$ represents the intermediate transverse plane. **(b)** Section in the $\mathcal{S}$ plane. This geometry is extruded along $\hat{k}$ and then revolved around $\hat{\jmath}$ to close the SPSC.

Table 3.1: SPSC independent parameters.

| Name | Description |
|---:|---|
| $2\,i$, $L$ | Semi-width and length |
| $h$, $s$ | Height and thickness |
| $a$, $b$, $c$, $d$ | Geometry form factors |

SPSC, and the structural stiffness of the same. The values in the last row, instead, establish the type of SPSC obtained. They are defined as follows:

$$a = \frac{x_{P_1}}{i} \quad , \quad b = \frac{y_{P_1}}{h} \quad , \quad c = \frac{x_{P_2}}{x_{P_1}} \quad , \quad d = \frac{y_{P_2}}{y_{P_1}} \tag{3.10}$$

Figure 3.4 shows the intermediate cross-section of four types of SPSCs, obtainable by this formulation, by keeping $i$ and $h$ constant. Types A and D exhibit $b$ values greater than 0.9, which, in conjunction with an $a$ value of approximately 0.6, describe the flat shape achieved at the SPSC tip. The shape of the side walls, straight for Type A and angled for Type D, is defined by the parameter $c$, which is larger in the case of the latter type. The pointed shape of Type C, on the other hand, is mainly determined by the low value of $a$. Type C is the one that most closely reproduces, in the cross-section, an arc of a circle.

## 3.3 SPSC prototyping and testing

For the purposes of this study, the fabrication of the SPSCs was carried out by implementing the most prevalent techniques for soft robotics manufacturing previously outlined in chapter 1.2.1. Indeed, similarly to what was illustrated for the BiSoft.Q in the previous chapter, the objective is to make the technology in question easily replicable in research laboratory environments.

Unlike the soft bi-directional actuator, the SPSC must be perfectly sealed to prevent pressure loss. Any air leak can alter measurement results and render the sensing unit unusable. The nominal geometry of the SPSC, on the other hand, is definitely simpler and easier to implement.

Table 3.2 summarizes the materials used for the realization of the SPSCs and the relative manufacturing methodology.

An early version of the bladders was realised by compression moulding, a method widely used in the literature due to its low cost and high simplicity[1]. With the advent of FDM printers, mould making is generally done in the laboratory, using a rigid plastic

---

[1] An extensive description of construction methods for soft robot was presented in subsection 1.2.1

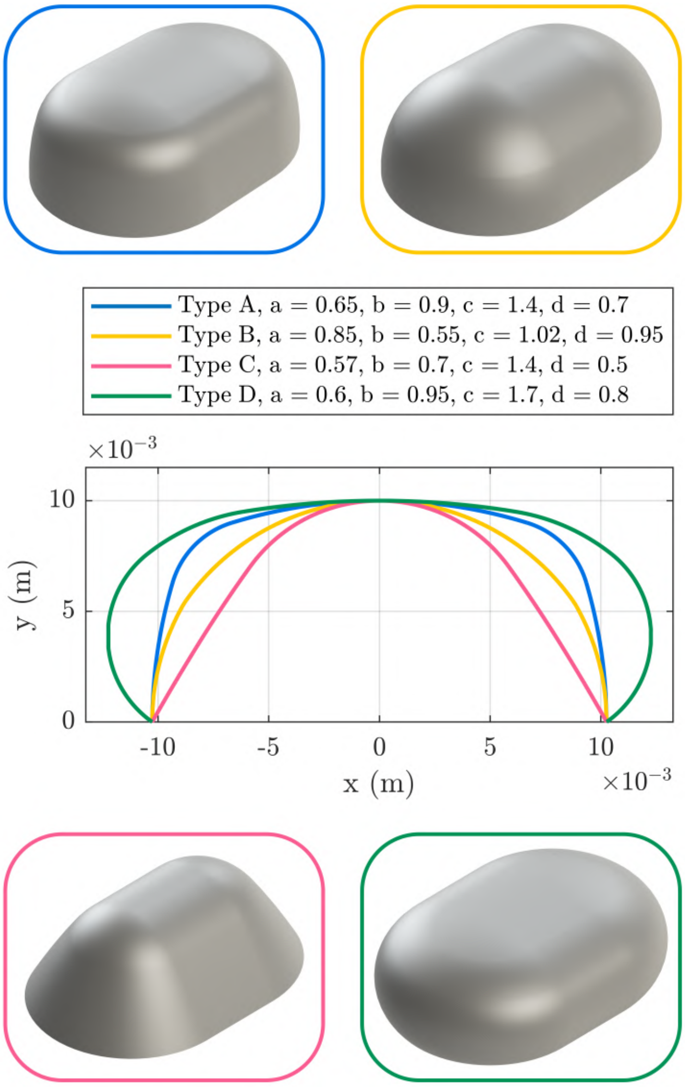

Figure 3.4: Geometries obtainable through the described formulation, represented in the $\mathcal{S}$ plane of Figure 3.3 (a). $i = h = 10$ mm. Type A and D exhibit a flat shape at the SPSC tip. Type A also has straight vertical side walls, whereas Type D has curved walls. Type C exhibits a pointed tip and straight, inclined side walls, while Type C resembles an arch of a circle.

material such as PLA or ABS, and there are also numerous examples of guidelines and whitepapers made available by the researchers themselves regarding the process [169, 170, 171]. Figure 3.5 (a) shows an exploded view of the moulds used in this study, represented in axonometric view. The mould in this case only makes the shell described in Figure 3.3, and consists of two parts. After mixing part A with part B according to the manufacturer's instructions, and carrying out the de-gassing process in a vacuum

Table 3.2: Materials used for the fabrication of the SPSCs.

| **Material** | **Manufacturing methodology** | **Hardness** | **Tensile str.** (MPa) | **Elongation at break** (%) | **Tear str.** (kN $m^{-1}$) |
|---|---|---|---|---|---|
| Ecoflex 00-50(1) | Compression moulding | 00-50(2) | 2.17 | 980 | 8.76 |
| Easy Comp. AS40(1) | Compression moulding | 36-45A | >3.5 | >250 | >13 |
| Recreus TPU | FDM 3D print | 63A(3) | 26(3) | 950 | 40(4) |
| Formlabs elastic (V2, cured) | SLA 3D print | 50A(2) | 3.23 | 160 | 19.1 |

(1) The official catalogue values are subject to modification by the incorporation of cotton fabric during the process of compression moulding.
(2) ASTM D-2240
(3) DIN 53504-S2
(4) ISO 34-1

chamber[2], the liquid silicone mixture is poured into the lower part of the mould, shown in the figure in red colour. The upper part, shown in blue, features the punch that forces the silicone to fill the meatus between the two parts of the mould when closing the mould. Correct positioning between the two parts of the mould is achieved by means of four prismatic couplings, visible on the edges of the moulds. The lower part also has a channel for collecting excess silicone. After closing the mould, the curing process was carried out at room temperature (23 °C), and no post-curing was done. The highly elastic properties of silicone would not allow the nominal geometry to be maintained when the membrane was pressurised. For this reason, it is necessary to apply some strengthening fibres, which allow the bladder to be crushed but do not allow its uncontrolled volumetric expansion. For this purpose, a cotton gauze was placed inside the mould. For the correct positioning of the gauze inside the silicone matrix, it was sufficient to place the gauze halfway through the silicone casting process in the mould, then cover it with the remaining quantity of silicone. Finally, to facilitate the removal of the moulded part, the two parts of the mould were covered with a film of releasing agent.

Finally, the membrane was closed by means of rigid attachment with a rigid lower

---

[2] The degassing process must be carried out to eliminate the air bubbles trapped in the compound during the mixing of the two parts. It involves an intermediate phase in which the mixture greatly increases its volume due to the expansion of the air bubbles, after which the mixture collapses leading to the evacuation of the bubbles.

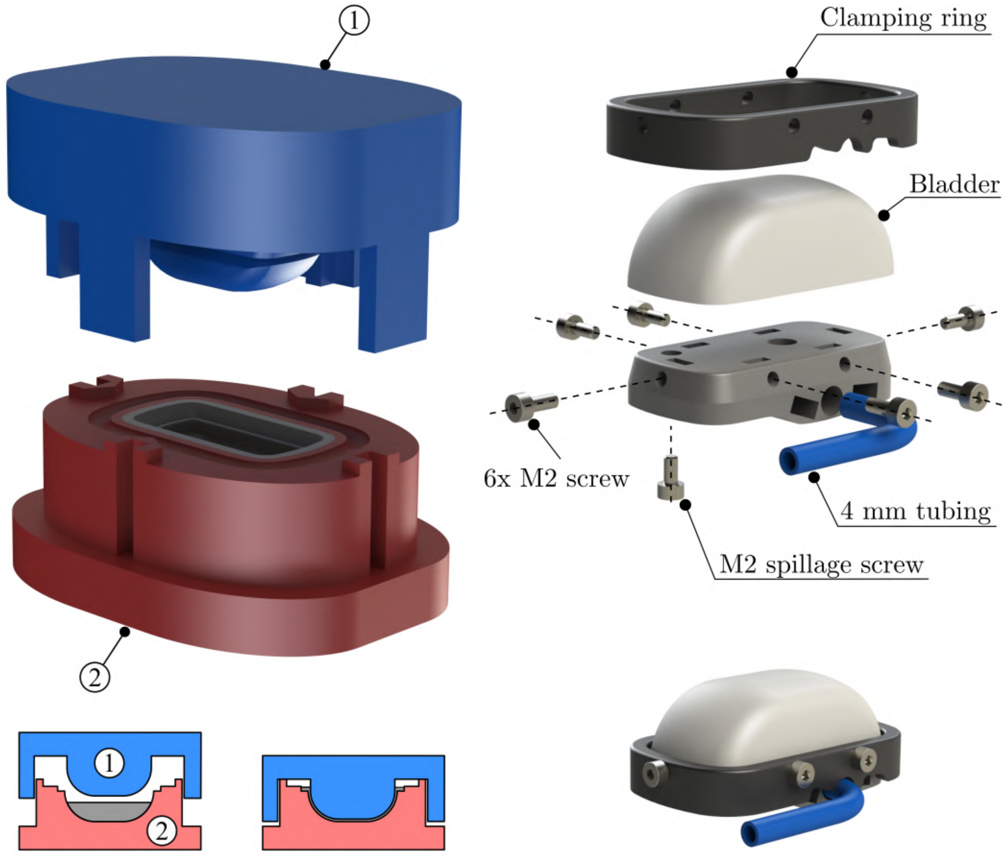

(a)

(b)

Figure 3.5: **(a)** Exploded view of the molds for the production of SPSC in silicone, shown in an axonometric view. A cotton strengthening fabric is inserted during the silicone pouring to inhibit uncontrolled volumetric expansion of the bladder when pressurized. **(b)** Exploded view of the SPSC in assembly design, where the deformable part is made of silicone via compression molding. Minor air leaks are prevented by silicone sealant or two-component adhesive.

base, according to the assembly diagram in Figure 3.5 (b). Similarly to the BiSoft.Q actuator, the base plate has the multiple tasks of closing the chamber under pressure, allocating the internal tubing to pressurise the chamber and rigidly connecting the sensing unit to the robotic gripper. The rigid connection was made by means of an external clamping ring, fixed to the headplate by screws. Any minor air leaks were prevented by means of two-component glue or silicone sealant. Prior to tightening the screws on the baseplate, for example, a quantity of selalant had to be applied to the thread. This assembly design also allows for the integration of a spillage screw into the base, should it be necessary to fill the SPSC with liquid.

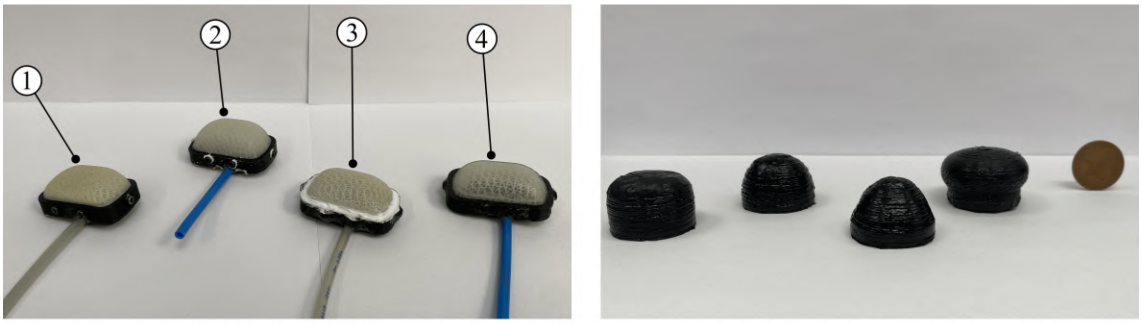

(a)

(b)

Figure 3.6: Soft pneumatic sensing chambers prototypes. Coin for scale. **(a)** Compression moulded (type A) silicone bladders. $h = 10$ mm, $i = 8$ mm, $l = 11$ mm, $a = 0.70$, $b = 0.75$, $c = 1.45$, $d = 0.61$. 1: EC AS40 $s = 1$ mm, 2: EC AS40 $s = 2$ mm, 3: Ecoflex 00-50 $s = 1$ mm, 4: Ecoflex 00-50 $s = 2$ mm. **(b)** FDM-manufactured monolithic TPU membranes (typologies A-D).

Figure 3.6 (a) shows four prototypes of the SPSC made by means of the above. The nominal geometry is type A, and its geometrical parameters are shown in the figure caption. In the case of both EcoFlex 00-50 and Easy Comp. AS40, SPSCs with thickness $s \in [1, 2]$ mm were manufactured. This manufacturing methodology, however, requires a high time effort. Firstly, any change in geometry requires the production of a new mould. In addition, the curing process takes several hours to complete[3].

In order to speed up and simplify the process, thus, SPSC prototypes were also built by additive manufacturing. Figure 3.6 (b) shows TPU 60A membranes made by FDM, in the four types identified in Figure 3.4. Similar results were also obtained by SLA, in which case materials with shore hardness ranging from 40 to 50A were used. Compared to FDM, the SLA method guarantees a higher finish of the part, but requires post-processing operations for cleaning and curing the part, and is also more expensive.

For further considerations regarding the durability and reliability of the manufactured SPSCs, please refer to sub-section 3.3.2.

### 3.3.1 Characterization and hysteresis

In this subsection, the effect of the geometrical parameters in Figure 3.3 on the stiffness and sensitivity of the system is illustrated. In the simple case of contact with a plane that uniformly squeezes the SPSC, it should be recalled that they depend on the set-up conditions of the system, i.e. the terms $P_i$ and $V_{C,i}$, as well as the contact area $A(y_s)$ and the volume of pressurised air $V(y_s) = V_{C,i} - \Delta V(y_s)$.

FEA methods allow the estimation of these terms, as well as the overall stiffness and

---

[3] 3 hours for Ecoflex 00-50, 24 hours for Easy comp. AS40.

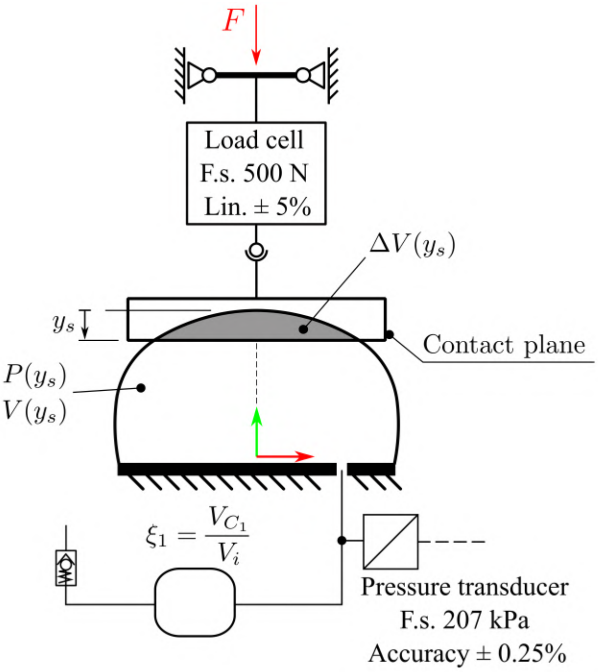

Figure 3.7: Static characterization experimental layout.

sensitivity [165, 157], but the aim here is to simplify and speed up the characterisation of the sensing unit by means of experimental identification.

Figure 3.7 shows the experimental set-up used for this purpose. The SPSC was connected to a single auxiliary volume, and a pressure transducer reads the pressure value inside the chamber. A rigid plane is used to press down on the membrane, which is constrained by a linear guide[4] to translate along $\hat{\jmath}$ along only. A load cell reads the value of the pressing force $F(y_s)$.

Figure 3.8 and following show the characterisation results for the four SPSCs in TPU 60A shown in Figure 3.6 (a). A first test, the results of which are shown in the respective sub-figures (a), was carried out to characterise only the structural stiffness part of the membrane $k_s$. During a loading and unloading cycle, starting from the rest configuration $y_s = 0$, the material exhibits hysteretic behaviour. In the four graphs $F_s$ versus $y_s$, the average value of $F_s$ over the cycle is identified by a dashed black line. The ratio between the hysteresis area and the area subtended by this average value ranges between 15 % (type C) and 38 % (type A).

Sub-figures (b) then show the experimental data of squeezing force $F$ and internal pressure $P$ acquired with set-up values of $\xi_1 \approx 6.2$ and $P_i \in [120, 160]$ kPa. Recalling

---

[4] The guide resolution is $10^{-2}$ mm

Equation 3.6, it is possible to estimate the contact area as:

$$A(y_s) = \frac{F(y_s) - F_s(y_s)}{p(y_s)} \tag{3.11}$$

The volume of squished air, on the other hand, depends on the pressure reading alone using the polytropic law:

$$\Delta V(y_s) = (V_{C1} + V_i)\left(1 - \frac{P_i}{P}^{\frac{1}{n}}\right) \tag{3.12}$$

The two values, with relative variation spans, are shown in sub-figures (c). The D-type SPSC presents the largest contact area, with increasing monotonic behaviour. The remaining three membranes present, in the final squeezing phase relative to values of $y_s > 7$ mm, a decrease in the contact area value. This is quite pronounced in type C, while type A and B show a less marked inflection. This could be due either to an actual inward deflection of the membrane (in support of this, the decrease in area is smaller for higher $P_i$), or to the simplifying assumption introduced, which does not consider the dependence of $k_\mathrm{s}$ on internal pressure.

Nevertheless, once $F_\mathrm{s}(y_\mathrm{s})$, $A(y_\mathrm{s})$ and $\Delta V(y_\mathbf{s})$ have been identified, it is possible to estimate the behaviour of the sensing system in terms of $F$ and $P$ according to the same equations as above. Furthermore, since the variation span in sub-figures (c) is relatively small, it is possible to estimate $A(y_\mathrm{s})$ and $\Delta V(y_\mathrm{s})$ by means of a single pressure test. Sub-figures (d) show the theoretical versus experimental comparison of $F$ and $P$, where the model is based on a single test (e.g. the test at $P_i = 140$ kPa). The method turns out to be quite reliable, with evident deviations only in the test at $P_i \in [150{,}160]$ kPa for Type C. In the remaining cases, however, the estimation is enough accurate, and notably reduces the time required for characterisation[5].

---

[5] In incremental steps of 0.2 mm, the two tests take a total time of about 20 min

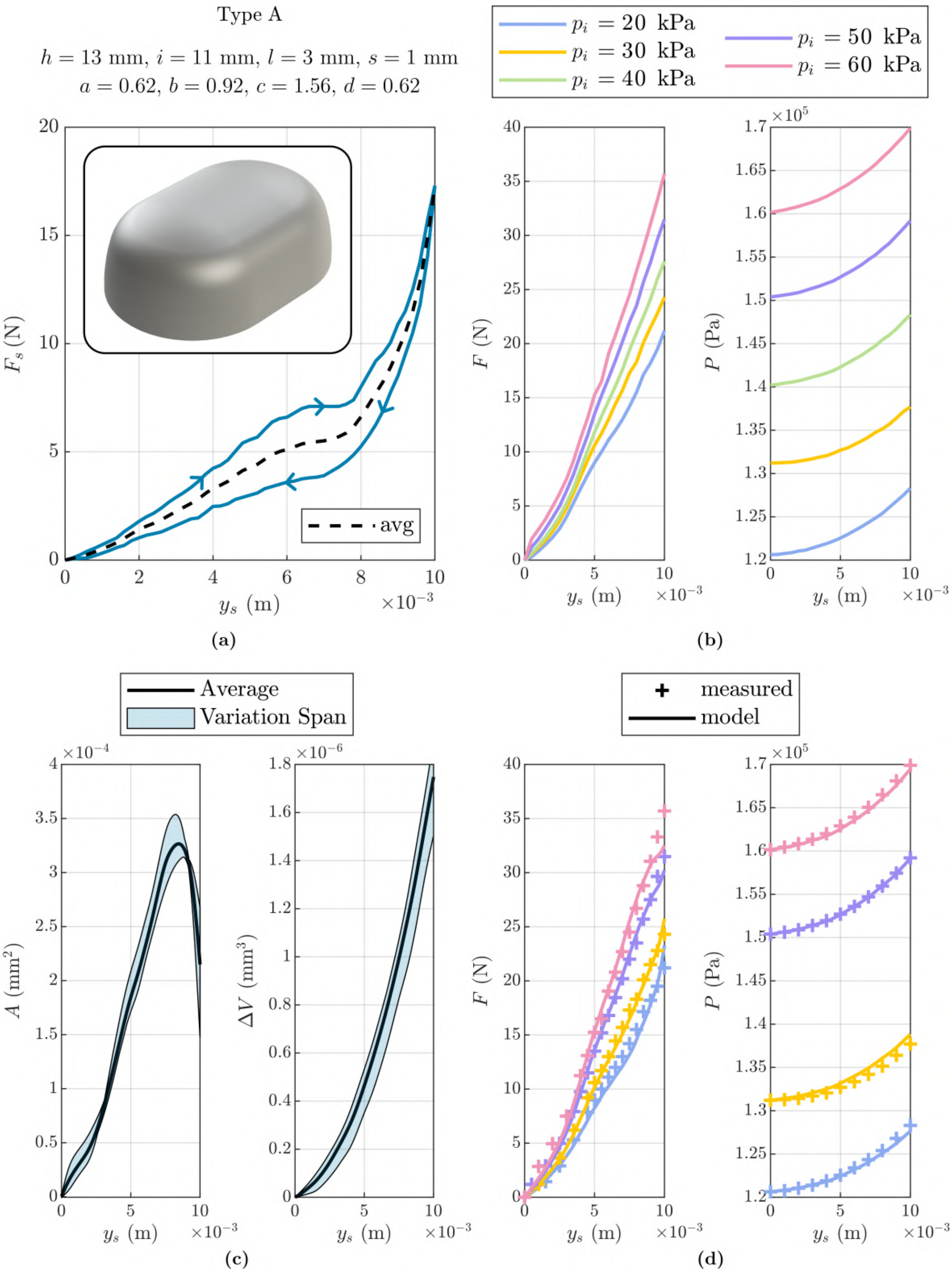

(a) (b) (c) (d)

Figure 3.8: Type A experimental results with $\xi = 6$. **(a)** Structural stiffness and hysteresis. **(b)** Contact force and pressure. **(c)** Contact area and squeezed volume. **(d)** Model versus experimental comparison, $P(y_s = 0) = 140$ kPa test is used for the model.

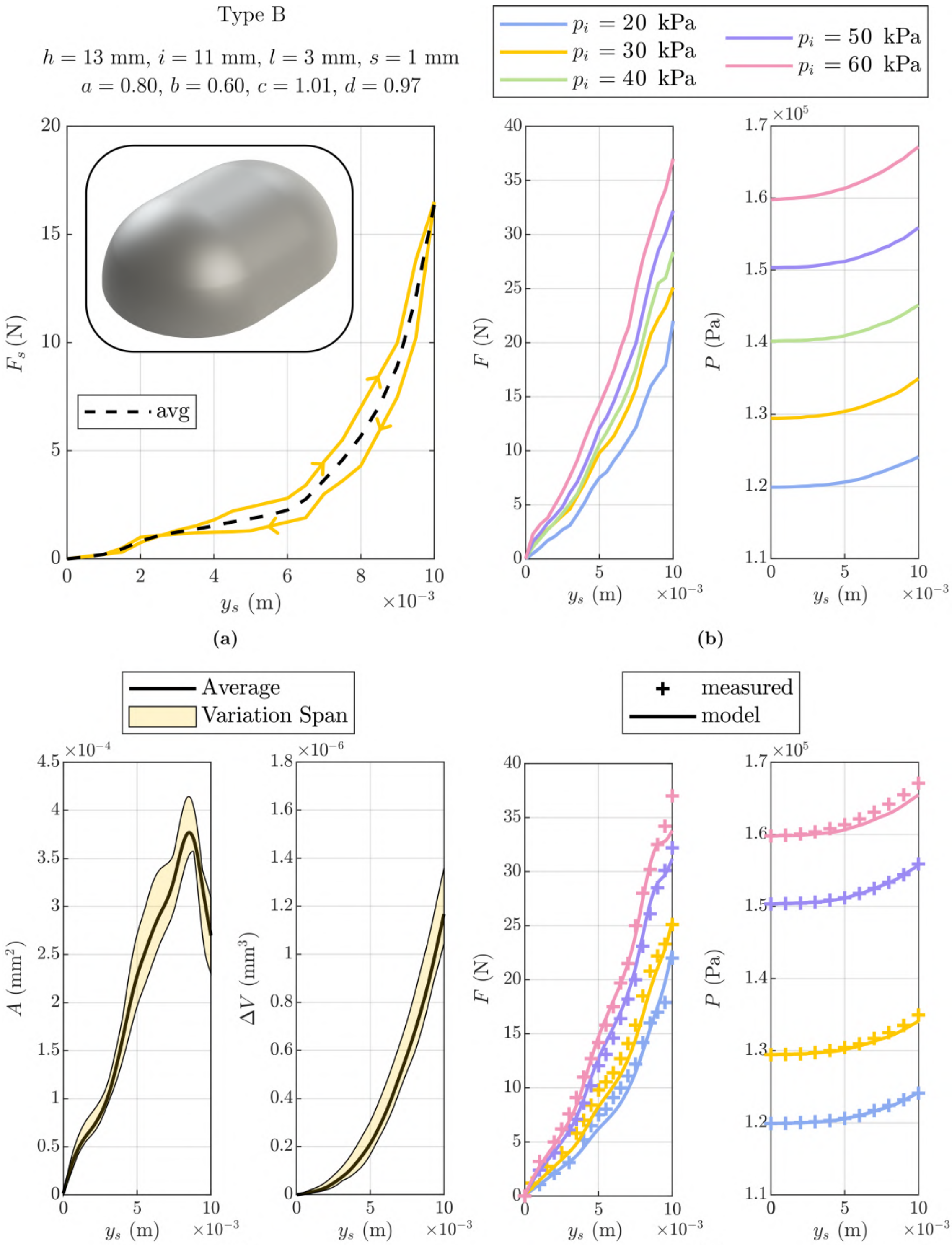

(a) (b) (c) (d)

Figure 3.9: Type B experimental results with $\xi = 6$. **(a)** Structural stiffness and hysteresis. **(b)** Contact force and pressure. **(c)** Contact area and squeezed volume. **(d)** Model versus experimental comparison, $P(y_s = 0) = 140$ kPa test is used for the model.

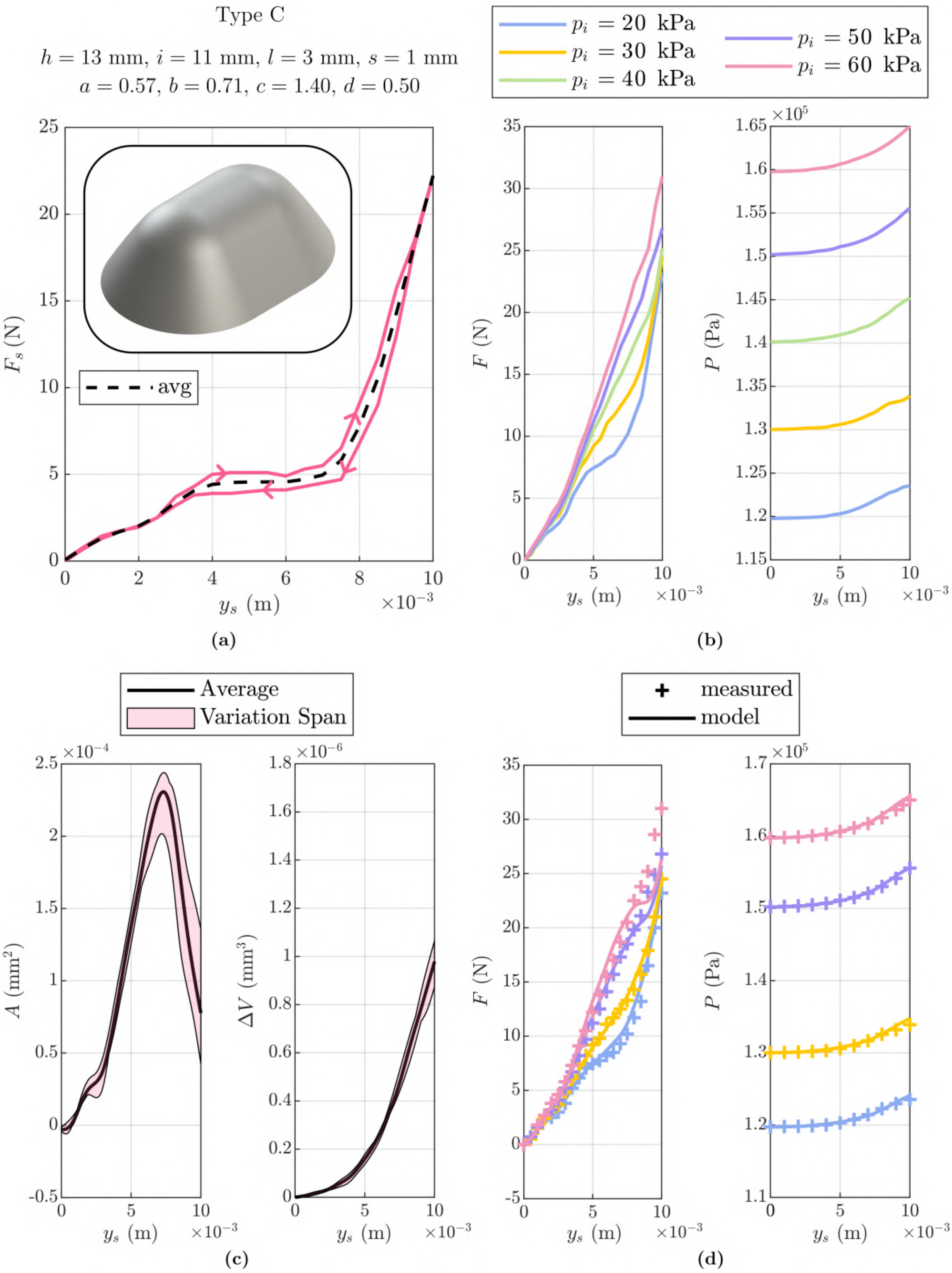

Figure 3.10: Type C experimental results with $\xi = 6$. **(a)** Structural stiffness and hysteresis. **(b)** Contact force and pressure. **(c)** Contact area and squeezed volume. **(d)** Model versus experimental comparison, $P(y_s = 0) = 140$ kPa test is used for the model.

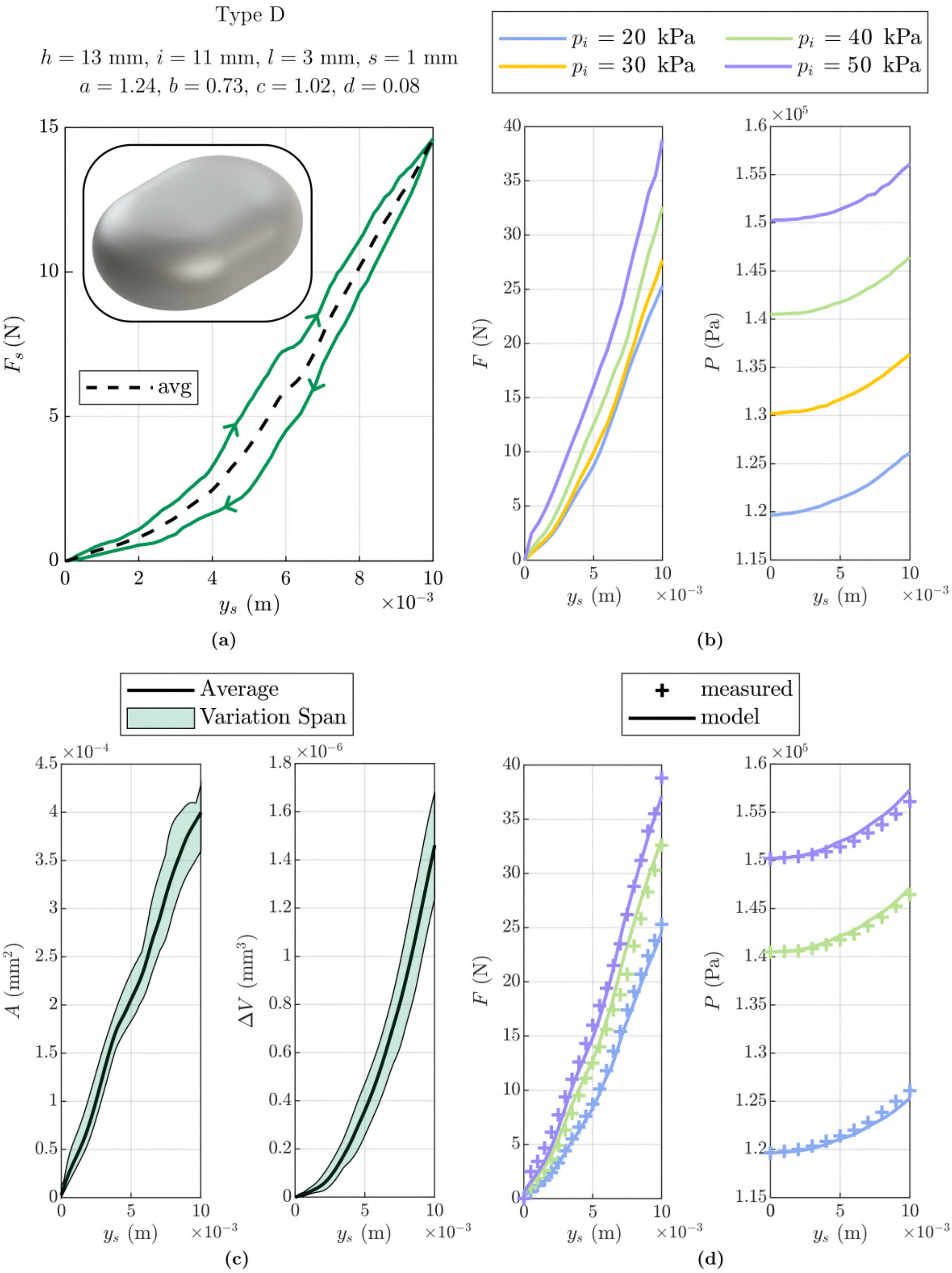

Figure 3.11: Type D experimental results with $\xi = 6$. **(a)** Structural stiffness and hysteresis. **(b)** Contact force and pressure. **(c)** Contact area and squeezed volume. **(d)** Model versus experimental comparison, $P(y_s = 0) = 130$ kPa test is used for the model.

Figure 3.12 compares the characterization results for the four SPSC types. In terms of sensitivity, i.e., $P(y_s)$, Types B and C are substantially similar, while Type D shows slight differences, with higher sensitivity for approximately $y_s < 0.6\,h$. Type A, on the other hand, deviates significantly due to a higher $\Delta V(y_s)$ compared to the other three types.

In terms of structural stiffness, Types A and C exhibit an initial interval with moderate slope, a central phase with nearly zero slope, and a final interval with high slope. Type B, on the other hand, stiffens for values of about $y_s > 0.6\,h$. For all three types, the final stiffening phase is due to the activation of edge stiffness. In terms of contact force $F$, Type C shows the lowest values among all, despite higher stiffness, due to its smaller contact area. Type D exhibits the opposite behavior, with $F$ being higher than all other cases for $y_s > 0.7\,h$ due to its larger contact area.

In conclusion, Type A is preferable when high sensitivity of the sensing unit is required, while Types B and C have lower sensitivity but higher contact force. Type D also has the largest contact area among the four types. Due to the high structural stiffness for high squeezing level and the significant deviation between theoretical and experimental results in this phase, Type C is of interest only for moderate squeezing, i.e., $y_s < 0.5\,h$, and when modest contact areas are required.

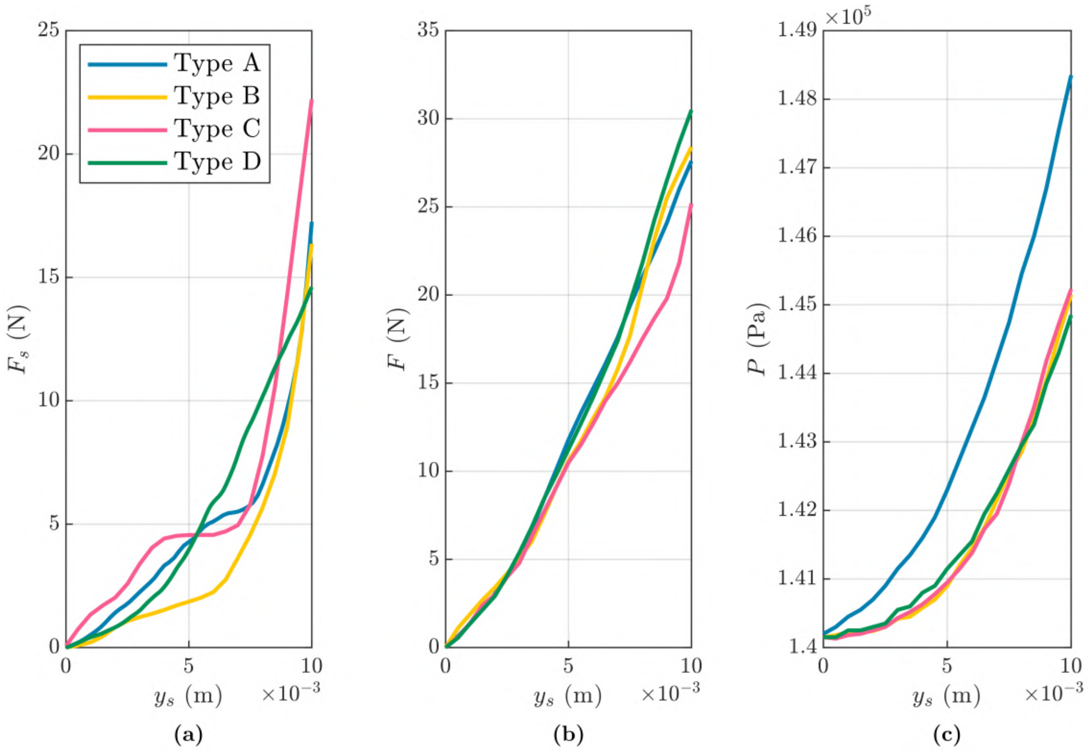

Figure 3.12: Characterization results for the four bladder typologies. **(a)** Structural stiffness (average). **(b-c)** Contact force and internal pressure. $\xi_1 \approx 6.2$

### 3.3.2 Reliability

Notwithstanding the fact that the research activity presented here is still at the prototype level, and not at the level of a commercial product, a minimum quantification of the reliability of the membranes is considered of interest. Indeed, it must be recalled that the sensing unit presented here is based on a closed, pressurised pneumatic system, and any damage to the SPSC would significantly damage its operation.

Firstly, SPSCs were tested at a pressure of $p_i = 100\,\mathrm{kPa}$ (gauge). The membrane was classified as compliant if it was free of air leaks for a duration of thirty minutes [157]. It was also observed that, at this pressure, the membranes underwent slight deformation, with an approximate rise of $0.1\,h$ along the $\hat{k}$ axis. The maximum geometry imposed in the design, as well as the type of membrane, remained valid. Subsequently, it was considered worthwhile to verify the fatigue limit of the membranes. To this end, the SPSC was subjected to a cyclic squeezing cycle imposed by a pneumatic piston. During the cycle, the bladder transitioned from the resting configuration $y_s = 0$ to the maximum crushing configuration $y_s = y_{s,\max}$. The test bench configuration utilised for this investigation is depicted in Figure 3.13. In this instance, the SPSC part is of type B, fabricated from TPU 60A by Recreus employing the FDM methodology. The nominal geometry is analogous to that illustrated in Figure 3.9. The pneumatic cylinder head functions as an infinitely rigid plane that exerts pressure on the specimen, similarly to the description in Figure 3.7 (a) for the SPSC characterisation. A second type of test performed was a puncture test with a conical puncture probe. This type of test is described in standards

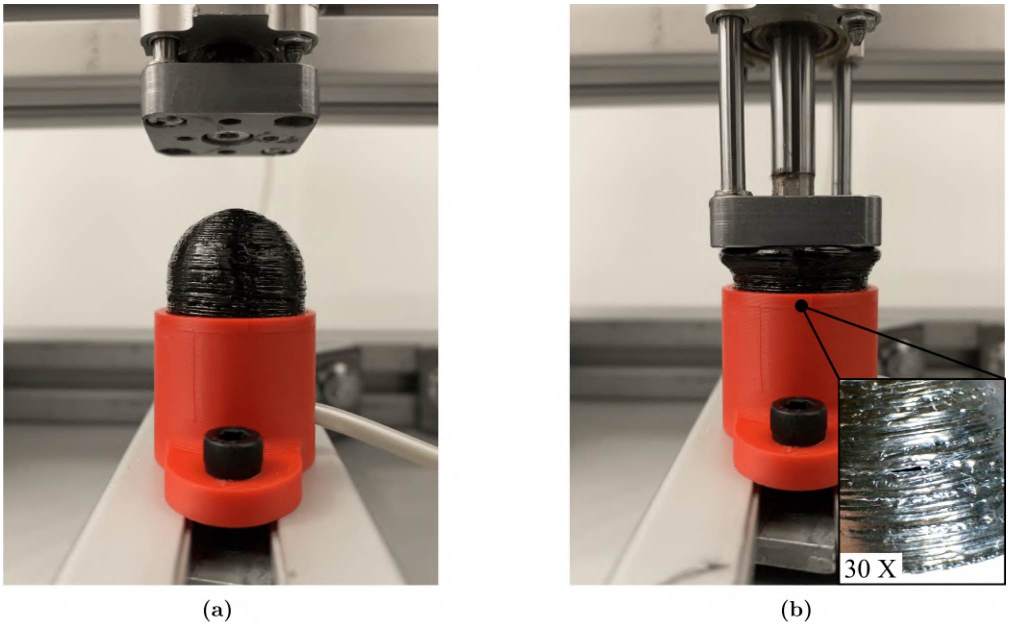

(a)

(b)

Figure 3.13: Fatigue test on an SPSC Type B made of TPU 60A. **(a)** Membrane at rest. **(b)** Membrane completely squeezed and resulting damage.

for evaluating the puncture resistance of protective clothing materials (e.g. plastics, coated fabrics, flexible materials) [172, 173], and it is used in the literature to test the puncture resistance of rubber membranes [174]. In the present case, where such membranes are the physical interface between a robotic gripper (or the haptice device) and the object to be gripped (or the human being), it provides an indication in the case of gripping objects with sharp or pointed edges. Figure 3.14 shows the test bench in the two configurations of rest and maximum puncture. The geometry of the conical probe is specified in Figure 3.14 (a), while (b) shows a detail of the type of damage suffered by a type B specimen made of Elastic V2 material from Formlabs (geometry definition in Figure 3.9).

In both types of test, membrane damage was automatically detected by measuring the pressure inside the chamber, with a threshold value of 0.95 $p_i$.

Table 3.3 summarises the results of the tests for three specimens with the same geometry and made with the four different materials described above, and Figure 3.15 shows the damages occurred. The silicone-moulded bladder proved to be the most resistant in the fatigue tests, reaching 5000 cycles without damage. For puncture tests, however, it proved to be the most fragile, with maximum forces of 27 N. It should be noted, as a reference, that the Kinova KG2 on which the SPSCs were mounted can apply

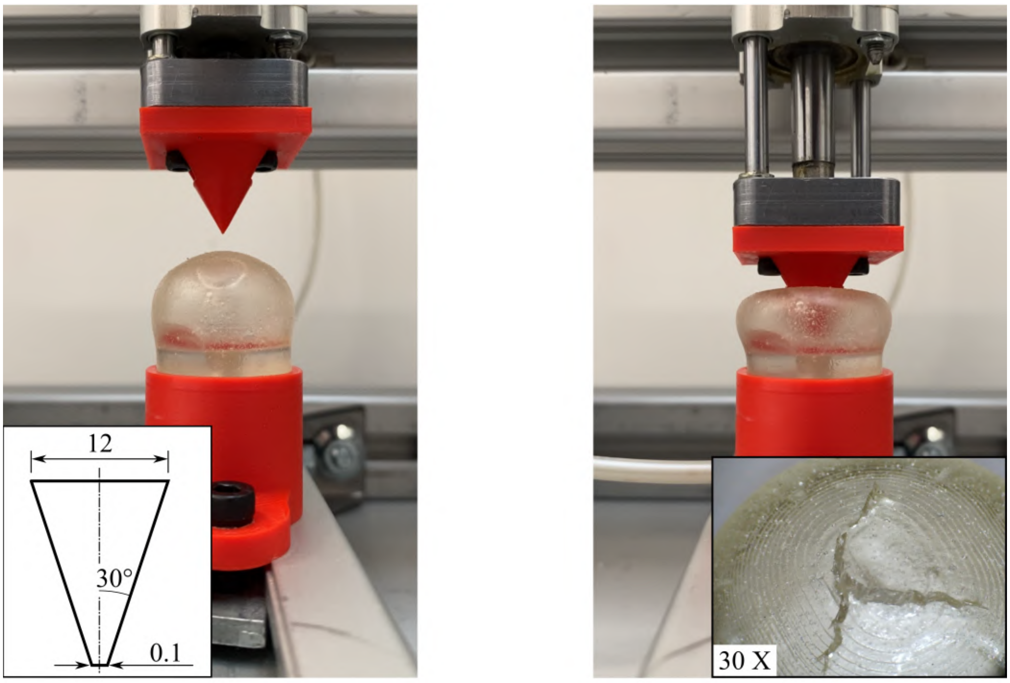

(a) (b)

Figure 3.14: Puncture test on an SPSC Type B made of Elastic 50A. **(a)** Membrane at rest and conical puncture probe geometry. **(b)** Membrane when punctured and resulting damage.

Table 3.3: Results of the destructive tests on the SPSCs.

| **SPSC type** | **Manufacturing methodology** | **Fatigue test**(1) (cycles to failure) | **Puncture test**(1) Force to failure (N) |
|---|---|---|---|
| Easy Comp. AS40 | Compression moulding | >5000(2) | 27 |
| Recreus TPU 60A | FDM 3D print(3) | 4100 | 45 |
| Formlabs elastic (V2, cured) | SLA 3D print(3) | 1330 | 40 |
| Formlabs silicone (40A, cured) | SLA 3D print(3) | 2075 | >80(2) |

(1) The bladder supply pressure for this test is $p_i = 50$ kPa (gauge).
(2) The membrane has passed this test without rupture.
(3) The print plane is parallel to the plane $< \hat{\imath}, \hat{\jmath} >$ reported in Figure 3.3.

gripping forces on the distal phalanx of approximately 40 N [156].

If both fatigue tests and puncture tests are considered, the TPU 60A membrane fab-

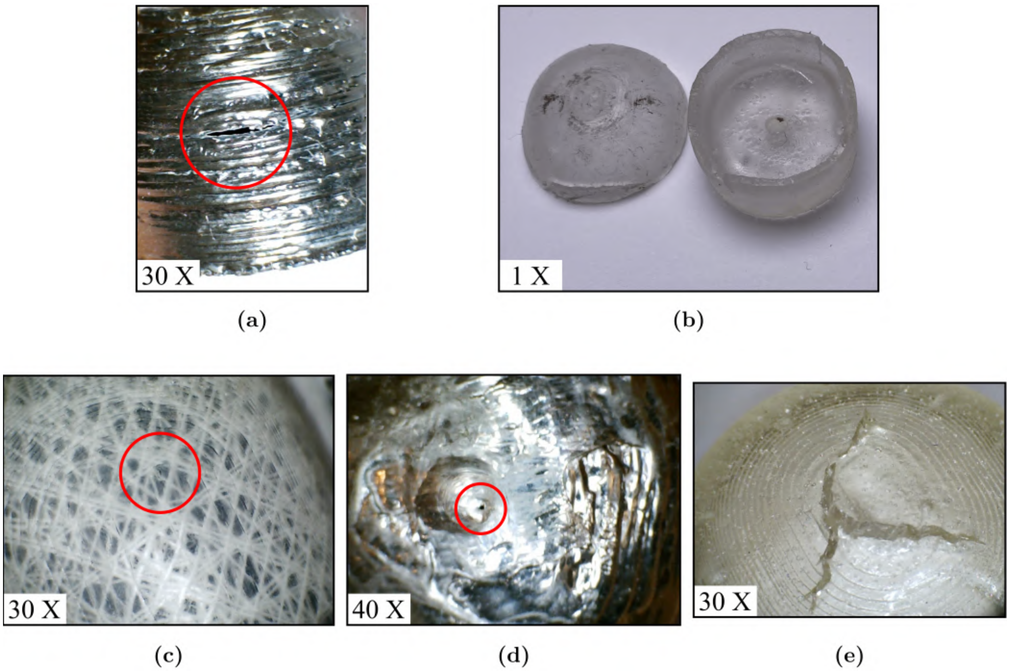

(a) (b)
(c) (d) (e)

Figure 3.15: Types of damage incurred by bladders during testing. Minor damages are marked with red circles. **(a)** TPU 60A, fatigue test. **(b)** Elastic 50A, fatigue test. **(c-e)** Easy Comp. AS40, TPU 60A and Formlabs Elastic 50A, puncture test.

ricated via FDM proves to be the most reliable. SPSCs produced through compression molding exhibit high fatigue resistance but low puncture resistance, while SPSCs made from the same material using SLA demonstrate moderate fatigue resistance and high puncture resistance. Elastic 50A, on the other hand, proves to be particularly unreliable.

Further attention must be given to the type of damage and the possibility of repair in the event of failure. Fatigue tests resulted in damage forming in the $< \hat{\imath}, \hat{\jmath} >$ plane of Figure 3.3 for both TPU and Elastic. This outcome was expected since, in both cases, this plane is parallel to the printing plane during the fabrication of the membranes. However, the damage observed in the TPU SPSC is significantly smaller compared to that of the Elastic SPSC, which instead undergoes total membrane failure. A similar result is observed in puncture tests.

The extent of the damage, as well as the material type, allows for repair in the case of TPU by melting and locally applying additional TPU using a soldering tip. In contrast, damage to Elastic material is irreparable. Similarly, for SPSCs in silicone fabricated through compression molding or SLA, the puncture test resulted in minor (or negligible) damage, which can be repaired by sealing the damage with a silicone sealant.

## 3.4 Application in Service Robotics

In this section, the described technology will be applied in two service robotics contexts. The first one follows what has been mentioned throughout the chapter and also alluded to in Figure 3.1 (a), namely the use of SPSCs as soft fingertips for robotic grippers. In this case, the aim will be to provide the global planner of the manipulator with additional information, such as the grasp success, the position of the grasped object and its stiffness. In the second application, the soft bladders will be used as interface elements with the fingers of a human user, and will be a constituting part of a wireless haptic device.

In both cases, the development of the technology starts from the design need for an interface element, in this case the SPSC, with variable stiffness when squeezed. Furthermore, the geometry of the bladder will be adapted to allocate additional elements, i.e. sensors or actuators, to increase its functionality.

### 3.4.1 Pneumatic sensing chambers for robotic manipulation

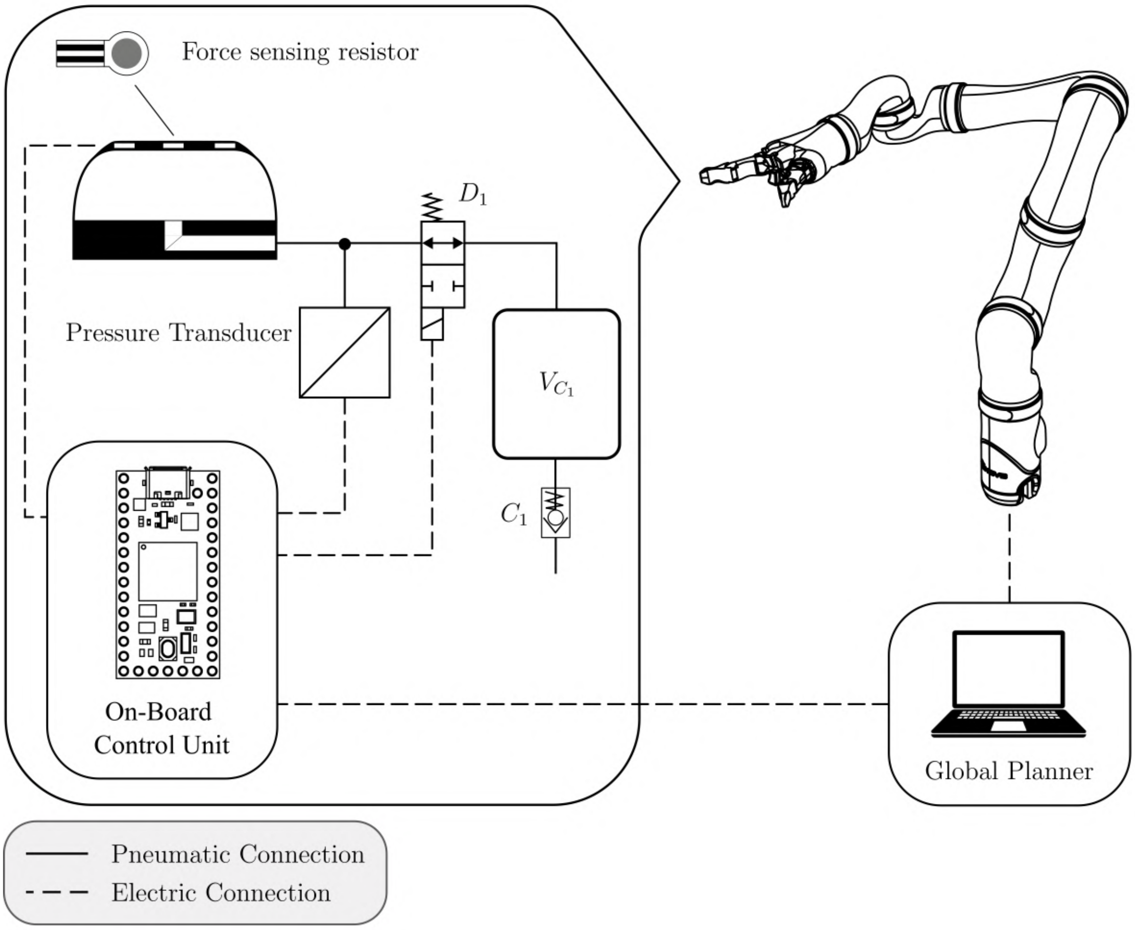

Figure 3.16: High-level architecture of PneuTact.Q mounted on the end-effector of the manipulator. Three force sensing resistors are placed in the middle of the upper wall of the membrane to provide indications on the contact area during gripping. A single auxiliary volume is used for each SPSC, meaning there is only one possible jump in stiffness.

The interposition of a compliant element between the object to be grasped and the rigid gripper finds its main utility in simplifying the grasping control, which from a force control becomes a position control [158]. Additional functionality relates to providing information about gripping operations, such as contact loss detection, stiffness identification, grasping force estimation and the object contouring [175].

Figure 3.16 schematises the architecture of the system, named PneuTact.Q, that implements the variable stiffness SPSCs on the distal links of a rigid commercial gripper[6].

According to the schematic, it is intended to allocate, on the manipulator's end effector, two SPSCs with an auxiliary pneumatic system, together with an electronic I/O management board. For the sake of simplicity, the schematic is devoid of secondary electronic elements, e.g. drivers, mosfets.

The choice of a single auxiliary volume for SPSC is motivated by the need for a small encumbrance and, in this context, the jump between only two levels of system stiffness is considered to be sufficient. The basic idea is, therefore, to employ a normally open $\boldsymbol{D}_1$ directional valve and, in the case of contact with a body classified as rigid, to switch $\boldsymbol{D}_1$ in order to exert greater contact forces. Conversely, $\boldsymbol{D}_1$ can be closed during the early stages of contact in order to assess the stiffness of the object with greater sensitivity on the part of the sensing unit and, in the case of a soft object, can be opened for a more delicate grip.

The local control unit, summarised in the figure by the symbol of a micro-controller, is responsible for collecting data from the SPSCs. In addition to the pressure information inside the chambers, three force sensing resistors (FSRs) are inserted inside the upper wall of the bladder. These sensors allow the contact force normal to them to be read, and are used here to provide an estimate of the distribution of contact forces across the membrane. Thus, the control unit collects, from the single sensing unit, a total of four measurements; and has as its only output signal the switching state of the on-off valve $\boldsymbol{D}_1$.
With regard to the fabrication of the SPSC, it is necessary here, in addition to what has already been discussed, to create a suitable housing for the three FSRs, as well as a suitable geometric coupling in order to rigidly fix the sensing unit to the gripper. Figure 3.17 shows a design solution that includes both features in a monolithic design. The housings of the force sensors are made by means of pockets, into which the FSRs are inserted post-fabrication of the SPSCs, and which protect the FSRs from damage due to direct contact with the bodies [176]. In view of the results discussed in sub-section 3.3.1, the fingertip chambers have a shape that can be traced back to Type A, due to the high contact area and higher sensitivity. The monolithic part also has a second chamber, with two associated FSRs. This distal chamber, which has a smaller volume than the fingertip chamber, is designed to provide information in the case of operations such as pressing keys, buttons or touching a surface. According to this design, the local control unit collects a total of seven measurements from the single SPSC. For the distal chamber, however, the jump between two stiffness levels is not of interest. Therefore, the only output signal remains the switching state of $\boldsymbol{D}_1$.

---

[6] In the specific case in the figure, this is the same Kinova Gen2 with KG2 gripper mentioned for the development of the BiSoft.Q gripper

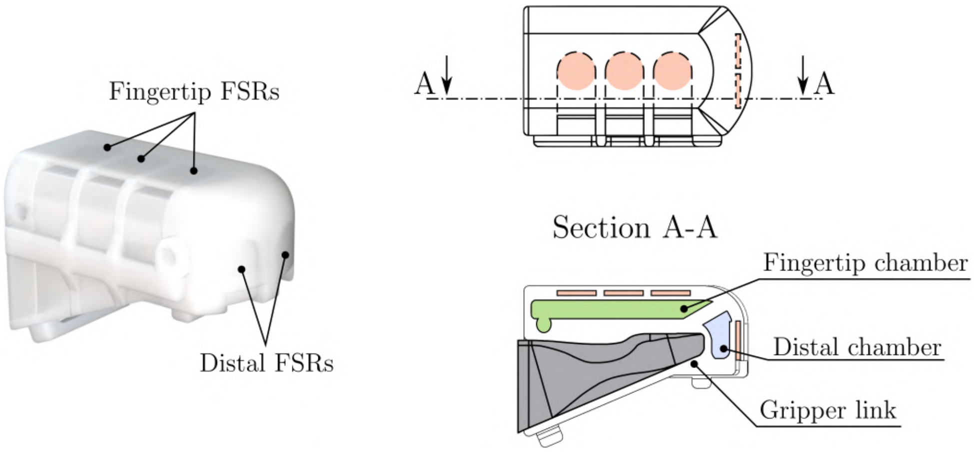

Figure 3.17: Representation of the sensing element that is mounted on the robotic gripper distal link. It has a monolithic design and includes the housing for the link insertion, two fingertip chambers and pockets for positioning the FSRs. The geometry of the fingertip chamber is Type A.

Figure 3.18 shows the prototype of the system mounted on the end effector of the manipulator. PneuTact.Q system is on-board except for two electrical cables, one power

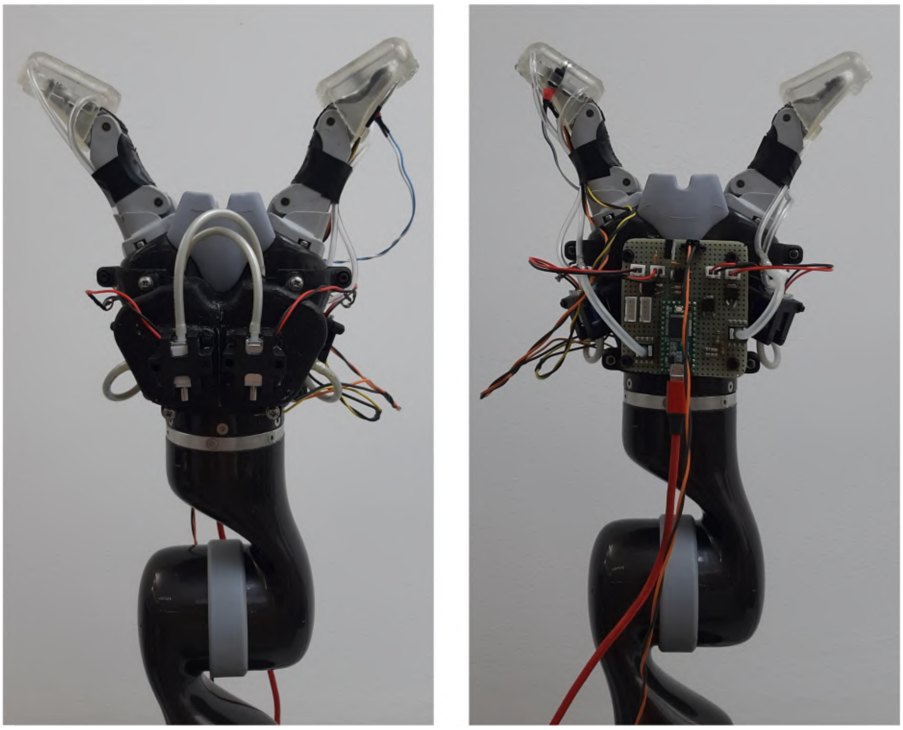

Figure 3.18: PneuTact.Q prototype mounted on the end-effector of a Kinova Gen2 manipulator. The prototype mass is 750 g, that is the 15% of the arm payload.

cable and a second data cable, which are directed to the external power supply and global planner respectively. The realisation of a wireless version is not excluded in further developments. In terms of payload subtracted from the manipulator, the prototype has a total mass of approximately 750 grams, which corresponds to 15 % of the manipulator payload. The FSRs have a circular active area with a diameter of 5.6 mm (model FSR05BE, by Ohmite), and a force range of up to 5 kg. The diameter of the FSRs determines the resolution achievable in terms of contact point reading, and it is planned to increase this functionality in the future using an FSR matrix (or similars). The pressure transducers used have a full-scale range of 100 kPa (gauge) and an accuracy of 0.25 % (model ELVH-015G-HAND-C-NAA5, by Amphenol All Sensors).

Given the geometric complexity of the SPSCs in monolithic design, they were fabricated using SLA in both Elastic 50A and silicon 40A, although the latter is to be preferred due to the higher reliability demonstrated in sub-section 3.3.2 tests.
Figure 3.19 shows an example of data collected using PneuTact.Q. The displacement of the contact point on finger 1, from the middle-rear to the front, is detected by the FSRs, whose measurements are displayed both in charts (top right) and through the opacity of the circles (top center), where higher opacity indicates a higher value. The squeezing level is also measured through pressure data, from which it is possible to observe that, in addition to shifting the contact point, the squeezing level of the SPSC is lower.
Figure 3.20 shows similar results but during the grasping of a rigid cylindrical object. In this case, the grasp is initially recognized as symmetric, with contact in the middle-front area of the SPSCs, but slippage is detected in (b) since the contact point shifted toward the tip and the pressure values are constantly decreasing.
Figure 3.21 instead shows the stiffness estimation functionality during the grasping of cylindrical objects with varying diameters. The detection of a grasp is recognized by setting threshold values on the pressure and its first derivative as a function of the closure angle $\alpha$, where $\alpha_c$ represents, for all grasps, the angle at which contact with the object occurs. For these tests, both directional valves $\boldsymbol{D}_1$ and $\boldsymbol{D}_2$ were open, i.e., both sensing units had low stiffness and low sensitivity. The light blue curve represents the grasp of an object considered infinitely rigid, while the cyan-green curve represents the grasp of a plastic bottle. Between these two extremes, it is possible to distinguish, after at least 10 deg of closure, the stiffness of three different types of objects. Note, in the case of the cyan-green and yellow curves, that it is possible to recognize a softening behavior due to the inward bending of the object's outer shell as it is being grasped.
Figure 3.22 shows how the data from Figure 3.21 can be used during the grasping of an object with unknown stiffness. In a potential real-time grasp control scenario, in the case of manipulating an object like the one in the figure, the directional valves $\boldsymbol{D}_1$ and $\boldsymbol{D}_2$ could be switched during the gripper's closure to ensure a more robust grasp.

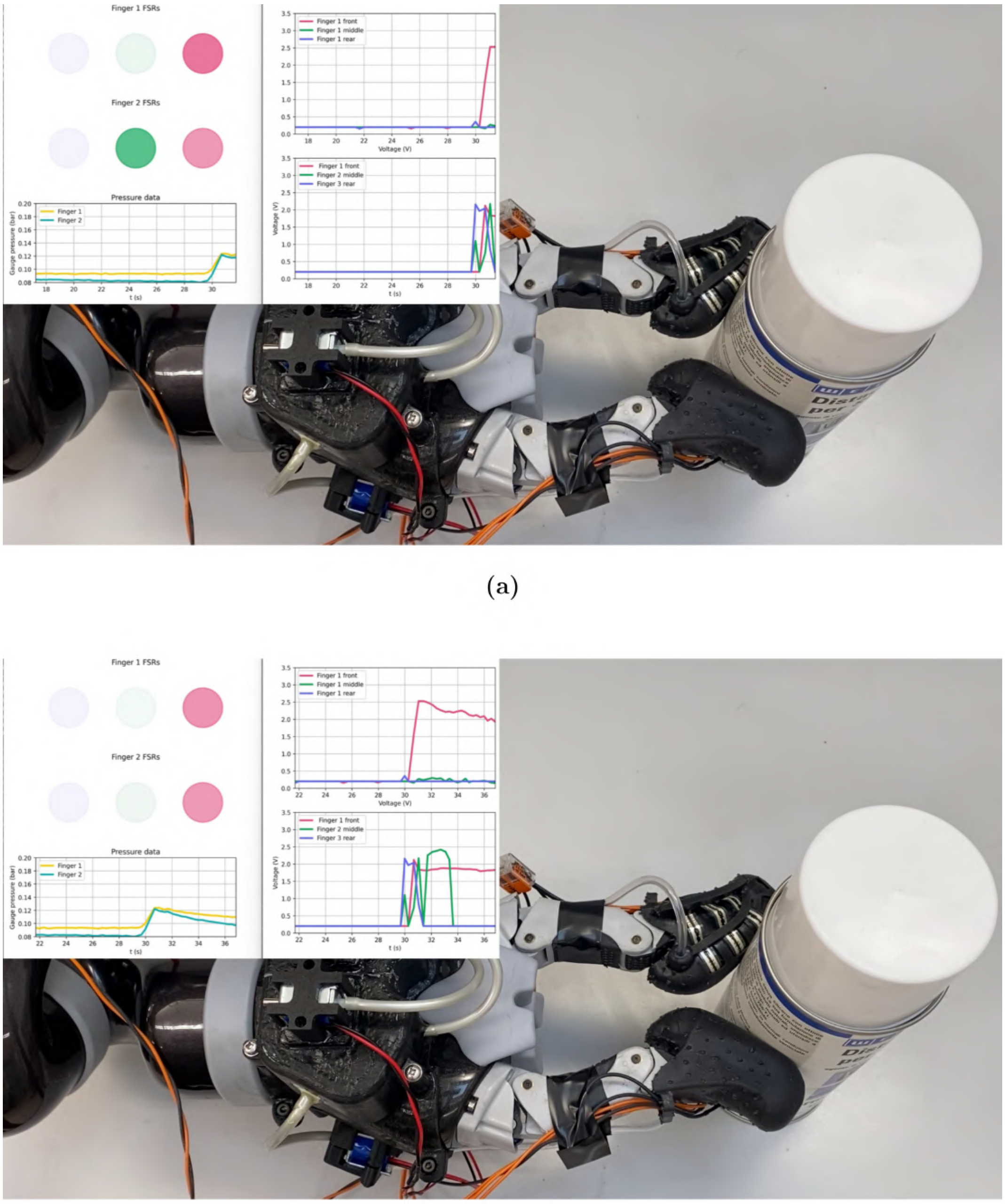

(a)

(b)

Figure 3.19: Data acquired from finger 1 of PneuTact.Q. $P(y_s = 0) = 10$ kPa. Data values from FSRs are represented by the opacity of the circles. Higher opacity indicates a higher value. Numerical values are also reported on the right.

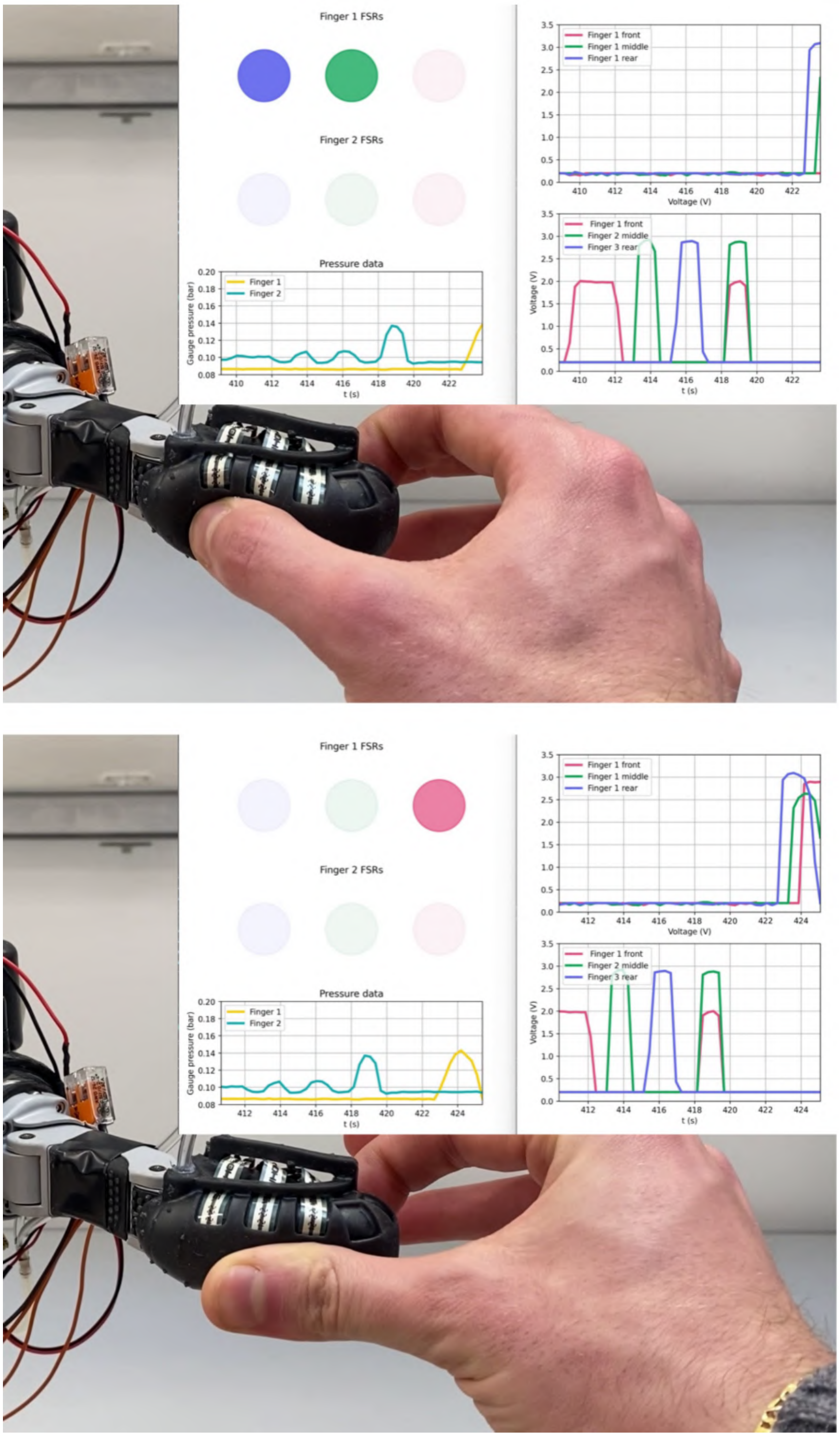

Figure 3.20: **(a)** Values measured when gripping a cylindrical rigid object. $P(y_s = 0) =$ 10 kPa. **(b)** Slippage detection observed due to the change in contact point and the decrease in internal chamber pressure.

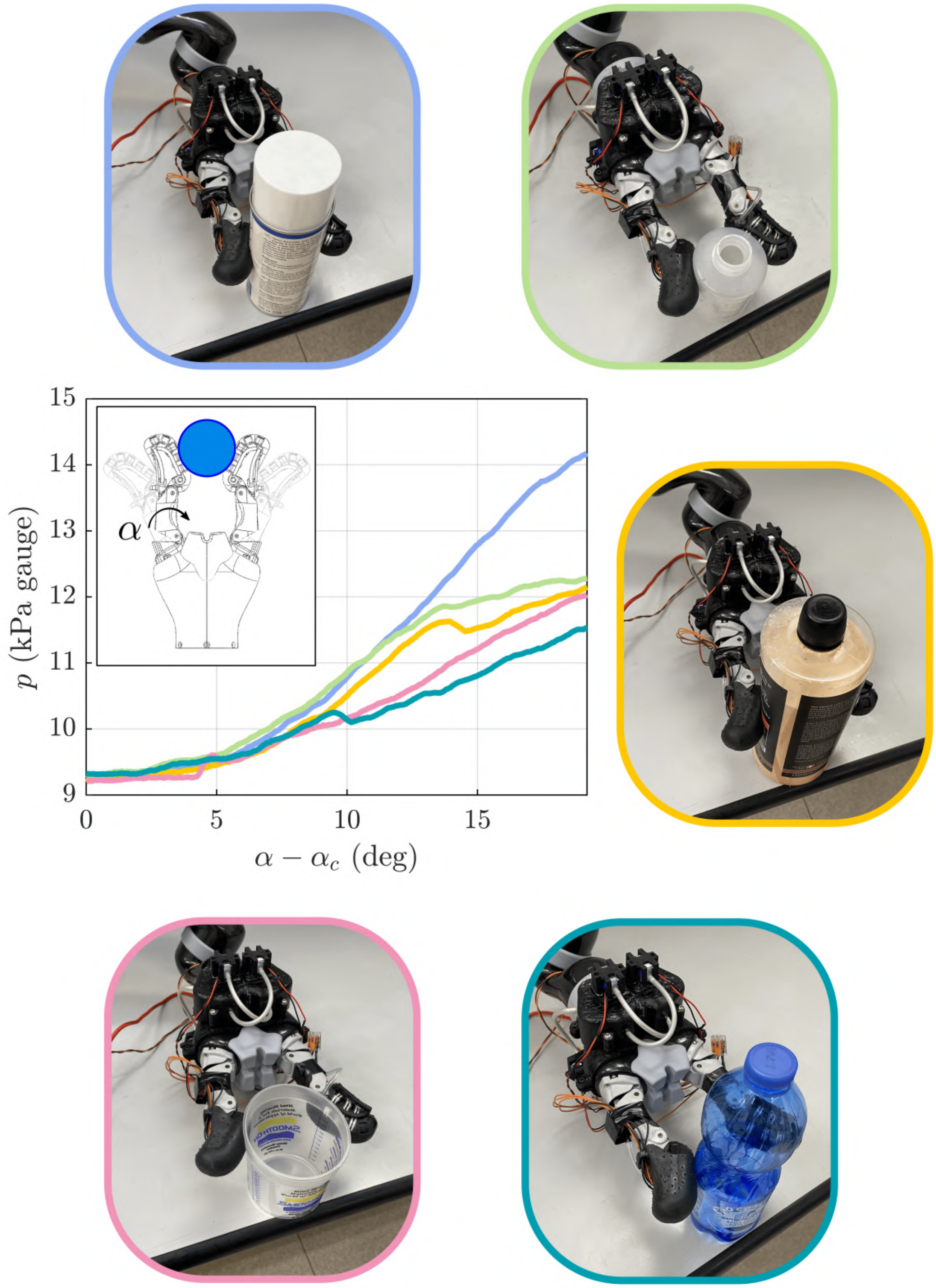

Figure 3.21: Pressure data are used for object stiffness evaluation. Thresholds on pressure values, supported by FSRs data, are used to detect contact ($\alpha_c$).

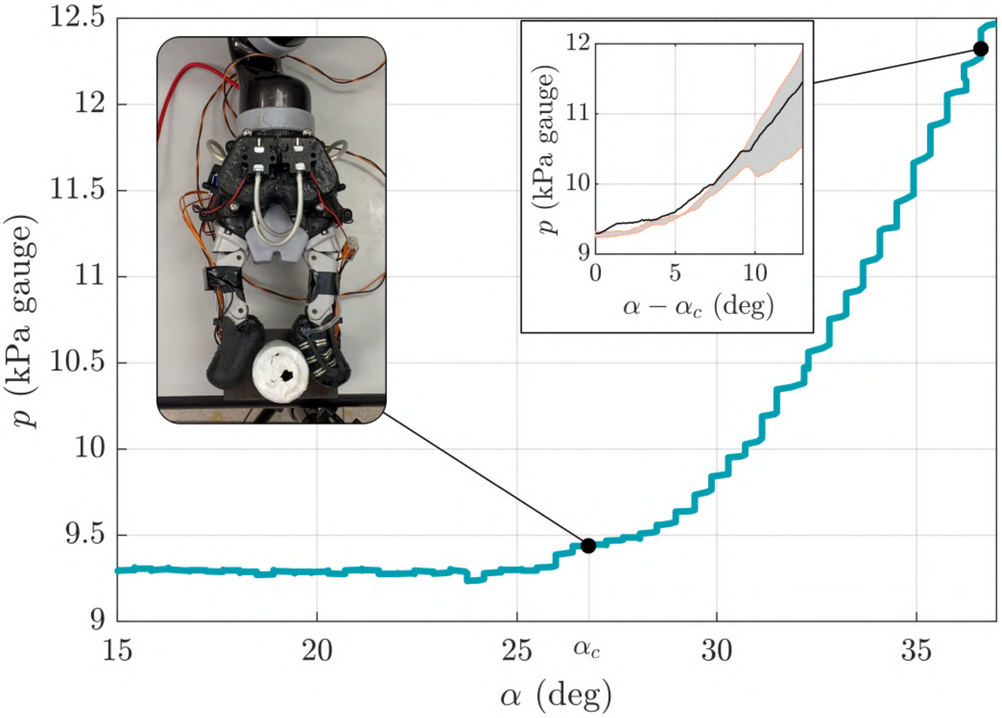

Figure 3.22: Object stiffness evaluation during graspig. In $\alpha_c$ the contact with the object is detected

### 3.4.2 Pneumatic handheld haptic device

Besides the use on robotic manipulators, this work also discusses the use of the SPSC system as a sensing unit for an untethered haptic device. This idea has led to the development of the PAL-HAND.Q haptic device, that has been subject of a national patent application by Colucci and Quaglia, n. 102024000002331 filed in february 2024. The PAL-HAND.Q concept and development has also been published by Duretto, Colucci, Jabbari and Quaglia in [167].

As shown in Figure 3.23, a haptic device is a human-machine interface capable of enabling bidirectional physical communication between a remote control unit and an end-user. The use of haptic devices is primarily employed for entertainment purposes [177, 178, 179], tele-operations [180, 181, 182, 183, 184, 185], or tele-rehabilitation [186, 187, 188, 189, 190], as it is well established that the repetitive and voluntary execution of hand opening/closing actions significantly helps in restoring motor functionality of the limb [191, 7] and also stimulates neurogenesis [8].

There are different types of haptic feedback, e.g., force feedback, mechanical vibration, heat, friction modulation, and the design of the device strongly depends on the intended application, as well as the part of the end-user's body with which the device interacts

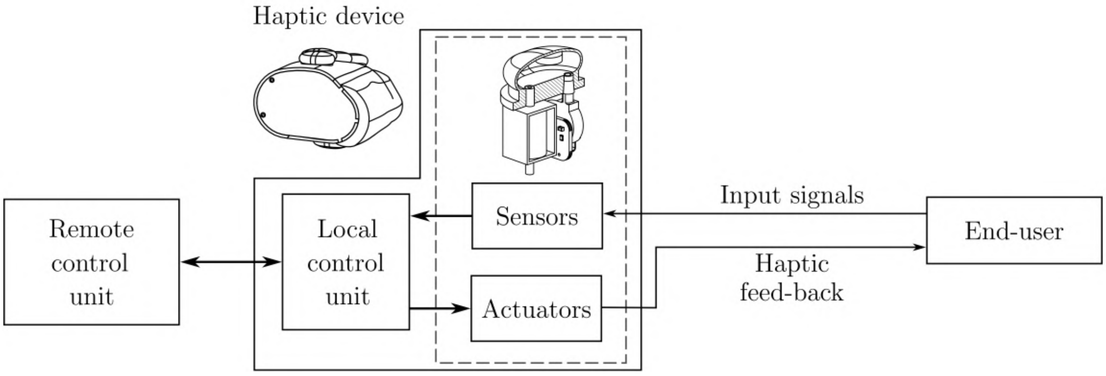

Figure 3.23: Schematic diagram of a generic haptic device. The interface element, in this case, are five SPSCs mounted on the hard cover of a handheld device.

[192].

Figure 3.24 depicts the basic design of a handheld device consisting of a rigid case, on which five SPSCs are positioned. The device is designed to be held in the user's hand, similar to commercial video game joysticks, as shown in the subsequent Figure 3.25. The five deformable membranes serve as the physical interface between the device and the user's five fingers. By pressing the membranes, the user can send a signal to the

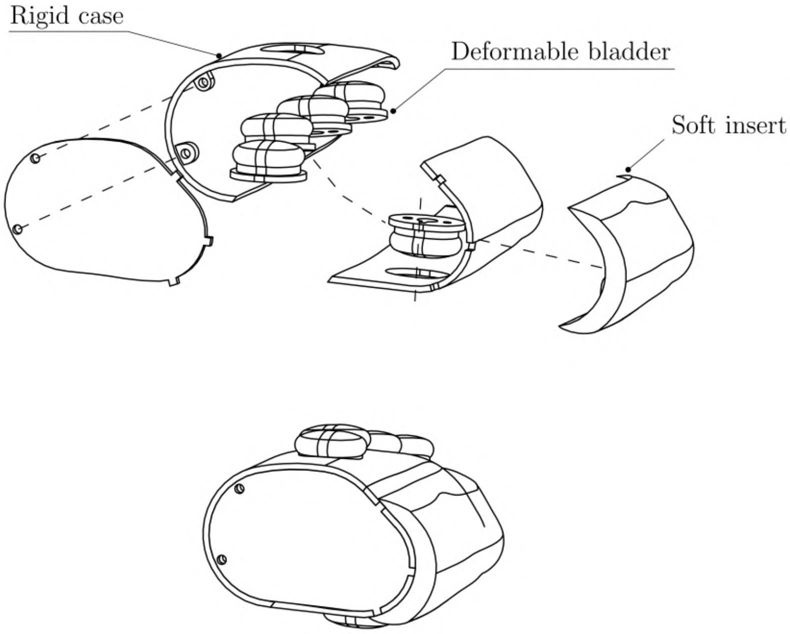

Figure 3.24: Exploded axonometric view of the haptic device under investigation.

remote control unit. The stiffness perceived by the user when pressing the membranes can be controlled similarly to what is described in previous sections.

Figure 3.26 shows the system architecture of the resulting device, that is named PAL-HAND.Q (Pneumatic and Lightweight Handheld Device). PAL-HAND.Q shares the design requirements of lightness and compactness with the previous technology for robotic grasping, which are essential here to allow the user to easily grasp and manipulate PAL-HAND.Q [193]. Therefore, in this case, the *m*-th membrane is connected to a single auxiliary volume, and there is only one possible jump between two stiffness levels, depending on the state of the on-off directional valve. To generate multimodal haptic feedback by combining different types of sensory feedback, a vibrating mini-motor (Linear Resonant Actuator, LRA) is mounted inside the SPSC chamber. This feature allows the user to perceive not only a variable stiffness of the SPSC, but also a localised vibratory feedback on the phalanx in contact with the SPSC. The scientific literature on the development of wearable or handheld haptic systems interacting with the user's

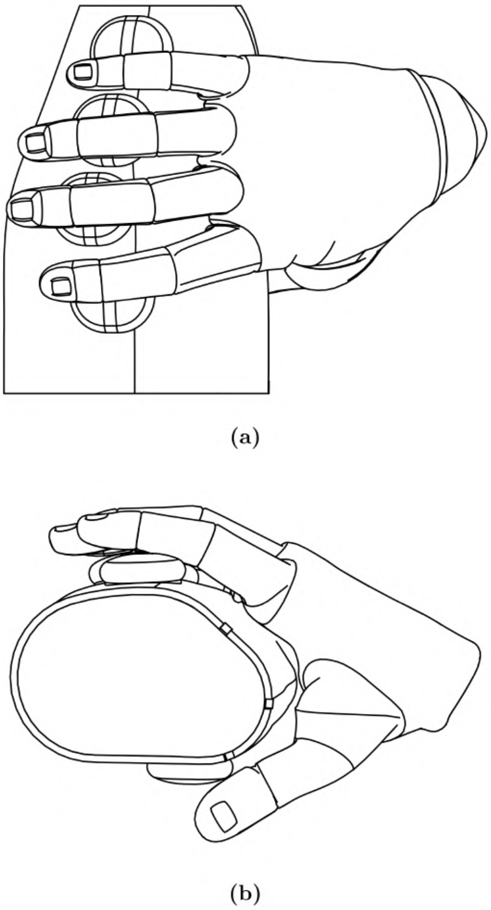
(a)

(b)

Figure 3.25: PAL-HAND.Q grasped by the hand of an end-user. **(a)** Top view. **(b)** Front view.

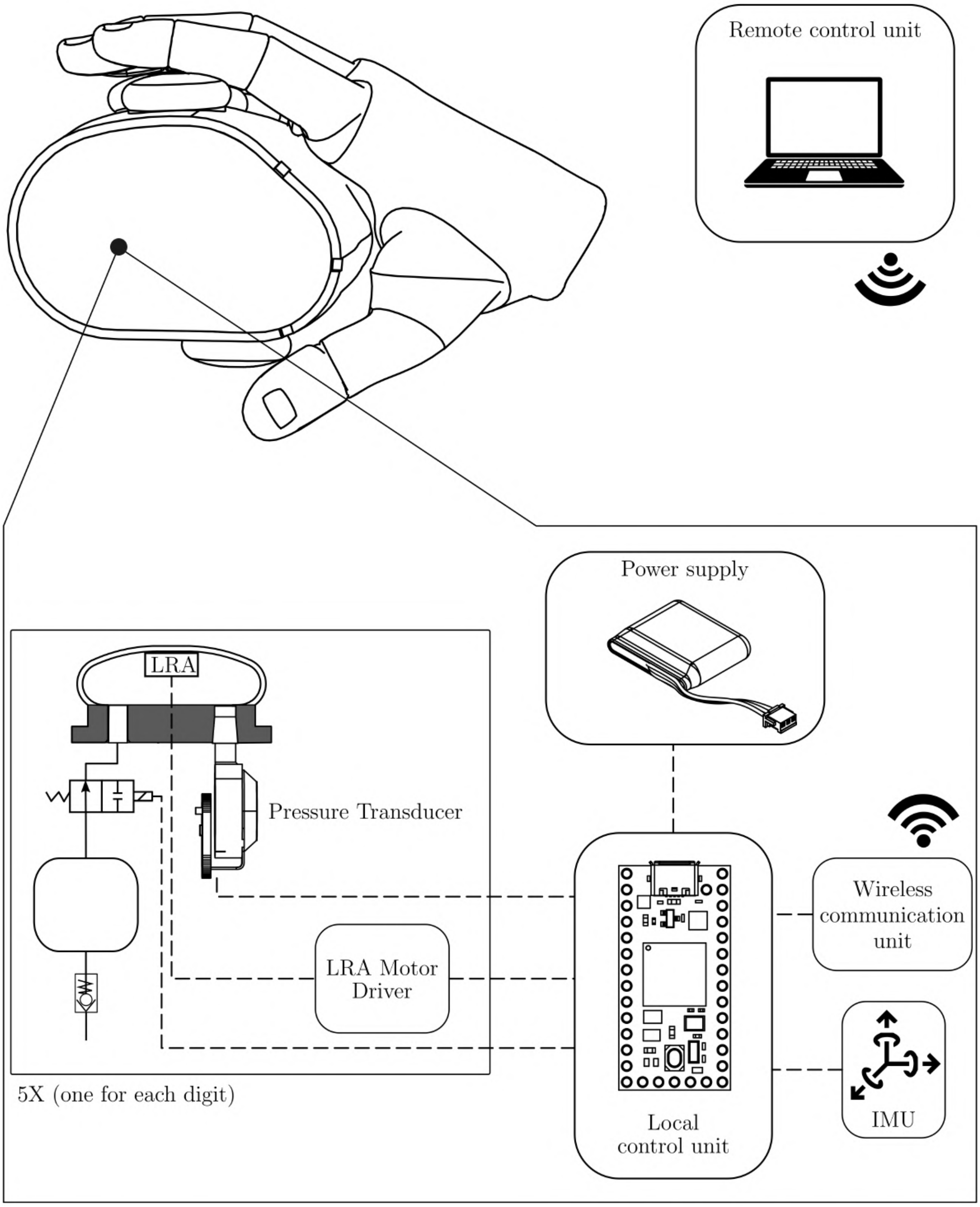

Figure 3.26: The PAL-HAND.Q system architecture. All the cited components are allocated within the rigid case.

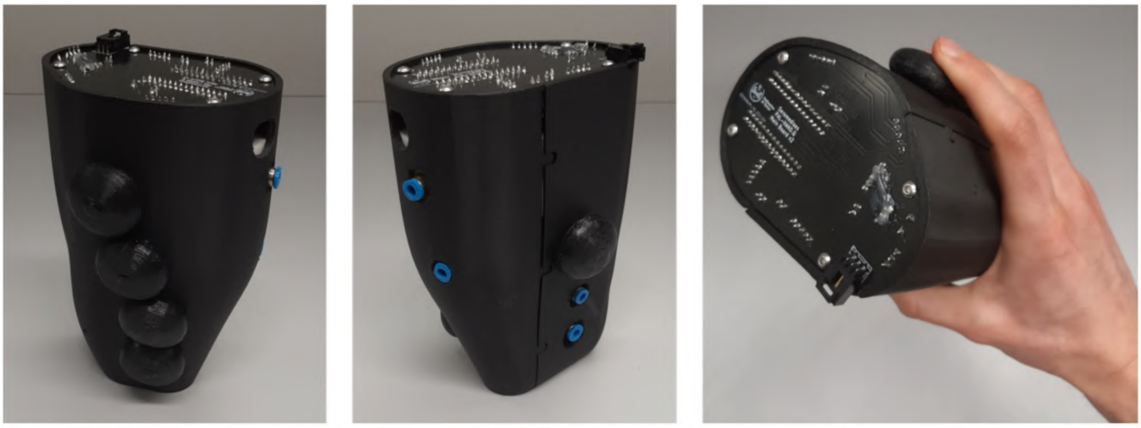

Figure 3.27: The PAL-HAND.Q prototype.

hand also suggests making the device wireless to increase its portability and ease of use [193]. This requirement is met here by integrating a power supply unit and a wireless communication unit into the system. An inertial measurement unit (IMU) completes the design, allowing for membrane squeezing tracking and hand motion tracking.

Figure 3.27 shows the prototype of PAL-HAND.Q. According to this design, all necessary spaces for the elements shown in Figure 3.26 are allocated within the case, which essentially fills the volume inside the user's hand. At the top of the device is the printed circuit board (PCB), which manages power supply, I/O signals, and wireless communication. The microcontroller used is the Arduino Nano 33 BLE, which integrates the 9-axis IMU LSM9DS1 and a Bluetooth Low Energy (BLE) module for wireless communication. The five check valves, whose blue push-in connectors are visible, are accessible from the outside without the need to open the device. For positioning the LRAs inside the SPSCs, these were made using FDM with TPU 60A. Once printed, a partial cut was made at the base of the membranes to insert the vibrating mini-motors. The cut was then repaired by applying melted rubber using an electronics soldering iron. The pressure sensors used are the same as those in the previous subsection, while the vibrating mini-motors are DFRobot FIT0774.

Similar commercial systems, whether handheld or wearable, provide force feedback, also known as kinesthetic feedback, to the user's fingers using electrical actuation [194], cables [189], or fluids [188, 187]. The use of active systems to control kinesthetic feedback certainly improves the functionality of the device, but it also increases its size and weight, making it impossible to create a completely wireless device that fits completely in the hand. The PAL-HAND.Q model represents a compromise between two design requirements: lightness and practicality on the one hand, and extensive functionality on the other.

Figure 3.28 shows an example of data collected by the remote control unit from PAL-HAND.Q. In the top left, the pressure measurements are shown, in this case for only three membranes. These measurements can be used to recognize, for instance,

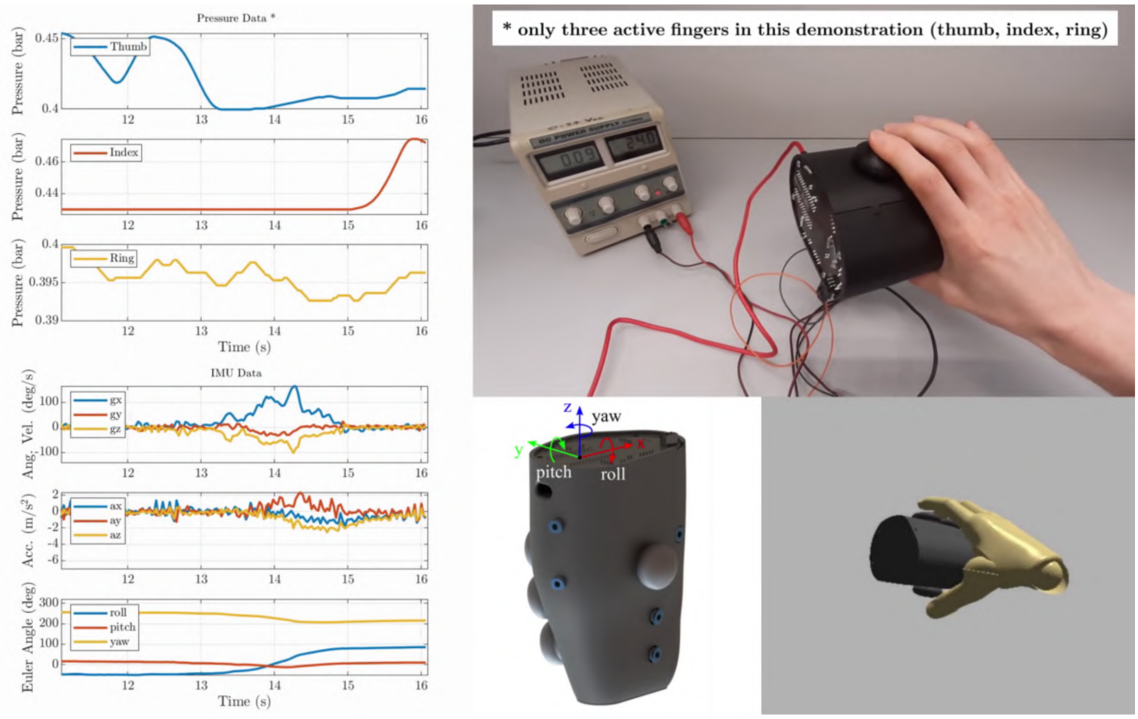

Figure 3.28: Example of data collected from PAL-HAND.Q. In the top left, internal pressure data in the SPSCs. In the bottom left, data from the 9-axis IMU. In the bottom right, representation of the user's hand and PAL-HAND.Q in the graphical interface on the remote control unit.

Table 3.4: PAL-HAND.Q technical specifications.

| Name | Value |
|---:|:---:|
| Encumbrance (mm) | 160 x 120 x 100 |
| Mass (with and without battery) (g) | 300-500 |
| Membrane deformation stroke (mm) | 10 |
| Set-up pressure $p_i$ (kPa gauge) | 20-50 |
| Autonomy (min) | $\approx 30$ |

the compression of the thumb membrane at t=12.5 s and the compression of the index membrane at t=16 s. The raw angular and linear acceleration data from the 9-axis IMU are post-processed to measure the position and orientation of the hand[7]. In the bottom right, a screenshot of a graphical interface, developed in Python, is shown, rendering

---

[7] A Madgwick filter was used for the angular acceleration data.

the real-time movement of the user's hand and fingers[8]. The data were collected here by connecting the microcontroller to the remote control unit's serial port, allowing for a higher data write frequency. With wireless connection, the upper limit for the sampling frequency is approximately $\approx 30$ Hz.

Table 3.4 reports the technical specifications of PAL-HAND.Q. The intended applications for the haptic device presented here mainly concern active hand telerehabilitation, the development of alternative forms of communication, and inclusive video games. The implementation of the device in these contexts, as well as the development of dedicated software, however, are not covered in this thesis.

---

[8] Developed using PyGame and ModernGL

# Chapter 4

# Conclusion and further research

Pneumatics applied to Service Robotics is an active and extremely fascinating area of research. Chapter 1 provided an overview, describing how requirements and paradigms have changed over the last two decades, and the latest methods and materials for manufacturing soft pneumatic robots.

### The BiSoft.Q actuator

Chapter 2 presented a novel soft pneumatic actuator that utilizes the principle of antagonistic chambers to achieve a bi-directional linear behavior. The use of additive manufacturing techniques makes the actuator lightweight, cost-effective, and easily reproducible. Two types of BiSoft.Q have been identified based on the internal arrangement of the membranes.

The BiSoft.Q design methodology is based on a simplified analytical model for calculating the actuator's performance under quasi-static conditions. This translates to the estimation of stroke, forces (both push and pull), and air consumption in the case of simple actuation or in case of more sophisticated energy-saving strategies. This method showed a good correspondence with experimental results obtained through isometric tests under nominal operating conditions. In the case of excessively high supply pressures, the assumption of inextensibility of the longitudinal fibers of the pleated membrane is no longer valid, and the actuator undergoes additional deformation due to the elastic deformation of the fibers. This also limits the actuator's energy work density. Further research may be conducted to improve the design shown in Figure 2.9 to strengthen the structure of the two membranes.

When compared to the elementary case of a bellows and a pleated actuator placed in parallel, the BiSoft.Q presents greater construction challenges but yields better results in the static apply graph. This is mainly due to better optimization of the available space. Compared to mono-directional PPAMs, the BiSoft.Q sacrifices some strain rate for its bi-directionality but retains the advantages of pleated geometries, such as negligible energy losses and low supply pressure thresholds. In terms of energy consumption, the

BiSoft.Q's air demand is strongly influenced by the dead volumes in the two chambers. The use of energy-saving methods has shown significant potential for improvement. Future development thus concerns the executive design of a version of the actuator with an integrated energy-saving system, followed by experimental validation.

The anticipated applications for this technology mainly target the field of assistive robotics, where soft actuators are widely employed. The gripper presented, actuated by a BiSoft.Q Type A, has proven to be an interesting solution due to its reduced mass and versatility in grasping objects of various shapes. Further applications may include the use of the BiSoft.Q in exoskeletal systems, where joint actuation is often achieved through multiple soft linear actuators positioned in an antagonistic configuration.

### PneuTact.Q and PAL-HAND.Q

Chapter 3 discussed the development of a pneumatic sensing unit applied to robotic manipulation for tactile sensing and to haptic systems for human interaction and finger active tele-rehabilitation. The single deformable pressurized chamber was described through a geometric model that allows the creation of membranes with different shapes. This results in varying sensitivity and stiffness in the experimental characterization phase, which were analyzed to provide guidelines for selecting the appropriate geometry based on design requirements. The initial setup parameters, i.e. pressure and volume in the auxiliary chambers, also allow control over the static performance of the sensing unit. Further research could explore modifications to enable continuous stiffness control, e.g., through real-time adjustments of the auxiliary volume.

The prototyping phase involved fabricating the membranes using additive manufacturing techniques and silicone molding. The reliability of the membranes was quantified through destructive fatigue tests and puncture tests.

This concept was first applied to develop a tactile sensing unit for robotic grippers. PneuTact.Q demonstrated various functionalities, including object estimation, grip force measurement and slippage detection. The system's current limitations lie in the resolution of contact force data obtained from the FSR sensors positioned on the membrane. Further work can be done to improve this resolution, such as implementing an FSR matrix to assess potential contact on the membrane's sides.

Another application involved using the sensing unit to develop a graspable and untethered haptic device for interaction with a human user's hand. The sensing unit allows measurement of finger motion and provides kinesthetic feedback, i.e., force feedback, by modifying the stiffness of the membranes. The main application for PAL-HAND.Q is post-stroke active rehabilitation of patients with finger impairments, promoting functional recovery and neurogenesis. Future development of the device should focus on a comfort study for designing an ergonomic case, the creation of rehabilitation exercises using the device, and software development for an interface enabling exercises in virtual or augmented reality environments.

# Appendix A

# BiSoft.Q geometry details

This appendix describes the methodology for deriving the nominal and undeformed BiSoft.Q geometry from the parameters outlined in Table 2.1. All the equations are referred to the $x = 0$ configuration, although this notation is omitted for brevity. For similar reasons, the subscript $[\,]_{[\,],p}$ will be omitted, while $[\,]_{[\,],b}$ will be used to refer to the bellows geometry.
The geometrical definition of the BiSoft.Q pleated membrane starts from the terminal cross-section B-B in Figure A.1. Among this plane, the only unknown value is $R_{oe}$, which can be derived by considering the longitudinal crest fibre geometry as:

$$R_{oe} = R_{om} - l_c \left( \frac{1 - \cos(\varphi_c)}{2\,\varphi_c} \right) \tag{A.1}$$

where the outer radius $R_{om}$ in the middle cross-sectional plane depends on the $R_{im}/R_{om}$ ratio and $R_{im}$ is equal to:

$$R_{im} = R_{ie} + l_v \left( \frac{1 - \cos(\varphi_v)}{2\,\varphi_v} \right) \tag{A.2}$$

The two angles $\varphi_{[c,v],p}$, respectively referred to the crest and valley fibres can be numerically derived from the following equation:

$$\frac{\sin(\varphi_{[c,v]})}{\varphi_{[c,v]}} = \frac{L}{l_{[c,v]}} \tag{A.3}$$

Hence, basing on the geometrical construction in Figure A.2 (a), the coordinates of the two tangency points $S_{ce}$ and $S_{ve}$ are respectively:

$$\mathbf{O'S_{ce}} = \begin{bmatrix} R_{ce}\,\cos(\varepsilon) \\ R_{oe} + R_{ce}\,(\sin(\varepsilon) - 1) \end{bmatrix} \tag{A.4}$$

$$\mathbf{O'S_{ve}} = \begin{bmatrix} (R_{ie} + R_{ve})\,\sin(\alpha_p/2) - R_{ve}\,\cos(\varepsilon) \\ (R_{ie} + R_{ve})\,\cos(\alpha_p/2) - R_{ve}\,\sin(\varepsilon) \end{bmatrix} \tag{A.5}$$

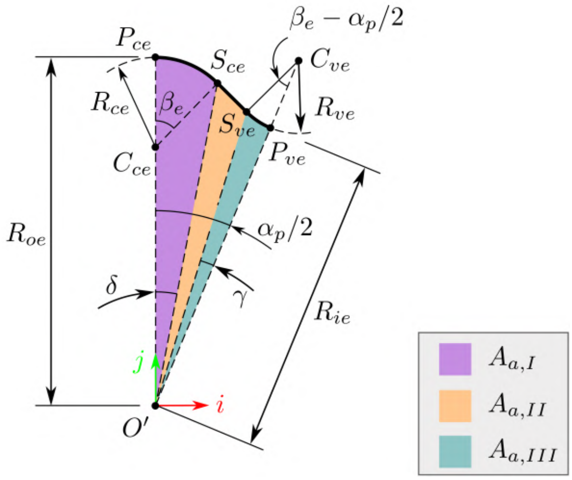

Figure A.1: Pleated geometry representation in the terminal cross-sectional plane. $A_{a,[]}$ is the antagonistic area which causes a decrease in actuator pull forces.

where the auxiliary angle $\varepsilon$ can be derived from Figure A.2 (a) as:

$$\varepsilon = \frac{\pi}{2} - \sin^{-1}\left(\frac{HC_{ve}}{C_{ce}C_{ve}}\right) - \tan^{-1}\left(\frac{BC_{ve}}{BC_{ce}}\right) \tag{A.6}$$

$$C_{ce}C_{ve} = \sqrt{BC_{ve}^2 + BC_{ce}^2} \tag{A.7}$$

$$HC_{ve} = R_{ce} + R_{ve} \tag{A.8}$$

The remaining two auxiliary angles $\delta$ and $\gamma$ can be obtained from the two geometrical construction in Figure A.2 (b) and (c) by means of the sine formula for the two $O'C_{ce}S_{ce}$ and $O'S_{ve}C_{ve}$ triangles:

$$\delta = \tan^{-1}\left(\frac{\sin(\beta_e)}{\frac{R_{oe}}{R_{ce}} + \cos(\beta_e) - 1}\right) \tag{A.9}$$

$$\gamma = \tan^{-1}\left(\frac{\sin(\beta_e - \alpha_p/2)}{\frac{R_{ie}}{R_{ve}} + \cos(\beta_e - \alpha_p/2) - 1}\right) \tag{A.10}$$

where

$$\beta_e = \pi - \tan^{-1}\left(\frac{y_{S_{ce}} - y_{S_{ve}}}{x_{S_{ce}} - x_{S_{ve}}}\right) \tag{A.11}$$

The geometry thus defined in the terminal cross-sectional plane is extruded along

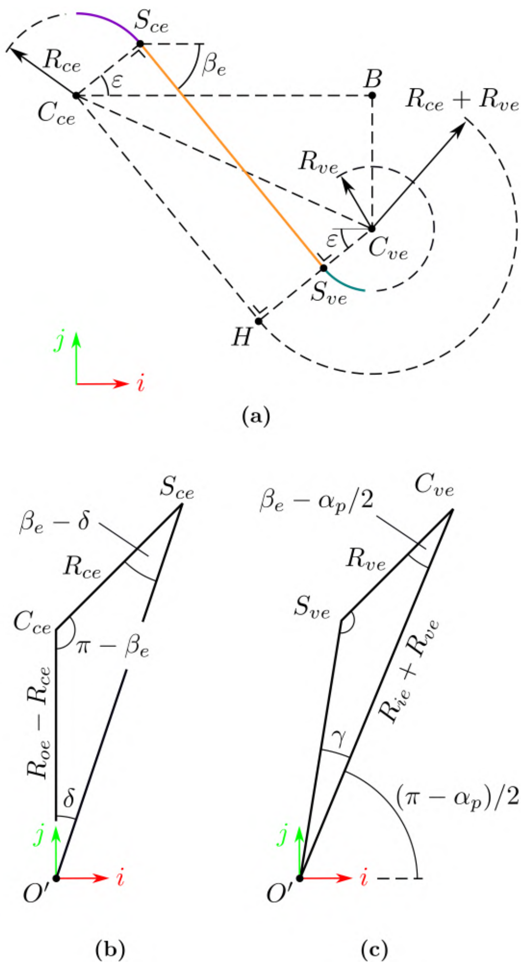

Figure A.2: **(a)** Geometric construction to derive $S_{ce}$ and $S_{ve}$ points. **(b)** Computation of $\delta$ angle, **(c)** computation of $\gamma$ angle.

$\hat{k}$ direction following the longitudinal crest and valley primitive arcs depicted in Figure 2.1 (a). To derive $R_{om}$ and $R_{im}$, let consider the two arc angles $\varphi_{[c,v]}$, respectively referred to the crest and valley fibre and defined in Figure 2.3 (a) and Figure 2.2. The two values can be linked to $L$ and $l_{[c,v]}$ by means of the following equation:

$$\frac{\sin(\varphi_{[c,v]})}{\varphi_{[c,v]}} = \frac{L}{l_{[c,v]}} \tag{A.12}$$

that does not have an analytical solution but can be numerically solved. Thus, $R_{[o,i]m}$ can be computed as:

$$R_{[o,i]m} = R_{[o,i]e} + \frac{l_{[c,v]}}{2\,\varphi_{[c,v]}}\,(1-\cos(\varphi_{[c,v]})) \tag{A.13}$$

To derive the two remaining terms $R_{[c,v]m}$, namely the radii of arcs I and II in the cross-sectional median section, it is here assumed $\delta$ and $\gamma$ remain constant moving from plane B-B to A-A in Figure 2.2. They are, therefore, calculated in a similar manner to that described above.

Let now consider the bellows geometry, reintroducing the notation $[\,]_{[\,],b}$ to refer to a bellows geometric quantity. Referring to Figure A.3, the half-height $h_b$ and the length of segment $A_bB_b$ can be easily obtained:

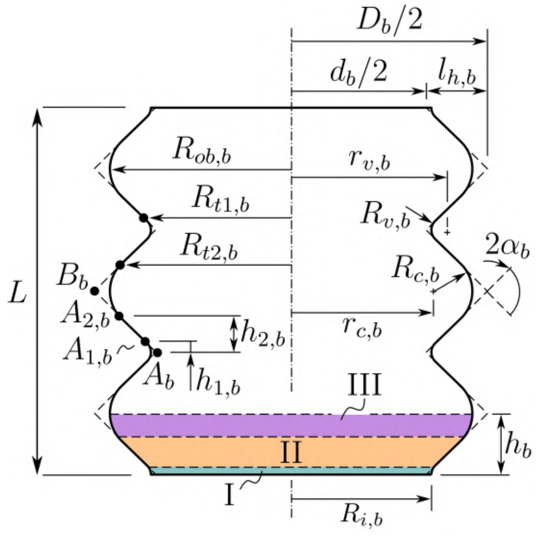

Figure A.3: Bellows primitive geometry representation.

$$h_b = \frac{L}{2N_b} \tag{A.14}$$

$$A_bB_b = \frac{l_{h,b}}{\cos\alpha_b} \tag{A.15}$$

$$l_{h,b} = \frac{h_b}{\tan\alpha_b} \tag{A.16}$$

where it was implicitly assumed that the bellows has the same height $L$ as the pleated geometry. Lastly, the lengths $r_{[c,v],b}$ are:

$$r_{v,b} = R_{i,b} + R_{v,b} \tag{A.17}$$

$$r_{c,b} = \frac{D_b}{2} - \frac{R_{c,b}}{\sin\alpha_b} \tag{A.18}$$

with:

$$D_b = d_b + 2l_{h,b} \tag{A.19}$$

$$d_b = 2\left(R_{i,b} - R_{v,b}\left(\frac{1-\sin\alpha_b}{\sin\alpha_b}\right)\right) \tag{A.20}$$

## A.1 Membrane analytical definition

This section describes the analytical definition of both the BiSoft.Q membrane in a generic configuration $x_{\min} \leq x \leq x_{\max}$. In a similar manner to the previous Appendix, the subscript $[\,]_{[\,],p}$ is omitted for brevity, while $[\,]_{[\,],b}$ is used to refer to the bellows. The pleated membrane geometry in its generic configuration can be estimated by imposing the translation of $P_{ce,p}$ along $\hat{k}$ of a value $x$, as depicted in Figure 2.3 (a). For the adopted fibre in-extensibility assumption, the angles $\varphi_{[c,v]}(x)$ can be expressed by introducing $x$ in Equation A.12:

$$\frac{\sin(\varphi_{[c,v]})}{\varphi_{[c,v]}} = \frac{L+x}{l_{[c,v]}} \tag{A.21}$$

which leads, in particular, to the computation of the crest arc radius $r_c(x)$ and the position of its centre $OC_c = OC_c(x)$, both shown in Figure A.4:

$$r_{[c,v]} = \frac{l_{[c,v]}}{2\,\varphi_{[c,v]}(x)} \tag{A.22}$$

Let now introduce the two polar coordinates $(\vartheta_1, \vartheta_2)$, respectively the latitude and longitude, displayed in Figure 2.4 (a). The following equation holds for the analytical definition of the longitudinal crest fibre $OW(0, \vartheta_2, x) = R(\vartheta_2, x)$:

$$R(\vartheta_2, x) = Y_{C_c}\cos(\vartheta_2) + \sqrt{r_c^2 - Y_{C_c}^2 \sin^2(\vartheta_2)} \tag{A.23}$$

where $Y_{C_c}$ is the coordinate of $C_c$ along $\hat{j}$. The generic outer radius $R_o(\vartheta_2, x)$ can now be written as:

$$R_o(\vartheta_2, x) = R(\vartheta_2, x)\cos(\vartheta_2) \tag{A.24}$$

Before deriving the explicit surface formulation $\underline{\Sigma}(\vartheta_1, \vartheta_2, x)$ as defined in Equation 2.3, let introduce the following auxiliary values:

$$A(\vartheta_2) = \frac{R_o}{R_c} \quad , \quad B(\vartheta_2) = \frac{R_i}{R_v} \quad , \quad C(\vartheta_2) = \frac{R_c}{R_v} \tag{A.25}$$

that can be reformulated as follows:

$$A(\vartheta_2) = 1 + \frac{\sin(\beta(\vartheta_2))}{\tan(\delta)} - \cos(\beta(\vartheta_2)) \tag{A.26}$$

$$B(\vartheta_2) = \frac{\sin(\beta(\vartheta_2) - \alpha/2)}{\tan(\gamma)} + \cos(\beta(\vartheta_2) - \alpha/2) - 1 \tag{A.27}$$

$$C(\vartheta_2) = \frac{1 - (B(\vartheta_2) + 1)\cos(\beta(\vartheta_2) - \alpha/2)}{(1 - A(\vartheta_2))\cos(\beta(\vartheta_2)) - 1} \tag{A.28}$$

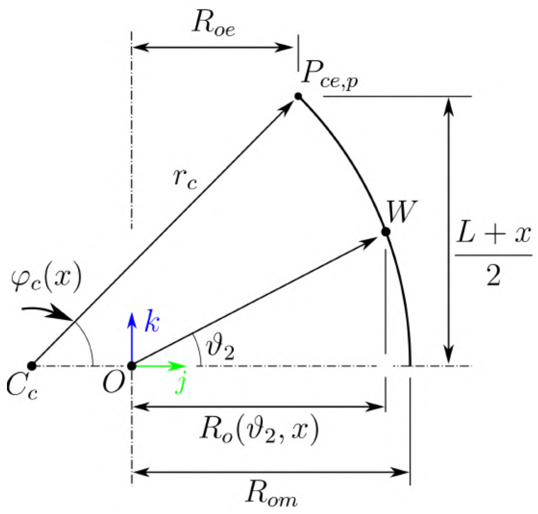

Figure A.4: Geometrical construction to derive the crest arc radius $r_c(x)$ and point $OC_c$.

where $\beta(\vartheta_2)$ is the inclination angle of segment II in the generic cross-section, and it can be derived in a similar manner to what described in Appendix A.
The pleated geometry can hence be defined within the range:

$$\begin{aligned} 0 &\leq \vartheta_1 \leq \alpha_p/2 \\ -\vartheta_{2,\max} &\leq \vartheta_2 \leq \vartheta_{2,\max} \\ x_{\min} &\leq x \leq x_{\max} \end{aligned}$$

and $\vartheta_{2,\max}$ defines the latitude of point $P_{ce,p}$:

$$\vartheta_{2,\max}(x) = \tan^{-1}\left(\frac{L+x}{2\,R_{oe}}\right) \tag{A.29}$$

Let consider the generic cross-section. As regards to the first segment I, it is described as an arc with a radius of $R_c(\vartheta_2, x)$ and centred in $(0, R_o - R_c)$:

$$\rho(\vartheta_1, \vartheta_2, x)_I = (R_o - R_c)\cos(\vartheta_1) + \sqrt{R_c^2 - (R_o - R_c)^2 \sin^2(\vartheta_1)} \tag{A.30}$$

and $R_c$ for the generic section can be derived from Equation A.25. Equation A.30 can also be reformulated by introducing the term $A$:

$$R_o - R_c = R_c\left(\frac{R_o}{R_c} - 1\right) = R_c\,(A-1) \tag{A.31}$$

thus leading to the following result:

$$\rho(\vartheta_1, \vartheta_2, x)_I = R_c(\vartheta_2, x)\Big(\big(A(\vartheta_2) - 1\big)\cos(\vartheta_1) + \sqrt{1 - \big(A(\vartheta_2) - 1\big)^2 \sin^2(\vartheta_1)}\,\Big) \tag{A.32}$$

for:

$$0 \leq \vartheta_1 \leq \delta \tag{A.33}$$

On other hand, the second portion II is a straight segment, whose slope is equal to $-\tan(\beta)$ and its intercept $q$ results to be equal to:

$$q = \frac{R_c + (R_o - R_c)\cos(\beta)}{\cos(\beta)} \tag{A.34}$$

and:

$$\begin{aligned}\rho(\vartheta_1, \vartheta_2, x)_{II} =& \frac{R_c(\vartheta_2, x) + (R_o - R_c)\cos(\beta)}{\cos(\vartheta_1 - \beta)} = \\ =& R_c(\vartheta_2, x)\left(\frac{1 + \left(A(\vartheta_2) - 1\right)\cos(\beta)}{\cos(\vartheta_1 - \beta)}\right)\end{aligned} \tag{A.35}$$

for:

$$\delta \leq \vartheta_1 \leq (\alpha_p/2) - \gamma \tag{A.36}$$

Lastly, the latter portion III can be derived in a similar manner to what shown for portion I, now considering an arc centred in $(R_i + Rv)(\sin(\alpha_p/2), \cos(\alpha_p/2))$ and with a radius of $R_v(\vartheta_2, x)$:

$$\rho(\vartheta_1, \vartheta_2, x)_{III} = (R_i + Rv)\cos(\vartheta_1 - \alpha_p/2) - \sqrt{R_v^2 - (R_i + Rv)^2 \sin^2(\vartheta_1 - \alpha_p/2)} \tag{A.37}$$

that can be reformulated by introducing $B$ and $C$:

$$R_i + Rv = R_v\left(\frac{R_i}{R_v} + 1\right) = R_v\,(B + 1) = \frac{R_c}{C}\,(B + 1) \tag{A.38}$$

which results in the following equation:

$$\begin{aligned}\rho(\vartheta_1, \vartheta_2, x)_{III} =& \frac{R_c(\vartheta_2)}{C(\vartheta_2)}\left(\left(B(\vartheta_2) + 1\right)\cos\left(\vartheta_1 - \frac{\alpha_p}{2}\right) + \right. \\ & \left. - \sqrt{1 - \left(B(\vartheta_2) + 1\right)^2 \sin^2\left(\vartheta_1 - \frac{\alpha_p}{2}\right)}\,\right)\end{aligned} \tag{A.39}$$

for:

$$\alpha_p/2 - \gamma \leq \vartheta_1 \leq \alpha_p/2 \tag{A.40}$$

Therefore, $\mathbf{OW}' = \rho$ can be defined piecewise and $\mathbf{OW}$ can be calculated according to Equation 2.3:

$$\mathbf{OW}' = \begin{bmatrix} X \\ Y \end{bmatrix} = \begin{cases} \rho_I & 0 \leq \vartheta_1 \leq \delta \\ \rho_{II} & \delta \leq \vartheta_1 \leq \alpha_p/2 - \gamma \\ \rho_{II} & \alpha_p/2 - \gamma \leq \vartheta_1 \leq \alpha_p/2 \end{cases} \tag{A.41}$$

$$\mathbf{\Sigma}(\vartheta_1, \vartheta_2, x) = \mathbf{OW} = \begin{bmatrix} X \\ Y \\ \sqrt{X^2 + Y^2}\ \tan(\vartheta_2) \end{bmatrix} \tag{A.42}$$

Let now consider the bellows membrane. Similarly to what depicted for the pleated geometry, the generic membrane configuration is shown in Figure 2.3 (c). By referring to Figure A.3, the following geometrical bellows parameters can be estimated:

$$h_b(x) = \frac{L_b + |x|}{2N_b} \tag{A.43}$$

$$\alpha_b(x) = \sin^{-1}\left(\frac{h_b(x)}{A_b B_b}\right) \tag{A.44}$$

$$R_{v,b}(x) = \frac{(R_{i,b} - d_b/2)\sin\alpha_b(x)}{1 - \sin\alpha_b(x)} \tag{A.45}$$

$$R_{c,b}(x) = \frac{\mathscr{L}_b - R_{v,b}(x)\left(\pi/2 - \alpha_b(x)\right)}{\pi/2 - \alpha_b(x) - 1/\tan\alpha_b(x)} - \frac{(h_b(x) - h_{1,b}(x))/\sin\alpha_b(x)}{\pi/2 - \alpha_b(x) - 1/\tan\alpha_b(x)} \tag{A.46}$$

with:

$$h_{1,b}(x) = R_{v,b}(x)\ \cos\alpha_b(x) \tag{A.47}$$

and $\mathscr{L}_b$ is computed with respect to the undeformed configuration:

$$\mathscr{L}_b = R_{v,b}\left(\frac{\pi}{2} - \alpha_b\right) + R_{c,b}\left(\frac{\pi}{2} - \alpha_b\right) + \frac{h_b - h_{1,b} - R_{s,1}\cos\alpha_b}{\sin\alpha_b} \tag{A.48}$$

It is worth noting the above equations where derived by assuming the length $A_b B_b$ as constant, i.e. assuming the actuator deformation solely consists of the folding/unfolding process.

The generic angle $\varphi(\theta_1, x)$ in Equation A.12 is a function of the latitude $\vartheta_1$ and the linear stroke $x$. Let consider the geometric construction in Figure A.5:

$$r(\vartheta_1, x)(1 - \cos(\varphi)) = \rho(\vartheta_1, 0, x) - \rho(\vartheta_1, \vartheta_{2,\max}, x) \tag{A.49}$$

$$r(\vartheta_1, x)\sin(\varphi, x) = \frac{L + x}{2} \tag{A.50}$$

Let combine Equations A.49 and A.50 by making $r$ explicit and let reformulate the resulting equation by exploiting the half-angle and double-angle formulae for sine:

$$\varphi(\vartheta_1, x) = 2\ \tan^{-1}\left(\frac{2}{L + x}\left(\rho(\vartheta_1, 0) - \rho(\vartheta_1, \vartheta_{2,\max})\right)\right) \tag{A.51}$$

where the maximum longitude can be derived by considering the longitudinal crest fibre, for which the following applies:

$$\rho(0, \theta_{2,\,\mathrm{max}}) = R_{oe,p} \tag{A.52}$$

$$\vartheta_{2,\mathrm{max}}(x) = \tan^{-1}\left(\frac{L+x}{2\,R_{oe,p}}\right) \tag{A.53}$$

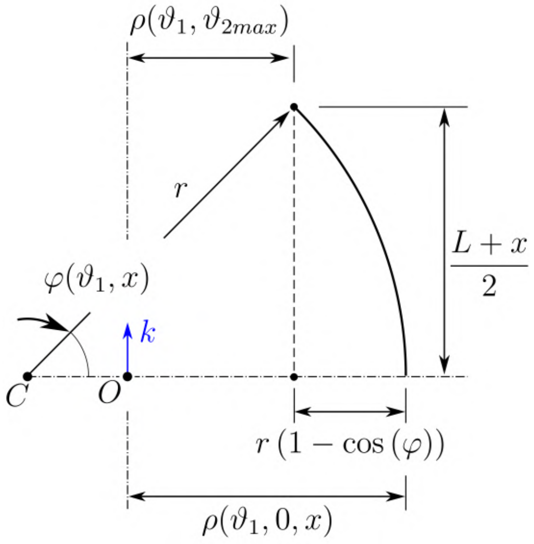

Figure A.5: Representation of angle $\varphi(\theta_1, x)$.

## A.2 Antagonist area and internal volumes

The evaluation of the antagonist area $A_a$ in Figure 2.5 (b) and (c) starts from the computation of the three portions $A_{a,[I,II,III]}$ in Figure A.1. The area of the terminal cross-section of the pleated membrane is clearly equal to:

$$A_{a,p} = 2\,N\,(A_{a,I} + A_{a,II} + A_{a,III}) \tag{A.54}$$

The first portion $A_{a,I}$ can be estimated as the union of the circular sector centred in $C_{ce}$, a radius of $R_{ce}$ and a central angle $\beta_e$; and the triangle $O'C_{ce}S_{ce}$ in Figure A.6 (a):

$$A_{a,I} = \frac{1}{2}\,R_{ce}^2\,\beta_e + \frac{1}{2}\,(R_{oe} - R_{ce})R_{ce}\,\sin(\beta_e) = \frac{1}{2}\,R_{ce}^2\,\beta_e + \frac{1}{2}\,R_{ce}^2(A-1)\,\sin(\beta_e) \tag{A.55}$$

On other hand, the area of the second portion can be evaluated by considering the triangle $O'S_{ce}S_{ve}$ in Figure A.6 (b):

$$A_{a,II} = \frac{1}{2}\,O'S_{ce} \cdot S_{ce}S_{ve}\,\sin\left(\frac{\pi}{2} - (\beta_e - \delta)\right) \tag{A.56}$$

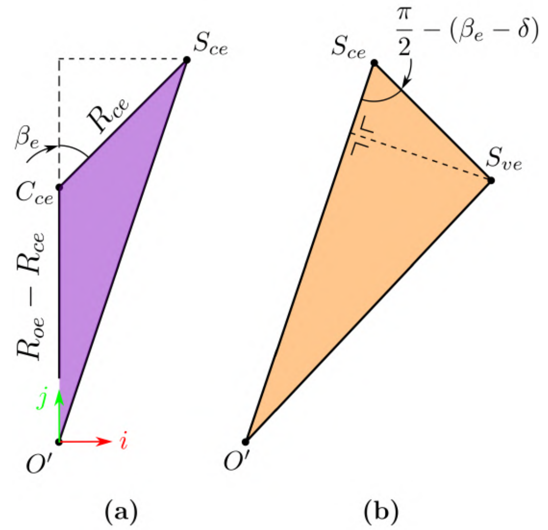

Figure A.6: Computation of the antagonistic area, **(a)** portion I, **(b)** portion II.

where:

$$S_{ce}S_{ve} = \left(O'S_{ce}^2 + O'S_{ve}^2 - 2O'S_{ce} \cdot O'S_{ve} \cos(\alpha_p/2 - \delta - \gamma)\right)^{1/2} \tag{A.57}$$

$$O'S_{ce} = \left((R_{oe} - R_{ce})^2 + R_{ce}^2 - 2(R_{oe} - R_{ce})R_{ce} \cos(\pi - \beta_e)\right)^{1/2} \tag{A.58}$$

Finally, the area of the last portion can be computed as the difference between the triangle $O'S_{ve}C_{ve}$ and the circular sector centred in $C_{ve}$, a radius of $R_{ve}$ and a central angle of $\beta_e - \alpha p/2$:

$$\begin{aligned} A_{a,III} =& \frac{1}{2}(R_{ie} + R_{ve})R_{ve} \sin\left(\beta_e - \frac{\alpha_p}{2}\right) - \frac{1}{2} R_{ve}^2 \left(\beta_e - \frac{\alpha_p}{2}\right) = \\ =& \frac{1}{2}\frac{R_{ce}^2}{C^2}\left((B+1)\sin\left(\beta - \frac{\alpha_p}{2}\right) - \left(\beta_e - \frac{\alpha_p}{2}\right)\right) \end{aligned} \tag{A.59}$$

On other hand, the evaluation of the antagonist area of the bellows is straightforward:

$$A_{a,b} = \pi R_{i,b}^2 \tag{A.60}$$

The net antagonist area can thus be derived also considering the different type A and B working modes, as observed in section 2.2.2:

$$A_a = \begin{cases} A_{a,p} - A_{a,b} & \text{type A} \\ A_{a,p} & \text{type B} \end{cases} \tag{A.61}$$

Let now focus on the internal volumes computation. To this aim, let consider the divergence theorem in its generic form:

$$\int_V \nabla \cdot \underline{q}\, dV = \oint_{\partial V} \underline{q} \cdot \hat{n}\, dA \tag{A.62}$$

where $\delta V$ is the boundary of region $V$ and $\mathbf{q}$ is a vector field. Thus, thanks to the BiSoft.Q geometric simmetry, let apply Equation A.62 to the $(1/2N)$-th portion of the pleated membrane, as shown in Figure A.7. The right-hand side on Equation A.62 can be decomposed as follows:

$$\oint_{\partial V} \mathbf{q} \cdot \hat{n}\, dA = \sum_{m=1}^{5} \int_{A_m} \mathbf{q} \cdot \hat{n}_m\, dA \tag{A.63}$$

where $\hat{n}_1$ is defined in Equation 2.5 and the remaining unit vectors are equal to:

$$\hat{n}_2 = (0, 0, 1) \tag{A.64}$$

$$\hat{n}_3 = (0, 0, -1) \tag{A.65}$$

$$\hat{n}_4 = (-1, 0, 0) \tag{A.66}$$

$$\hat{n}_5 = \big(\cos(\alpha_p/2), -\sin(\alpha_p/2), 0\big) \tag{A.67}$$

Let now choose a convenient expression for $\mathbf{q}$:

$$\mathbf{q} = (0, 0, Z) \tag{A.68}$$

which enables to make null the fourth and fifth term of the summation in Equation A.63. The remaining terms can be reformulated as follows:

$$A_2 = A_3 = A_I + A_{II} + A_{III} \tag{A.69}$$

$$\int_{A_{[2,3]}} \mathbf{q} \cdot \hat{n}_{[2,3]}\, dA = \frac{L + x}{2}\,(A_I + A_{II} + A_{III}) \tag{A.70}$$

As regards to the left-hand side of Equation A.63, since $\nabla \cdot \underline{q} = 1$, it merely represents the internal volume of the $(1/2N)$-th pleated membrane portion. The total volume $V_p$ is thus equal to:

$$V_p(x) = 2\,N\Big( \int_0^{\alpha_p/2} \int_{-\vartheta_{2,\max}}^{\vartheta_{2,\max}} Z(\vartheta_1, \vartheta_2, x)\, n_{1,k}\, d\vartheta_1 d\vartheta_2 + (L + x)(A_I + A_{II} + A_{III}) \Big) \tag{A.71}$$

On other hand, the bellows geometry can be estimated as:

$$V_b(x) = 2\,N_b\big(V_{I,b}(x) + V_{II,b}(x) + V_{III,b}(x)\big) \tag{A.72}$$

where the three bellows portions II, II and III are shown in Figure A.3, and are equal to:

$$V_{I,b}(x) = \pi\, R_{t1,b}(x)^2\, h_{1,b}(x) - 2\,\pi\, r_{v,b}(x) A_{v,b}(x) \tag{A.73}$$

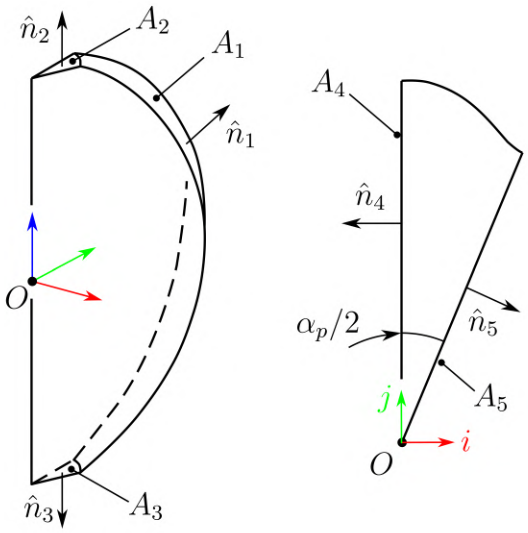

Figure A.7: Representation of the internal volume of the $(1/2N)$-th portion of the pleated membrane. The flux of $\mathbf{q}$ through both $A_4$ and $A_5$ is null.

$$V_{II,b}(x) = \frac{1}{3}\,\pi\left(h_{2,b}(x) - h_{1,b}(x)\right)\left(R_{t1,b}(x)^2 + R_{t1,b}(x)R_{t2,b}(x) + R_{t2,b}(x)^2\right) \tag{A.74}$$

$$V_{III,b}(x) = \pi\,R_{c,b}(x)^2\left(h_b(x) - h_{2,b}(x)\right) + 2\,\pi\,r_{c,b}(x)A_{c,b}(x) \tag{A.75}$$

where:

$$A_{v,b}(x) = \frac{1}{2}\left(R_{v,b}(x)^2\left(\frac{\pi}{2} - \alpha_b(x)\right) - h_{1,b}(x)R_{v,b}(x)\cos\left(\frac{\pi}{2} - \alpha_b(x)\right)\right) \tag{A.76}$$

$$\begin{aligned} A_{c,b}(x) =& \frac{1}{2}\left(R_{c,b}(x)^2\left(\frac{\pi}{2} - \alpha_b(x)\right) + \right. \\ & \left. - \left(h_b(x) - h_{2,b}(x)\right)R_{c,b}(x)\cos\left(\frac{\pi}{2} - \alpha_b(x)\right)\right) \end{aligned} \tag{A.77}$$

The internal volumes of the BiSoft.Q chambers can eventually be estimated as follows:

$$V_{\text{ch. }1}(x) = \begin{cases} V_p(x) - V_b(x) & \text{type A} \\ V_p(x) & \text{type B} \end{cases} \tag{A.78}$$

$$V_{\text{ch. }2}(x) = \begin{cases} V_b(x) & \text{type A} \\ V_b(x) - V_p(x) & \text{type B} \end{cases} \tag{A.79}$$

# Bibliography

[1] Elena Garcia et al. "The evolution of robotics research." In: *IEEE Robotics & Automation Magazine* 14.1 (Mar. 2007). Conference Name: IEEE Robotics & Automation Magazine, pp. 90–103. ISSN: 1558-223X. DOI: `10.1109/MRA.2007.339608`.

[2] *THE 17 GOALS | Sustainable Development.* URL: `https://sdgs.un.org/goals` (visited on 02/09/2025).

[3] Catherine P Bishop. "Sustainability lessons from appropriate technology." In: *Current Opinion in Environmental Sustainability* 49 (Apr. 2021), pp. 50–56. ISSN: 1877-3435. DOI: `10.1016/j.cosust.2021.02.011`.

[4] Tatsuya Nomura et al. "What people assume about humanoid and animal-type robots: Cross-cultural analysis between Japan, Korea, and the United Utates." English. In: *International Journal of Humanoid Robotics* 5.1 (Mar. 2008). Publisher: World Scientific Publishing Co. Pte Ltd, pp. 25–46. ISSN: 0219-8436. DOI: `10.1142/S0219843608001297`.

[5] IFR International Federation of Robotics. *International Federation of Robotics.* en. URL: `https://ifr.org/wr-service-robots` (visited on 01/29/2025).

[6] Ricardo Morales et al. "Pneumatic robotic systems for upper limb rehabilitation." en. In: *Medical & Biological Engineering & Computing* 49.10 (Oct. 2011), pp. 1145–1156. ISSN: 1741-0444. DOI: `10.1007/s11517-011-0814-3`.

[7] Theresa A. Jones et al. "Motor Skills Training Enhances Lesion-Induced Structural Plasticity in the Motor Cortex of Adult Rats." en. In: *Journal of Neuroscience* 19.22 (Nov. 1999). Publisher: Society for Neuroscience Section: ARTICLE, pp. 10153–10163. ISSN: 0270-6474, 1529-2401. DOI: `10.1523/JNEUROSCI.19-22-10153.1999`.

[8] Gerd Kempermann, Henriette van Praag, and Fred H. Gage. "Chapter 3 Activity-dependent regulation of neuronal plasticity and self repair." In: *Progress in Brain Research.* Vol. 127. Functional Neural Transplantation II. Novel Cell Therapies For CNS Disorders. Elsevier, Jan. 2000, pp. 35–48. DOI: `10.1016/S0079-6123(00)27004-0`.

[9] Paul Lam et al. “A haptic-robotic platform for upper-limb reaching stroke therapy: Preliminary design and evaluation results.” en. In: *Journal of NeuroEngineering and Rehabilitation* 5.1 (May 2008), p. 15. ISSN: 1743-0003. DOI: 10.1186/1743-0003-5-15.

[10] H. I. Krebs and B. T. Volpe. “Chapter 23 - Rehabilitation Robotics.” In: *Handbook of Clinical Neurology*. Ed. by Michael P. Barnes and David C. Good. Vol. 110. Neurological Rehabilitation. Elsevier, Jan. 2013, pp. 283–294. DOI: 10.1016/B978-0-444-52901-5.00023-X.

[11] Patrizia Poli et al. “Robotic Technologies and Rehabilitation: New Tools for Stroke Patients’ Therapy.” en. In: *BioMed Research International* 2013.1 (2013), p. 153872. ISSN: 2314-6141. DOI: 10.1155/2013/153872.

[12] Hao Su, Gregory A. Cole, and Gregory S. Fischer. “High-Field MRI-Compatible Needle Placement Robots for Prostate Interventions: Pneumatic and Piezoelectric Approaches.” en. In: *Advances in Robotics and Virtual Reality*. Ed. by Tauseef Gulrez and Aboul Ella Hassanien. Berlin, Heidelberg: Springer, 2012, pp. 3–32. ISBN: 978-3-642-23363-0. DOI: 10.1007/978-3-642-23363-0_1.

[13] Haytham Elhawary et al. “The case for MR-compatible robotics: a review of the state of the art.” en. In: *The International Journal of Medical Robotics and Computer Assisted Surgery* 4.2 (2008), pp. 105–113. ISSN: 1478-596X. DOI: 10.1002/rcs.192.

[14] Kevin Cleary et al. “Interventional robotic systems: Applications and technology state-of-the-art.” In: *Minimally Invasive Therapy & Allied Technologies* 15.2 (Jan. 2006). Publisher: Taylor & Francis, pp. 101–113. ISSN: 1364-5706. DOI: 10.1080/13645700600674179.

[15] B.L. Luk et al. “Walking and Climbing Service Robots for Safety Inspection of Nuclear Reactor Pressure Vessels.” en. In: *Measurement and Control* 39.2 (Mar. 2006). Publisher: SAGE Publications Ltd, pp. 43–47. ISSN: 0020-2940. DOI: 10.1177/002029400603900201.

[16] Domenico Longo and Giovanni Muscato. “Adhesion techniques for climbing robots: state of the art and experimental considerations.” In: *Advances in Mobile Robotics*. WORLD SCIENTIFIC, Aug. 2008, pp. 6–28. ISBN: 978-981-283-576-5. DOI: 10.1142/9789812835772_0003.

[17] Hae-Bum Yun et al. “Development of Inspection Robots for Bridge Cables.” en. In: *The Scientific World Journal* 2013.1 (2013), p. 967508. ISSN: 1537-744X. DOI: 10.1155/2013/967508.

[18] Kyung-Hyun Yoon and Young-Woo Park. “Pipe inspection robot actuated by using compressed air.” In: *2010 IEEE/ASME International Conference on Advanced Intelligent Mechatronics*. ISSN: 2159-6255. July 2010, pp. 1345–1349. DOI: 10.1109/AIM.2010.5695865.

[19] I- Ming Chen and Song Huat Yeo. “Locomotion of a Two-Dimensional Walking-Climbing Robot Using A Closed-Loop Mechanism: From Gait Generation to Navigation.” en. In: *The International Journal of Robotics Research* 22.1 (Jan. 2003). Publisher: SAGE Publications Ltd STM, pp. 21–40. ISSN: 0278-3649. DOI: 10.1177/02783649030220010003.

[20] Johann Borenstein, Grzegorz Granosik, and Malik Hansen. “The OmniTread serpentine robot: design and field performance.” In: *Unmanned Ground Vehicle Technology VII*. Vol. 5804. SPIE, May 2005, pp. 324–332. DOI: 10.1117/12.601486.

[21] H. Ohno and S. Hirose. “Study on slime robot (proposal of slime robot and design of slim slime robot).” In: *Proceedings. 2000 IEEE/RSJ International Conference on Intelligent Robots and Systems (IROS 2000) (Cat. No.00CH37113)*. Vol. 3. Oct. 2000, 2218–2223 vol.3. DOI: 10.1109/IROS.2000.895298.

[22] H. Tsukagoshi et al. “Design of a Higher Jumping Rescue Robot with the Optimized Pneumatic Drive.” In: *Proceedings of the 2005 IEEE International Conference on Robotics and Automation*. ISSN: 1050-4729. Apr. 2005, pp. 1276–1283. DOI: 10.1109/ROBOT.2005.1570291.

[23] Jianyong Li et al. “Design of continuous climbing pneumatic cable maintenance robot.” In: *2009 International Conference on Mechatronics and Automation*. ISSN: 2152-744X. Aug. 2009, pp. 4633–4637. DOI: 10.1109/ICMA.2009.5244793.

[24] Jun Luo et al. “Development of cable maintenance robot for cable-stayed bridges.” In: *Industrial Robot: An International Journal* 34.4 (Jan. 2007). Publisher: Emerald Group Publishing Limited, pp. 303–309. ISSN: 0143-991X. DOI: 10.1108/01439910710749627.

[25] Hyeun-Seok Choi et al. “Development of hybrid robot for construction works with pneumatic actuator.” In: *Automation in Construction*. 20th International Symposium on Automation and Robotics in Construction: The Future Site 14.4 (Aug. 2005), pp. 452–459. ISSN: 0926-5805. DOI: 10.1016/j.autcon.2004.09.008.

[26] Mario M. Foglia and Giulio Reina. “Agricultural robot for radicchio harvesting.” en. In: *Journal of Field Robotics* 23.6-7 (2006), pp. 363–377. ISSN: 1556-4967. DOI: 10.1002/rob.20131.

[27] Marco Ceccarelli et al. “Designing a robotic gripper for harvesting horticulture products.” en. In: *Robotica* 18.1 (Jan. 2000), pp. 105–111. ISSN: 1469-8668, 0263-5747. DOI: 10.1017/S026357479900226X.

[28] A. Manuello Bertetto et al. “An integrated device for saffron flowers detaching and harvesting.” In: *19th International Workshop on Robotics in Alpe-Adria-Danube Region (RAAD 2010)*. June 2010, pp. 93–98. DOI: 10.1109/RAAD.2010.5524604.

[29] G. Carducci et al. “Pneumatic robotic arm controlled by on-off valves for automatic harvesting based on vision localisation.” In: *2004 IEEE International Conference on Industrial Technology, 2004. IEEE ICIT ’04*. Vol. 2. Dec. 2004, 1017–1022 Vol. 2. DOI: 10.1109/ICIT.2004.1490216.

[30] Carlos Blanes et al. “Assessment of eggplant firmness with accelerometers on a pneumatic robot gripper.” In: *Computers and Electronics in Agriculture* 113 (Apr. 2015), pp. 44–50. ISSN: 0168-1699. DOI: 10.1016/j.compag.2015.01.013.

[31] Kanae Tanigaki et al. “Cherry-harvesting robot.” In: *Computers and Electronics in Agriculture*. Special issue on bio-robotics 63.1 (Aug. 2008), pp. 65–72. ISSN: 0168-1699. DOI: 10.1016/j.compag.2008.01.018.

[32] Christopher Lehnert et al. “Autonomous Sweet Pepper Harvesting for Protected Cropping Systems.” In: *IEEE Robotics and Automation Letters* 2.2 (Apr. 2017). Conference Name: IEEE Robotics and Automation Letters, pp. 872–879. ISSN: 2377-3766. DOI: 10.1109/LRA.2017.2655622.

[33] Bertrand Tondu and Pierre Lopez. “The McKibben muscle and its use in actuating robot-arms showing similarities with human arm behaviour.” In: *Industrial Robot: An International Journal* 24.6 (Jan. 1997). Publisher: MCB UP Ltd, pp. 432–439. ISSN: 0143-991X. DOI: 10.1108/01439919710192563.

[34] Bertrand Tondu. “Modelling of the McKibben artificial muscle: A review.” en. In: *Journal of Intelligent Material Systems and Structures* 23.3 (Feb. 2012). Publisher: SAGE Publications Ltd STM, pp. 225–253. ISSN: 1045-389X. DOI: 10.1177/1045389X11435435.

[35] Taimoor Hassan et al. “Finite-Element Modeling and Design of a Pneumatic Braided Muscle Actuator With Multifunctional Capabilities.” In: *IEEE/ASME Transactions on Mechatronics* 24.1 (Feb. 2019). Conference Name: IEEE/ASME Transactions on Mechatronics, pp. 109–119. ISSN: 1941-014X. DOI: 10.1109/TMECH.2018.2877125.

[36] Michele G Antonelli et al. “Numerical modelling and experimental validation of a McKibben pneumatic muscle actuator.” en. In: *Journal of Intelligent Material Systems and Structures* 28.19 (Nov. 2017). Publisher: SAGE Publications Ltd STM, pp. 2737–2748. ISSN: 1045-389X. DOI: 10.1177/1045389X17698245.

[37] Steven D. Thomalla and James D. Van de Ven. “Modeling and Implementation of the McKibben Actuator in Hydraulic Systems.” In: *IEEE Transactions on Robotics* 34.6 (Dec. 2018). Conference Name: IEEE Transactions on Robotics, pp. 1593–1602. ISSN: 1941-0468. DOI: 10.1109/TRO.2018.2864780.

[38] Shigeyoshi Yahara et al. “McKibben artificial muscle realizing variable contraction characteristics using helical shape-memory polymer fibers.” In: *Sensors and Actuators A: Physical* 295 (Aug. 2019), pp. 637–642. ISSN: 0924-4247. DOI: 10.1016/j.sna.2019.06.012.

[39] Michael A Meller, Matthew Bryant, and Ephrahim Garcia. "Reconsidering the McKibben muscle: Energetics, operating fluid, and bladder material." en. In: *Journal of Intelligent Material Systems and Structures* 25.18 (Dec. 2014). Publisher: SAGE Publications Ltd STM, pp. 2276–2293. ISSN: 1045-389X. DOI: 10.1177/1045389X14549872.

[40] Danial Sangian et al. "Three-Dimensional Printed Braided Sleeves for Manufacturing McKibben Artificial Muscles." In: *3D Printing and Additive Manufacturing* 6.1 (Mar. 2019). Publisher: Mary Ann Liebert, Inc., publishers, pp. 57–62. ISSN: 2329-7662. DOI: 10.1089/3dp.2018.0103.

[41] Peng Liu, Daoxiong Gong, and Jianjun Yu. "Design of a Knitting Thin McKibben Muscle." In: *2023 International Conference on Service Robotics (ICoSR)*. July 2023, pp. 1–5. DOI: 10.1109/ICoSR59980.2023.00011.

[42] B. Tondu, V. Boitier, and P. Lopez. "Naturally compliant robot-arms actuated by McKibben artificial muscles." In: *Proceedings of IEEE International Conference on Systems, Man and Cybernetics*. Vol. 3. Oct. 1994, 2635–2640 vol. 3. DOI: 10.1109/ICSMC.1994.400269.

[43] Michael F. Cullinan et al. "A McKibben Type Sleeve Pneumatic Muscle and Integrated Mechanism for Improved Stroke Length." In: *Journal of Mechanisms and Robotics* 9.011013 (Jan. 2017). ISSN: 1942-4302. DOI: 10.1115/1.4035496.

[44] Martin Tschiersky et al. "A Compact McKibben Muscle Based Bending Actuator for Close-to-Body Application in Assistive Wearable Robots." In: *IEEE Robotics and Automation Letters* 5.2 (Apr. 2020). Conference Name: IEEE Robotics and Automation Letters, pp. 3042–3049. ISSN: 2377-3766. DOI: 10.1109/LRA.2020.2975732.

[45] Simona Aracri et al. "Soft Robotics: A Route to Equality, Diversity, and Inclusivity in Robotics." In: *Soft Robotics* 11.6 (Dec. 2024). Publisher: Mary Ann Liebert, Inc., publishers, pp. 903–910. ISSN: 2169-5172. DOI: 10.1089/soro.2023.0225.

[46] Charbel Tawk and Gursel Alici. "A Review of 3D-Printable Soft Pneumatic Actuators and Sensors: Research Challenges and Opportunities." en. In: *Advanced Intelligent Systems* 3.6 (2021), p. 2000223. ISSN: 2640-4567. DOI: 10.1002/aisy.202000223.

[47] Sangbae Kim, Cecilia Laschi, and Barry Trimmer. "Soft robotics: a bioinspired evolution in robotics." English. In: *Trends in Biotechnology* 31.5 (May 2013). Publisher: Elsevier, pp. 287–294. ISSN: 0167-7799, 1879-3096. DOI: 10.1016/j.tibtech.2013.03.002.

[48] Jun Shintake et al. "Soft Robotic Grippers." en. In: *Advanced Materials* 30.29 (2018), p. 1707035. ISSN: 1521-4095. DOI: 10.1002/adma.201707035.

[49] Panagiotis Polygerinos et al. "Soft Robotics: Review of Fluid-Driven Intrinsically Soft Devices; Manufacturing, Sensing, Control, and Applications in Human-Robot Interaction." en. In: *Advanced Engineering Materials* 19.12 (2017), p. 1700016. ISSN: 1527-2648. DOI: `10.1002/adem.201700016`.

[50] Filip Ilievski et al. "Soft Robotics for Chemists." In: *Angewandte Chemie International Edition* 50.8 (2011), pp. 1890–1895. ISSN: 1521-3773. DOI: `10.1002/anie.201006464`.

[51] Stephen A. Morin et al. "Camouflage and Display for Soft Machines." In: *Science* 337.6096 (Aug. 2012). Publisher: American Association for the Advancement of Science, pp. 828–832. DOI: `10.1126/science.1222149`.

[52] Fenglin Han et al. "A Restorable, Variable Stiffness Pneumatic Soft Gripper Based on Jamming of Strings of Beads." In: *IEEE Transactions on Robotics* 39.5 (Oct. 2023). Conference Name: IEEE Transactions on Robotics, pp. 4065–4077. ISSN: 1941-0468. DOI: `10.1109/TRO.2023.3280595`.

[53] Antonio López-Díaz et al. "Hydrogel-based soft pneumatic bending actuator with self-healing and proprioception capabilities." In: *2022 IEEE 5th International Conference on Soft Robotics (RoboSoft)*. Apr. 2022, pp. 370–375. DOI: `10.1109/RoboSoft54090.2022.9762200`.

[54] Michael A. Bell et al. "A Modular and Self-Contained Fluidic Engine for Soft Actuators." en. In: *Advanced Intelligent Systems* 4.1 (2022), p. 2100094. ISSN: 2640-4567. DOI: `10.1002/aisy.202100094`.

[55] Trevor J. Jones et al. "Bubble casting soft robotics." en. In: *Nature* 599.7884 (Nov. 2021). Publisher: Nature Publishing Group, pp. 229–233. ISSN: 1476-4687. DOI: `10.1038/s41586-021-04029-6`.

[56] Qinjie Ji and Aiguo Song. "Bionic Snail Robot Enhanced by Poroelastic Foams Crawls Using Direct and Retrograde Waves." In: *Soft Robotics* 11.3 (June 2024). Publisher: Mary Ann Liebert, Inc., publishers, pp. 453–463. ISSN: 2169-5172. DOI: `10.1089/soro.2023.0077`.

[57] Benjamin C. Mac Murray et al. "Poroelastic Foams for Simple Fabrication of Complex Soft Robots." In: *Advanced Materials* 27.41 (2015), pp. 6334–6340. ISSN: 1521-4095. DOI: `10.1002/adma.201503464`.

[58] Matheus S. Xavier et al. "Soft Pneumatic Actuators: A Review of Design, Fabrication, Modeling, Sensing, Control and Applications." In: *IEEE Access* 10 (2022). Conference Name: IEEE Access, pp. 59442–59485. ISSN: 2169-3536. DOI: `10.1109/ACCESS.2022.3179589`.

[59] Ela Sachyani Keneth et al. "3D Printing Materials for Soft Robotics." en. In: *Advanced Materials* 33.19 (2021), p. 2003387. ISSN: 1521-4095. DOI: `10.1002/adma.202003387`.

[60] Mohammadreza Lalegani Dezaki et al. "Soft Pneumatic Actuators with Controllable Stiffness by Bio-Inspired Lattice Chambers and Fused Deposition Modeling 3D Printing." en. In: *Advanced Engineering Materials* 25.6 (2023), p. 2200797. ISSN: 1527-2648. DOI: `10.1002/adem.202200797`.

[61] Soya Eguchi et al. "Pneumatic Auxetics: Inverse design and 3D printing of auxetic pattern for pneumatic morphing." In: *Extended Abstracts of the 2022 CHI Conference on Human Factors in Computing Systems*. CHI EA '22. New York, NY, USA: Association for Computing Machinery, Apr. 2022, pp. 1–7. ISBN: 978-1-4503-9156-6. DOI: `10.1145/3491101.3519801`.

[62] A. Heiden et al. "3D printing of resilient biogels for omnidirectional and exteroceptive soft actuators." In: *Science Robotics* 7.63 (Feb. 2022). Publisher: American Association for the Advancement of Science, eabk2119. DOI: `10.1126/scirobotics.abk2119`.

[63] Yuki Takishima et al. "Fully 3D-Printed Hydrogel Actuator for Jellyfish Soft Robots." en. In: *ECS Journal of Solid State Science and Technology* 10.3 (Mar. 2021). Publisher: IOP Publishing, p. 037002. ISSN: 2162-8777. DOI: `10.1149/2162-8777/abea5f`.

[64] Honumant Nethani et al. "Silicone-Based Additive Manufacturing." In: *Polymer-Plastics Technology and Materials* 0.0 (). Publisher: Taylor & Francis, pp. 1–21. ISSN: 2574-0881. DOI: `10.1080/25740881.2024.2445610`.

[65] Erina Baynojir Joyee and Yayue Pan. "Multi-material Additive Manufacturing of Functional Soft Robot." In: *Procedia Manufacturing* 34 (2019). 47th SME North American Manufacturing Research Conference, NAMRC 47, Pennsylvania, USA., pp. 566–573. ISSN: 2351-9789. DOI: `https://doi.org/10.1016/j.promfg.2019.06.221`.

[66] Dinesh K Patel et al. "Highly stretchable and UV curable elastomers for digital light processing based 3D printing." In: *Advanced Materials* 29.15 (2017), p. 1606000.

[67] Qingchuan Song et al. "Fabrication of Multi-Material Pneumatic Actuators and Microactuators Using Stereolithography." In: *Micromachines* 14.2 (2023). ISSN: 2072-666X. DOI: `10.3390/mi14020244`.

[68] N. Bhattacharjee et al. "Desktop-Stereolithography 3D-Printing of a Poly(dimethylsiloxane)-Based Material with Sylgard-184 Properties." In: *Advanced Materials* 30.22 (2018). DOI: `10.1002/adma.201800001`.

[69] Manuel Schaffner et al. "3D printing of robotic soft actuators with programmable bioinspired architectures." en. In: *Nature Communications* 9.1 (Feb. 2018). Publisher: Nature Publishing Group, p. 878. ISSN: 2041-1723. DOI: `10.1038/s41467-018-03216-w`.

[70] Yin Cheng et al. "Direct-Ink-Write 3D Printing of Hydrogels into Biomimetic Soft Robots." In: *ACS Nano* 13.11 (Nov. 2019). Publisher: American Chemical Society, pp. 13176–13184. ISSN: 1936-0851. DOI: 10.1021/acsnano.9b06144.

[71] Zhenhua Wang et al. "Freeform Fabrication of Pneumatic Soft Robots via Multi-Material Jointed Direct Ink Writing." en. In: *Macromolecular Materials and Engineering* 307.4 (2022), p. 2100813. ISSN: 1439-2054. DOI: 10.1002/mame.202100813.

[72] Xinjun Sheng et al. "Multi-material 3D printing of caterpillar-inspired soft crawling robots with the pneumatically bellow-type body and anisotropic friction feet." In: *Sensors and Actuators A: Physical* 316 (Dec. 2020), p. 112398. ISSN: 0924-4247. DOI: 10.1016/j.sna.2020.112398.

[73] Peter Kappel et al. "Application-Oriented Comparison of Two 3D Printing Processes for the Manufacture of Pneumatic Bending Actuators for Bioinspired Macroscopic Soft Gripper Systems." en. In: *Biomimetic and Biohybrid Systems.* Ed. by Alexander Hunt et al. Cham: Springer International Publishing, 2022, pp. 54–67. ISBN: 978-3-031-20470-8. DOI: 10.1007/978-3-031-20470-8_6.

[74] Edoardo Milana et al. "Out-of-Plane Soft Lithography for Soft Pneumatic Microactuator Arrays." In: *Soft Robotics* 10.1 (Feb. 2023). Publisher: Mary Ann Liebert, Inc., publishers, pp. 197–204. ISSN: 2169-5172. DOI: 10.1089/soro.2021.0106.

[75] Sheila Russo et al. "An Additive Millimeter-Scale Fabrication Method for Soft Biocompatible Actuators and Sensors." en. In: *Advanced Materials Technologies* 2.10 (2017). _eprint: https://onlinelibrary.wiley.com/doi/pdf/10.1002/admt.201700135, p. 1700135. ISSN: 2365-709X. DOI: 10.1002/admt.201700135.

[76] Tommaso Ranzani et al. "Increasing the Dimensionality of Soft Microstructures through Injection-Induced Self-Folding." en. In: *Advanced Materials* 30.38 (2018). _eprint: https://onlinelibrary.wiley.com/doi/pdf/10.1002/adma.201802739, p. 1802739. ISSN: 1521-4095. DOI: 10.1002/adma.201802739.

[77] Hend M. Elmoughni et al. "Machine-Knitted Seamless Pneumatic Actuators for Soft Robotics: Design, Fabrication, and Characterization." en. In: *Actuators* 10.5 (May 2021). Number: 5 Publisher: Multidisciplinary Digital Publishing Institute, p. 94. ISSN: 2076-0825. DOI: 10.3390/act10050094.

[78] Mengxin Yang et al. "Knitting from Nature: Self-Sensing Soft Robotics Enabled by All-in-One Knit Architectures." In: *ACS Applied Materials & Interfaces* 15.37 (Sept. 2023). Publisher: American Chemical Society, pp. 44294–44304. ISSN: 1944-8244. DOI: 10.1021/acsami.3c09029.

[79] Yiyue Luo et al. “Digital Fabrication of Pneumatic Actuators with Integrated Sensing by Machine Knitting.” In: *Proceedings of the 2022 CHI Conference on Human Factors in Computing Systems*. CHI ’22. New York, NY, USA: Association for Computing Machinery, Apr. 2022, pp. 1–13. ISBN: 978-1-4503-9157-3. DOI: `10.1145/3491102.3517577`.

[80] Mingke Wang, Yi Zhou, and Rebecca Stewart. “Soft Wearable Robotics: Innovative Knitting-Integrated Approaches for Pneumatic Actuators Design.” In: *Companion Publication of the 2024 ACM Designing Interactive Systems Conference*. DIS ’24 Companion. New York, NY, USA: Association for Computing Machinery, July 2024, pp. 234–238. ISBN: 9798400706325. DOI: `10.1145/3656156.3663700`.

[81] Vanessa Sanchez et al. “3D Knitting for Pneumatic Soft Robotics.” en. In: *Advanced Functional Materials* 33.26 (2023), p. 2212541. ISSN: 1616-3028. DOI: `10.1002/adfm.202212541`.

[82] Amir Ali Amiri Moghadam et al. “Laser Cutting as a Rapid Method for Fabricating Thin Soft Pneumatic Actuators and Robots.” In: *Soft Robotics* 5.4 (Aug. 2018). Publisher: Mary Ann Liebert, Inc., publishers, pp. 443–451. ISSN: 2169-5172. DOI: `10.1089/soro.2017.0069`.

[83] Donghua Shen et al. “Design and Analysis of a Novel Flat Pneumatic Artificial Muscle.” In: *2021 IEEE 8th International Conference on Industrial Engineering and Applications (ICIEA)*. Apr. 2021, pp. 110–114. DOI: `10.1109/ICIEA52957.2021.9436760`.

[84] Jacob Rogatinsky et al. “A Collapsible Soft Actuator Facilitates Performance in Constrained Environments.” en. In: *Advanced Intelligent Systems* 4.10 (2022). _eprint: https://onlinelibrary.wiley.com/doi/pdf/10.1002/aisy.202200085, p. 2200085. ISSN: 2640-4567. DOI: `10.1002/aisy.202200085`.

[85] Huaiyuan Chen, Yiyuan Ma, and Weidong Chen. “Design and Optimization of an Origami-Inspired Foldable Pneumatic Actuator.” In: *IEEE Robotics and Automation Letters* 9.2 (Feb. 2024). Conference Name: IEEE Robotics and Automation Letters, pp. 1278–1285. ISSN: 2377-3766. DOI: `10.1109/LRA.2023.3343624`.

[86] Zhuowen Li et al. “An Origami-Inspired Pneumatic Continuum Module with Active Variable Stiffness.” In: *2024 IEEE/RSJ International Conference on Intelligent Robots and Systems (IROS)*. ISSN: 2153-0866. Oct. 2024, pp. 8293–8298. DOI: `10.1109/IROS58592.2024.10801420`.

[87] Vera G Kortman et al. “A bio-inspired expandable soft suction gripper for minimal invasive surgery—an explorative design study.” en. In: *Bioinspiration & Biomimetics* 18.4 (May 2023). Publisher: IOP Publishing, p. 046004. ISSN: 1748-3190. DOI: `10.1088/1748-3190/accd35`.

[88] *SoftModBot*. en. URL: `https://www.softmodbot.com/` (visited on 01/21/2025).

[89] C.M. (Katrien) van Riet. "Soft Circuits Toolkit: A circuit-building kit that works on air." In: *Driving Design*. Ed. by Sally Bourdon, Julia Bertolaso, and Jessica Guy. Vol. II. Barcelona, Mar. 2024, pp. 96–101. ISBN: 978-84-12-08864-9.

[90] Min Pan et al. "Soft Actuators and Robotic Devices for Rehabilitation and Assistance." en. In: *Advanced Intelligent Systems* 4.4 (2022). _eprint: https://onlinelibrary.wiley.com/doi/pdf/10.1002/aisy.202100140, p. 2100140. ISSN: 2640-4567. DOI: `10.1002/aisy.202100140`.

[91] Jen-Hsuan Hsiao, Jen-Yuan (James) Chang, and Chao-Min Cheng. "Soft medical robotics: clinical and biomedical applications, challenges, and future directions." In: *Advanced Robotics* 33.21 (Nov. 2019). Publisher: Taylor & Francis _eprint: https://doi.org/10.1080/01691864.2019.1679251, pp. 1099–1111. ISSN: 0169-1864. DOI: `10.1080/01691864.2019.1679251`.

[92] Tanguy Ridremont et al. "Pneumatically Actuated Soft Robotic Hand and Wrist Exoskeleton for Motion Assistance in Rehabilitation." en. In: *Actuators* 13.5 (May 2024). Number: 5 Publisher: Multidisciplinary Digital Publishing Institute, p. 180. ISSN: 2076-0825. DOI: `10.3390/act13050180`.

[93] Inderjeet Singh et al. "Development of Soft Pneumatic Actuator Based Wrist Exoskeleton for Assistive Motion." In: *2023 IEEE/ASME International Conference on Advanced Intelligent Mechatronics (AIM)*. ISSN: 2159-6255. June 2023, pp. 359–366. DOI: `10.1109/AIM46323.2023.10196235`.

[94] Anoush Sepehri et al. "A Soft Robotic Wrist Orthosis Using Textile Pneumatic Actuators For Passive Rehabilitation." In: *2024 IEEE 7th International Conference on Soft Robotics (RoboSoft)*. ISSN: 2769-4534. Apr. 2024, pp. 284–290. DOI: `10.1109/RoboSoft60065.2024.10521992`.

[95] Juan C. Tejada et al. "Soft Robotic Hand Exoskeleton with Enhanced PneuNet-Type Pneumatic Actuators for Rehabilitation and Movement Assistance." en. In: *Journal of Robotics* 2024.1 (2024), p. 5815358. ISSN: 1687-9619. DOI: `10.1155/2024/5815358`.

[96] Panagiotis Polygerinos et al. "Soft robotic glove for combined assistance and at-home rehabilitation." In: *Robotics and Autonomous Systems*. Wearable Robotics 73 (Nov. 2015), pp. 135–143. ISSN: 0921-8890. DOI: `10.1016/j.robot.2014.08.014`.

[97] Yan Shen et al. "A Textile-Based Pneumatic Soft Suit for Elbow Joint Rehabilitation." In: *2024 IEEE 14th International Conference on CYBER Technology in Automation, Control, and Intelligent Systems (CYBER)*. ISSN: 2642-6633. July 2024, pp. 662–667. DOI: `10.1109/CYBER63482.2024.10749338`.

[98] Ajinkya Bhat, Jonathan William Ambrose, and Raye Chen-Hua Yeow. "Composite Soft Pneumatic Actuators Using 3D Printed Skins." In: *IEEE Robotics and Automation Letters* 8.4 (Apr. 2023). Conference Name: IEEE Robotics and Automation Letters, pp. 2086–2093. ISSN: 2377-3766. DOI: 10.1109/LRA.2023.3246841.

[99] Muhammad Umair Ahmad Khan et al. "A Soft Robotic Sleeve for Physiotherapy: Improving Elbow Rehabilitation in Baseball Pitchers." en. In: *Physiotherapy Research International* 30.1 (2025), e70025. ISSN: 1471-2865. DOI: 10.1002/pri.70025.

[100] Disheng Xie et al. "A Compact Elbow Exosuit Driven by Pneumatic Artificial Muscles." In: *IEEE Robotics and Automation Letters* 9.4 (Apr. 2024). Conference Name: IEEE Robotics and Automation Letters, pp. 3331–3338. ISSN: 2377-3766. DOI: 10.1109/LRA.2024.3366012.

[101] So Shimooka et al. "Development of Ankle-Joint Rehabilitation Device for Bedridden Patient Using Fan-Shaped Pneumatic Soft Actuator Driven at Low Pressure." In: *Journal of Robotics and Mechatronics* 35.3 (2023), pp. 565–576. DOI: 10.20965/jrm.2023.p0565.

[102] Grace P. Marconi, Alpha A. Gopalai, and Sunita Chauhan. "A hybrid ankle-foot orthosis with soft pneumatic actuation." In: *Mechatronics* 99 (May 2024), p. 103171. ISSN: 0957-4158. DOI: 10.1016/j.mechatronics.2024.103171.

[103] Dina Al-Shamkhani, Alaa Al-Ibadi, and Maria Elena Giannaccini. "Soft robot for ankle rehabilitation." In: *2023 16th International Conference on Developments in eSystems Engineering (DeSE)*. Dec. 2023, pp. 486–491. DOI: 10.1109/DeSE60595.2023.10468823.

[104] R.J. Sanchez et al. "A pneumatic robot for re-training arm movement after stroke: rationale and mechanical design." In: *9th International Conference on Rehabilitation Robotics, 2005. ICORR 2005.* ISSN: 1945-7901. June 2005, pp. 500–504. DOI: 10.1109/ICORR.2005.1501151.

[105] Parsa Kabir et al. "An inflatable soft wearable knee rehabilitation device: Design, fabrication, control and preliminary evaluation." In: *Mechatronics* 102 (Oct. 2024), p. 103233. ISSN: 0957-4158. DOI: 10.1016/j.mechatronics.2024.103233.

[106] Yong-Lae Park et al. "A soft wearable robotic device for active knee motions using flat pneumatic artificial muscles." In: *2014 IEEE International Conference on Robotics and Automation (ICRA)*. ISSN: 1050-4729. May 2014, pp. 4805–4810. DOI: 10.1109/ICRA.2014.6907562.

[107] Lorenzo Campioni et al. "Preliminary Evaluation of a Soft Wearable Robot for Shoulder Movement Assistance." In: *IEEE Transactions on Medical Robotics and Bionics* (2025). Conference Name: IEEE Transactions on Medical Robotics and Bionics, pp. 1–1. ISSN: 2576-3202. DOI: `10.1109/TMRB.2025.3527708`.

[108] Alexander Weymann et al. "Artificial Muscles and Soft Robotic Devices for Treatment of End-Stage Heart Failure." en. In: *Advanced Materials* 35.19 (2023), p. 2207390. ISSN: 1521-4095. DOI: `10.1002/adma.202207390`.

[109] Tommaso Ranzani et al. "A Soft Modular Manipulator for Minimally Invasive Surgery: Design and Characterization of a Single Module." In: *IEEE Transactions on Robotics* 32.1 (Feb. 2016). Conference Name: IEEE Transactions on Robotics, pp. 187–200. ISSN: 1941-0468. DOI: `10.1109/TRO.2015.2507160`.

[110] Jianlin Yang et al. "A Soft Inflatable Robot Driven by Hydraulic Folded Pouch Actuators for Minimally Invasive Surgery." In: *IEEE Robotics and Automation Letters* 9.5 (May 2024). Conference Name: IEEE Robotics and Automation Letters, pp. 4870–4877. ISSN: 2377-3766. DOI: `10.1109/LRA.2024.3386022`.

[111] Joseph DelPreto et al. "Sensorizing a Compression Sleeve for Continuous Pressure Monitoring and Lymphedema Treatment Using Pneumatic or Resistive Sensors." In: *2023 IEEE International Conference on Soft Robotics (RoboSoft)*. ISSN: 2769-4534. Apr. 2023, pp. 1–8. DOI: `10.1109/RoboSoft55895.2023.10122068`.

[112] Yuying Li et al. "SmartLact8: A Bio-Inspired Robotic Breast Pump for Customized and Comfort Milk Expression." en. In: *Biomimetics* 8.2 (June 2023). Number: 2 Publisher: Multidisciplinary Digital Publishing Institute, p. 190. ISSN: 2313-7673. DOI: `10.3390/biomimetics8020190`.

[113] Yuxuan Liu et al. "Intelligent Soft Robotic Grippers for Agricultural and Food Product Handling: A Brief Review with a Focus on Design and Control." en. In: *Advanced Intelligent Systems* 5.12 (2023). _eprint: https://onlinelibrary.wiley.com/doi/pdf/10.1002/aisy.202300233, p. 2300233. ISSN: 2640-4567. DOI: `10.1002/aisy.202300233`.

[114] Tantan Jin and Xiongzhe Han. "Robotic arms in precision agriculture: A comprehensive review of the technologies, applications, challenges, and future prospects." In: *Computers and Electronics in Agriculture* 221 (2024), p. 108938. ISSN: 0168-1699. DOI: `https://doi.org/10.1016/j.compag.2024.108938`.

[115] Alex Clark et al. "Bio-Inspired Soft Pneumatic Gripper for Agriculture Harvesting." en. In: *Towards Autonomous Robotic Systems*. Ed. by M. Nazmul Huda, Mingfeng Wang, and Tatiana Kalganova. Cham: Springer Nature Switzerland, 2025, pp. 266–277. ISBN: 978-3-031-72062-8. DOI: `10.1007/978-3-031-72062-8_24`.

[116] Zinat Tasneem and Koichi Oka. "Design and performance analysis of soft pneumatic manipulator-based linear cutter and stem holder for sweet pepper harvesting." en. In: *Journal of Field Robotics* 41.4 (2024). _eprint: https://onlinelibrary.wiley.com/doi/pdf/10.1002/rob.22323, pp. 1204–1225. ISSN: 1556-4967. DOI: `10.1002/rob.22323`.

[117] Eduardo Navas et al. "Diaphragm-Type Pneumatic-Driven Soft Grippers for Precision Harvesting." en. In: *Agronomy* 11.9 (Sept. 2021). Number: 9 Publisher: Multidisciplinary Digital Publishing Institute, p. 1727. ISSN: 2073-4395. DOI: `10.3390/agronomy11091727`.

[118] Yinan Sun et al. "Soft Mobile Robots: a Review of Soft Robotic Locomotion Modes." en. In: *Current Robotics Reports* 2.4 (Dec. 2021), pp. 371–397. ISSN: 2662-4087. DOI: `10.1007/s43154-021-00070-5`.

[119] Tao Wen et al. "Design, Performance Analysis, and Experiments of a Soft Robot for Rescue." In: *Journal of Mechanisms and Robotics* 16.071011 (Oct. 2023). ISSN: 1942-4302. DOI: `10.1115/1.4063669`.

[120] W. McMahan et al. "Field trials and testing of the OctArm continuum manipulator." In: *Proceedings 2006 IEEE International Conference on Robotics and Automation, 2006. ICRA 2006.* ISSN: 1050-4729. May 2006, pp. 2336–2341. DOI: `10.1109/ROBOT.2006.1642051`.

[121] Emmanouil Papadakis, Dimitris P. Tsakiris, and Michael Sfakiotakis. "An Octopus-Inspired Soft Pneumatic Robotic Arm." en. In: *Biomimetics* 9.12 (Dec. 2024). Number: 12 Publisher: Multidisciplinary Digital Publishing Institute, p. 773. ISSN: 2313-7673. DOI: `10.3390/biomimetics9120773`.

[122] Xiaomin Liu et al. "Worm-Inspired Soft Robots Enable Adaptable Pipeline and Tunnel Inspection." en. In: *Advanced Intelligent Systems* 4.1 (2022). _eprint: https://onlinelibrary.wiley.com/doi/pdf/10.1002/aisy.202100128, p. 2100128. ISSN: 2640-4567. DOI: `10.1002/aisy.202100128`.

[123] Xue Zhang et al. "A Biomimetic Soft Robot for Inspecting Pipeline with Significant Diameter Variation." In: *2018 IEEE/RSJ International Conference on Intelligent Robots and Systems (IROS).* ISSN: 2153-0866. Oct. 2018, pp. 7486–7491. DOI: `10.1109/IROS.2018.8594390`.

[124] Robert F. Shepherd et al. "Multigait soft robot." In: *Proceedings of the National Academy of Sciences* 108.51 (Dec. 2011). Publisher: Proceedings of the National Academy of Sciences, pp. 20400–20403. DOI: `10.1073/pnas.1116564108`.

[125] Yuxuan Wang et al. "A Novel High-Torque Bidirectional Curl Pneumatic Muscle With Stretchable Sheath: Design and Finite Element Method Analysis." In: *IEEE Robotics & Automation Magazine* 31.3 (Sept. 2024). Conference Name: IEEE Robotics & Automation Magazine, pp. 83–96. ISSN: 1558-223X. DOI: `10.1109/MRA.2023.3283332`.

[126] Morin Alexandre Henri. "Elastic diaphragm." en. US2642091A. June 1953.

[127] Frank Daerden. "Conception and realization of pleated pneumatic artificial muscles and their use as compliant actuation elements." PhD Thesis. Brussels, 1999.

[128] Carlo Ferraresi, Walter Franco, and Giuseppe Quaglia. "A novel bi-directional deformable fluid actuator." en. In: *Proceedings of the Institution of Mechanical Engineers, Part C: Journal of Mechanical Engineering Science* 228.15 (Oct. 2014). Publisher: IMECHE, pp. 2799–2809. ISSN: 0954-4062. DOI: 10.1177/0954406214522022.

[129] Seyed M. Mirvakili and Ian W. Hunter. "Artificial Muscles: Mechanisms, Applications, and Challenges." en. In: *Advanced Materials* 30.6 (2018), p. 1704407. ISSN: 1521-4095. DOI: 10.1002/adma.201704407.

[130] Hassanin Al-Fahaam et al. "The Design and Mathematical Model of a Novel Variable Stiffness Extensor-Contractor Pneumatic Artificial Muscle." In: *Soft Robotics* 5.5 (Oct. 2018). Publisher: Mary Ann Liebert, Inc., publishers, pp. 576–591. ISSN: 2169-5172. DOI: 10.1089/soro.2018.0010.

[131] M. Van Damme et al. "Modeling Hysteresis in Pleated Pneumatic Artificial Muscles." In: *2008 IEEE Conference on Robotics, Automation and Mechatronics*. ISSN: 2158-219X. Sept. 2008, pp. 471–476. DOI: 10.1109/RAMECH.2008.4681431.

[132] Simone Duretto. "Prototipazione di BiSoft.Q: un attuatore pneumatico, deformabile e bidirezionale realizzato tramite Fabbricazione Additiva = Prototyping of BiSoft.Q: a pneumatic, deformable and bidirectional actuator fabricated through Additive Manufacturing." laurea. Politecnico di Torino, Oct. 19, 2023. 122 pp. (Visited on 03/31/2025).

[133] Giovanni Colucci, Simone Duretto, and Giuseppe Quaglia. "Design and Prototyping of BiSoft.Q, A 3-D Printed Bi-directional Deformable Actuator." en. In: *Advances in Mechanism and Machine Science*. Ed. by Masafumi Okada. Cham: Springer Nature Switzerland, 2024, pp. 710–720. ISBN: 978-3-031-45709-8. DOI: 10.1007/978-3-031-45709-8_69.

[134] Muhammad Rusydi Muhammad Razif et al. "Two chambers soft actuator realizing robotic gymnotiform swimmers fin." In: *2014 IEEE International Conference on Robotics and Biomimetics (ROBIO 2014)*. Dec. 2014, pp. 15–20. DOI: 10.1109/ROBIO.2014.7090300.

[135] David Rostin Ellis, Martin Philip Venter, and Gerhard Venter. "Soft Pneumatic Actuator with Bimodal Bending Response Using a Single Pressure Source." In: *Soft Robotics* 8.4 (Aug. 2021). Publisher: Mary Ann Liebert, Inc., publishers, pp. 478–484. ISSN: 2169-5172. DOI: 10.1089/soro.2020.0017.

[136] J. H. Low et al. "A bidirectional soft pneumatic fabric-based actuator for grasping applications." In: *2017 IEEE/RSJ International Conference on Intelligent Robots and Systems (IROS)*. ISSN: 2153-0866. Sept. 2017, pp. 1180–1186. DOI: 10.1109/IROS.2017.8202290.

[137] Frank Daerden and Dirk Lefeber. "The Concept and Design of Pleated Pneumatic Artificial Muscles." en. In: *International Journal of Fluid Power* (Jan. 2014). Publisher: Taylor & Francis. ISSN: 1439-9776.

[138] Daniel Villegas et al. "Third–Generation Pleated Pneumatic Artificial Muscles for Robotic Applications: Development and Comparison with McKibben Muscle." EN. In: *Advanced Robotics* (July 2012). Publisher: Routledge. ISSN: 0169-1864.

[139] Corrado De Pascali et al. "3D-printed biomimetic artificial muscles using soft actuators that contract and elongate." In: *Science Robotics* 7.68 (2022), eabn4155. DOI: 10.1126/scirobotics.abn4155.

[140] Zhongkui Wang et al. "A Soft Robotic Hand Based on Bellows Actuators for Dishwashing Automation." In: *IEEE Robotics and Automation Letters* 6.2 (Apr. 2021). Conference Name: IEEE Robotics and Automation Letters, pp. 2139–2146. ISSN: 2377-3766. DOI: 10.1109/LRA.2021.3061063.

[141] Tao Wang, Wei Song, and Shiqiang Zhu. "Analytical research on energy harvesting systems for fluidic soft actuators." en. In: *International Journal of Advanced Robotic Systems* 15.1 (Jan. 2018). Publisher: SAGE Publications, p. 1729881418755876. ISSN: 1729-8806. DOI: 10.1177/1729881418755876.

[142] Sinyoung Lee, Dongun Lee, and Dongjun Shin. "An Air Recirculation System Based on Bioinspired Soft Re-Air Valve for Highly Efficient Pneumatic Actuation." In: *Soft Robotics* 8.5 (Oct. 2021). Publisher: Mary Ann Liebert, Inc., publishers, pp. 564–576. ISSN: 2169-5172. DOI: 10.1089/soro.2020.0007.

[143] Miao Feng et al. "High-Speed and Low-Energy Actuation for Pneumatic Soft Robots with Internal Exhaust Air Recirculation." en. In: *Advanced Intelligent Systems* 5.4 (2023), p. 2200257. ISSN: 2640-4567. DOI: 10.1002/aisy.202200257.

[144] Silvia Filogna et al. "A Bioinspired Fluid-Filled Soft Linear Actuator." In: *Soft Robotics* 10.3 (June 2023). Publisher: Mary Ann Liebert, Inc., publishers, pp. 454–466. ISSN: 2169-5172. DOI: 10.1089/soro.2021.0091.

[145] Seppe Terryn et al. "Self-healing soft pneumatic robots." In: *Science Robotics* 2.9 (Aug. 2017). Publisher: American Association for the Advancement of Science. DOI: 10.1126/scirobotics.aan4268.

[146] Krishna S, Nagarajan T, and Rani A. M.A. "Review of Current Development of Pneumatic Artificial Muscle." en. In: *Journal of Applied Sciences* (2011). ISSN: 18125654. DOI: 10.3923/jas.2011.

[147] Dylan Drotman et al. "Application-Driven Design of Soft, 3-D Printed, Pneumatic Actuators With Bellows." In: *IEEE/ASME Transactions on Mechatronics* 24.1 (Feb. 2019), pp. 78–87. ISSN: 1083-4435, 1941-014X. DOI: 10.1109/TMECH.2018.2879299.

[148] Tariq Rehman et al. “Design, characterization, and manufacturing of circular bellows pneumatic soft actuator.” en. In: *The International Journal of Advanced Manufacturing Technology* 93.9 (Dec. 2017), pp. 4295–4304. ISSN: 1433-3015. DOI: `10.1007/s00170-017-0891-z`.

[149] David Gonzalez et al. “Characterization of 3D printed pneumatic soft actuator.” In: *Sensors and Actuators A: Physical* 334 (Feb. 2022), p. 113337. ISSN: 0924-4247. DOI: `10.1016/j.sna.2021.113337`.

[150] Alix Lopez, Christophe A. Marquette, and Edwin-Joffrey Courtial. “FingerMap: a new approach to predict soft material 3D objects printability.” en. In: *Progress in Additive Manufacturing* 6.1 (Feb. 2021), pp. 53–62. ISSN: 2363-9520. DOI: `10.1007/s40964-020-00143-5`.

[151] Ji Hyeon Shin et al. “A Universal Soft Gripper with the Optimized Fin Ray Finger.” en. In: *International Journal of Precision Engineering and Manufacturing-Green Technology* 8.3 (May 2021), pp. 889–899. ISSN: 2198-0810. DOI: `10.1007/s40684-021-00348-1`.

[152] Xiaowei Shan and Lionel Birglen. “Modeling and analysis of soft robotic fingers using the fin ray effect.” en. In: *The International Journal of Robotics Research* 39.14 (Dec. 2020). Publisher: SAGE Publications Ltd STM, pp. 1686–1705. ISSN: 0278-3649. DOI: `10.1177/0278364920913926`.

[153] Chih-Hsing Liu et al. “Optimal Design of a Motor-Driven Three-Finger Soft Robotic Gripper.” In: *IEEE/ASME Transactions on Mechatronics* 25.4 (Aug. 2020). Conference Name: IEEE/ASME Transactions on Mechatronics, pp. 1830–1840. ISSN: 1941-014X. DOI: `10.1109/TMECH.2020.2997743`.

[154] Atsushi Kakogawa, Hiroyuki Nishimura, and Shugen Ma. “Underactuated modular finger with pull-in mechanism for a robotic gripper.” In: *2016 IEEE International Conference on Robotics and Biomimetics (ROBIO)*. Dec. 2016, pp. 556–561. DOI: `10.1109/ROBIO.2016.7866381`.

[155] Huan Liu et al. “A Single-Actuator Gripper with a Working Mode Switching Mechanism for Grasping and Rolling Manipulation.” In: *2018 IEEE/ASME International Conference on Advanced Intelligent Mechatronics (AIM)*. ISSN: 2159-6255. July 2018, pp. 359–364. DOI: `10.1109/AIM.2018.8452711`.

[156] Giuseppe Quaglia et al. “Design of an Under-Actuated Mechanism for Collecting and Cutting Crop Samples in Precision Agriculture.” en. In: *Advances in Service and Industrial Robotics*. Ed. by Doina Pisla et al. Cham: Springer Nature Switzerland, 2024, pp. 533–541. ISBN: 978-3-031-59257-7. DOI: `10.1007/978-3-031-59257-7_53`.

[157] Charbel Tawk et al. "Soft Pneumatic Sensing Chambers for Generic and Interactive Human–Machine Interfaces." en. In: *Advanced Intelligent Systems* 1.1 (May 2019). Publisher: John Wiley & Sons, Ltd, p. 1900002. ISSN: 2640-4567. DOI: 10.1002/aisy.201900002.

[158] Tsuneo Yoshikawa. "Multifingered robot hands: Control for grasping and manipulation." In: *Annual Reviews in Control* 34.2 (Dec. 2010), pp. 199–208. ISSN: 1367-5788. DOI: 10.1016/j.arcontrol.2010.09.001.

[159] N. Hogan. "Stable execution of contact tasks using impedance control." In: *1987 IEEE International Conference on Robotics and Automation Proceedings*. Vol. 4. Mar. 1987, pp. 1047–1054. DOI: 10.1109/ROBOT.1987.1087854.

[160] P.N. Akella and M.R. Cutkosky. "Contact transition control with semiactive soft fingertips." In: *IEEE Transactions on Robotics and Automation* 11.6 (Dec. 1995). Conference Name: IEEE Transactions on Robotics and Automation, pp. 859–867. ISSN: 2374-958X. DOI: 10.1109/70.478432.

[161] L. Biagiotti et al. "Modelling and Controlling the Compliance of a Robotic Hand with Soft Finger-pads." en. In: *Multi-point Interaction with Real and Virtual Objects* (2005). Publisher: Springer, Berlin, Heidelberg, pp. 55–73. DOI: 10.1007/11429555_4.

[162] Josie Hughes, Shuguang Li, and Daniela Rus. "Sensorization of a Continuum Body Gripper for High Force and Delicate Object Grasping." In: *2020 IEEE International Conference on Robotics and Automation (ICRA)*. ISSN: 2577-087X. May 2020, pp. 6913–6919. DOI: 10.1109/ICRA40945.2020.9196603.

[163] Naveen Kuppuswamy et al. "Soft-bubble grippers for robust and perceptive manipulation." In: *2020 IEEE/RSJ International Conference on Intelligent Robots and Systems (IROS)*. ISSN: 2153-0866. Oct. 2020, pp. 9917–9924. DOI: 10.1109/IROS45743.2020.9341534.

[164] Manjia Su et al. "Soft Tactile Sensing for Object Classification and Fine Grasping Adjustment Using a Pneumatic Hand With an Inflatable Palm." In: *IEEE Transactions on Industrial Electronics* 71.4 (Apr. 2024). Conference Name: IEEE Transactions on Industrial Electronics, pp. 3873–3883. ISSN: 1557-9948. DOI: 10.1109/TIE.2023.3279554.

[165] Zhongkui Wang, Ryo Kanegae, and Shinichi Hirai. "Circular Shell Gripper for Handling Food Products." In: *Soft Robotics* 8.5 (Oct. 2021). Publisher: Mary Ann Liebert, Inc., publishers, pp. 542–554. ISSN: 2169-5172. DOI: 10.1089/soro.2019.0140.

[166] G. Colucci, C. Visconte, and G. Quaglia. “Functional Design and Prototyping of a Novel Soft Fingertip with Variable Stiffness.” In: *Proceedings of I4SDG Workshop 2023*. Ed. by V. Petuya et al. Vol. 134. Mechanisms and Machine Science. Springer, Cham, 2023, pp. 375–387. ISBN: 978-3-031-32439-0. DOI: 10.1007/978-3-031-32439-0_32.

[167] S. Duretto et al. “PAL-HAND.Q: A Handheld Device for Bidirectional and Multimodal Haptic Interaction.” In: *Advances in Italian Mechanism Science*. Ed. by G. Rizzi and A. Siciliano. Vol. 164. Mechanisms and Machine Science. Springer, Cham, 2024, pp. 483–491. ISBN: 978-3-031-64569-3. DOI: 10.1007/978-3-031-64569-3_55.

[168] Hiep Xuan Trinh et al. “A novel rigid-soft gripper for safe and reliable object handling.” en. In: *Journal of the Brazilian Society of Mechanical Sciences and Engineering* 46.4 (Mar. 2024), p. 176. ISSN: 1806-3691. DOI: 10.1007/s40430-024-04757-6.

[169] *Shell-Reinforced SPA Fabrication*. en. URL: https://softroboticstoolkit.com/book/modeling-soft-pneumatic-actuators/fabrication/shell (visited on 01/28/2025).

[170] Michael Bell. *Soft Robotic Manufacturing: Bi-directional Bellow with Integrated Magnetic Dome Actuators*. Mar. 2021. URL: https://www.youtube.com/watch?v=2iv4f6lFdvs (visited on 01/28/2025).

[171] Adriana Cabrera. *Soft Robotics tutorial*. Dec. 2018. URL: https://www.youtube.com/watch?v=TyYW9BmMeSs (visited on 01/28/2025).

[172] International Organization for Standardization. *Protective clothing - Protection against cuts - Test method using a moving blade*. UNI EN ISO 13997:1999. ISO, 1999. URL: https://www.iso.org/standard/23232.html.

[173] ASTM International. *Standard Test Method for Protective Clothing Material Resistance to Puncture*. ASTM F1342-13. ASTM International, 2013. URL: https://www.astm.org/Standards/F1342.htm.

[174] C. T. Nguyen, T. Vu-Khanh, and J. Lara. “Puncture characterization of rubber membranes.” In: *Theoretical and Applied Fracture Mechanics* 42.1 (Sept. 2004), pp. 25–33. ISSN: 0167-8442. DOI: 10.1016/j.tafmec.2004.06.002.

[175] Liangliang Wang and Zheng Wang. “Mechanoreception for Soft Robots via Intuitive Body Cues.” In: *Soft Robotics* 7.2 (Apr. 2020). Publisher: Mary Ann Liebert, Inc., publishers, pp. 198–217. ISSN: 2169-5172. DOI: 10.1089/soro.2018.0135.

[176] Jeremy A. Fishel, Veronica J. Santos, and Gerald E. Loeb. “A robust micro-vibration sensor for biomimetic fingertips.” In: *2008 2nd IEEE RAS & EMBS International Conference on Biomedical Robotics and Biomechatronics*. ISSN: 2155-1782. Oct. 2008, pp. 659–663. DOI: 10.1109/BIOROB.2008.4762917.

[177] Zhen Chen et al. "A Wireless Haptic Device for Virtual Reality Based on SPSC." In: *ACM Trans. Graph.* 39.4 (2020), 88:1–88:12. DOI: 10.1145/3290605.3300401.

[178] Evan Strasnick et al. "Haptic Links: Bimanual Haptics for Virtual Reality Using Variable Stiffness Actuation." In: *Proceedings of the 2018 CHI Conference on Human Factors in Computing Systems.* ACM, 2018, pp. 1–12. DOI: 10.1145/3173577.3174173.

[179] Eric Whitmire et al. "Haptic Revolver: Touch, Shear, Texture, and Shape Rendering on a Reconfigurable Virtual Reality Controller." In: *Proceedings of the 2018 CHI Conference on Human Factors in Computing Systems.* ACM, 2018, pp. 1–12. DOI: 10.1145/3173574.3173660.

[180] Harshal Arun Sonar, Jian-Lin Huang, and Jamie Paik. "Soft Touch using Soft Pneumatic Actuator–Skin as a Wearable Haptic Feedback Device." In: *Advanced Intelligent Systems* 3.3 (2021), p. 2000168. DOI: 10.1002/aisy.202000168.

[181] Hrvoje Benko et al. "NormalTouch and TextureTouch: High-fidelity 3D Haptic Shape Rendering on Handheld Virtual Reality Controllers." In: *Proceedings of the 2016 ACM Symposium on User Interface Software and Technology (UIST).* ACM, 2016, pp. 1–12. DOI: 10.1145/2984511.2984526.

[182] Inrak Choi et al. "CLAW: A Multifunctional Handheld Haptic Controller for Grasping, Touching, and Triggering in Virtual Reality." In: *Proceedings of the 2018 CHI Conference on Human Factors in Computing Systems.* ACM, 2018, pp. 1–12. DOI: 10.1145/3173574.3173661.

[183] Jaeyeon Lee et al. "TORC: A Virtual Reality Controller for In-Hand High-Dexterity Finger Interaction." In: *Proceedings of the 2019 CHI Conference on Human Factors in Computing Systems.* ACM, 2019, pp. 1–13. DOI: 10.1145/3290605.3300301.

[184] Robert Kovacs et al. "Haptic PIVOT: On-Demand Handhelds in VR." In: *Proceedings of the 33rd Annual ACM Symposium on User Interface Software and Technology (UIST 2020).* ACM, 2020, pp. 1–12. DOI: 10.1145/3313831.3376476.

[185] HaptX. *Use Cases - Robotics.* HaptX Website. Accessed: 2024-01-02. 2023. URL: https://haptx.com/use-cases-robotics/.

[186] Sung-Sik Yun, Brian Byunghyun Kang, and Kyu-Jin Cho. "Exo-Glove PM: An Easily Customizable Modularized Pneumatic Assistive Glove." In: *IEEE Robotics and Automation Letters* 2.3 (2017), pp. 1773–1778. DOI: 10.1109/lra.2017.2678545.

[187] SIYI INTELLIGENCE. *New-Gen Soft Robotic Rehabilitation Gloves.* Syrebo Website. Accessed: 2024-01-02. 2023. URL: https://www.syrebo.com/rehabilitation-equipment-for-home/new-gen-soft-robotic-rehabilitation-gloves-sy.html.

[188] Wyss Institute at Harvard University. *Soft Robotic Glove for Neuromuscular Rehabilitation*. Wyss Institute Website. Accessed: 2024-01-02. 2023. URL: https://wyss.harvard.edu/technology/soft-robotic-glove/.

[189] CyberGlove Systems LLC. *CyberGrasp*. CyberGlove Systems Website. Accessed: 2024-01-02. 2023. URL: http://www.cyberglovesystems.com/cybergrasp.

[190] Humanware. *HumanGlove - Hand Robotic Rehabilitation Device*. Humanware Website. Accessed: 2024-01-02. 2023. URL: https://www.hmw.it/en/research-and-development/humanglove/.

[191] Cathrin Bütefisch et al. "Repetitive training of isolated movements improves the outcome of motor rehabilitation of the centrally paretic hand." In: *Journal of the Neurological Sciences* 130.1 (May 1995), pp. 59–68. ISSN: 0022-510X. DOI: 10.1016/0022-510X(95)00003-K.

[192] Chyanna Wee, Kian Meng Yap, and Woan Ning Lim. "Haptic Interfaces for Virtual Reality: Challenges and Research Directions." In: *IEEE Access* 9 (2021), pp. 112145–112162. DOI: 10.1109/ACCESS.2021.3103598.

[193] Oliver Ozioko and Ravinder Dahiya. "Smart Tactile Gloves for Haptic Interaction, Communication, and Rehabilitation." In: *Advanced Intelligent Systems* 4.2 (2022), p. 2100091. DOI: 10.1002/aisy.202100091.

[194] WEART. *TouchDIVER Pro Haptic Gloves*. Weart Website. Accessed: 2024-01-02. 2024. URL: https://weart.it/touchdiver-pro-haptic-gloves/.

This Ph.D. thesis has been typeset by means of the TeX-system facilities. The typesetting engine was LuaLaTeX. The document class was `toptesi`, by Claudio Beccari, with option `tipotesi=scudo`. This class is available in every up-to-date and complete TeX-system installation.